The Hall effect in Nonmagnetic, Ferromagnetic, and Antiferromagnetic Thin films

By

Neil Gribben Campbell

A dissertation submitted in partial fulfillment of

the requirements for the degree of

Doctor of Philosophy

(Physics)

at the

UNIVERSITY OF WISCONSIN-MADISON

2023

Date of final oral examination: December 20th, 2023

The dissertation is approved by the following members of the Final Oral Committee:

Mark Rzchowski, Professor, Physics

Chang-Beom Eom, Professor, Materials Science and Engineering

Robert Joynt, Professor, Physics

Maxim Vavilov, Professor, Physics

Abstract

The Hall effect was discovered by Edwin Hall over a century ago, and remains an important probe of conducting, and particularly, magnetic materials. Expanded epitaxial thin-film synthesis developing new complex oxide thin-film materials has instigated new interpretations of the Hall effect, with promising applications for antiferromagnetic spintronics. Hall effects resulting from topological properties of materials are of high interest, be they from a topologically-protected band structure or a Berry phase arising from antiferromagnetic spin arrangements. The materials systems investigations in this thesis resulted in better understanding of conditions for these effects, and in some systems such as $Pr_2Ir_2O_7$ uncovered new interesting phenomena, where I reported a broken symmetry arising from thin-film epitaxy that results in a spin Hall effect persisting to higher temperatures than in previous reports of the material. This suggests a road map for increasing the temperatures of important phenomena previously restricted to low-temperatures. In $SrIrO_3$ after pursuing a topological band structure, I ended up showing the lack of magnetic ordering in distorted Perovskite $SrIrO_3$, which many researchers had presumed to exist. In the Mn_3GaN chapters I use other magnetic characterizations and analysis to show the impact of heterostructuring on magnetic anisotropy in a way that demonstrates a path for manipulating hard ferrimagnets to be amenable for spintronics. I used exchange bias interactions to break the degeneracy of anti-

ferromagnetic domains, addressing a problem currently plaguing promising spintronic candidate materials. While an original goal of my research was to elucidate novel Hall effects and this did not come to fruition due to subtle electronic and structural characteristics of the materials systems I studied, I did significantly improve the understanding of Hall-effect physics for these epitaxial thin-film systems.

To all my Family and Friends who have supported me

Acknowledgements

While purusing this research I had the pleasure and opportunity of working with many people of different skills, interests, backgrounds, and disciplines. I am confident that none of the work presented here could have been accomplished solely by me and so I am thankful for the many contributions of my collaborators. While the list is truly too long and wide to name in full, I will present a highlights section here.

First, I would like to acknowledge Professor Mark Rzchowski, my research advisor from my first day of grauduate school. Working with him has been a joy, and his knowledge and thought processes have been transformative for me to observe and learn from. Next, I would like to acknowlege Professor Chang-Beom Eom, a defacto advisor of mine for the vasy majority of my time here. His expertise, project management, and ability to conjure best-in-class thin films of seemingly any material have opened countless doors and opportunties for me.

Next, I would like to acknowlege all the graduate students and postdocs of both Professors Mark Rzchowski and Chang-Beom Eom. They provided me with wonderful films, company, and comraderie during the daily grind of experimental research.

Finally, I would like to acknowledge the support of friends and family for all they did to support and nurture me prior to starting my PhD and during my PhD.

Preface

In the pyrochlore $Pr_2Ir_2O_7$ chapter, I present research about the electronic properties of thin-films that differs from the same material in bulk. This is one example of a Rare-Earth pyrochlore Iridate, an exciting class of materials. Rare earth pyrochlore Iridates ($RE_2Ir_2O_7$) consist of two interpenetrating cation sublattices, the RE with highly-frustrated magnetic moments, and the Iridium with extended conduction orbitals significantly mixed by spin-orbit interactions. The coexistence and coupling of these two sublattices create a landscape for discovery and manipulation of quantum phenomena such as the topological Hall effect, massless conduction bands, and quantum criticality. Thin films allow extended control of the material system via symmetry-lowering effects such as strain. While bulk $Pr_2Ir_2O_7$ shows a spontaneous hysteretic Hall effect below 1.5 K, we observe the effect at elevated temperatures up to 15 K in epitaxial thin films on (111) YSZ substrates synthesized via solid phase epitaxy. Similar to the bulk, the lack of observable long-range magnetic order in the thin films points to a topological origin. We use synchrotron-based element-specific x-ray diffraction (XRD) and x-ray magnetic circular dichroism (XMCD) to compare powders and thin films to attribute the spontaneous Hall effect in the films to localization of the Ir moments. We link the thin film Ir local moments to lattice distortions absent in the bulk-like powders. We conclude that the elevated-temperature spontaneous Hall effect is caused by the topological effect

originating either from the Ir or Pr sublattice, with interaction strength enhanced by the Ir local moments. This spontaneous Hall effect with weak net moment highlights the effect of vanishingly small lattice distortions as a means to discover topological phenomena in metallic frustrated magnetic materials.

In the Perovskite $SrIrO_3$ chapter, I present research about how using the thin-film platform can allow physical changes to a material that do or do not manifest as electronic and magnetic properties. Infinite-layer perovskite $SrIrO_3$ is in close phase proximity to compounds such as Sr_2IrO_4 and $BaIrO_3$ that show magnetic ordering of Ir local moments. We investigate this with different strain states of coherent, epitaxial, perovskite $SrIrO_3$ thin films by growth on different pseudocubic substrates. The strain states include both compressive and tensile strain and are controlled by growth on different (001) pesudocubic substrates. This strain controls the lattice constant which in turn influences the magnetic behavior. Resistive transport measurements show that $SrIrO_3$ remains metallic for all investigated strain states, magnetism below 30 K emerges with tensile strain. Hall measurements at fields up to 9 T are consistent with a paramagnetic state that does not show long-range ordering. These results are contrasted with Xray magnetic circular dichroism at the Ir $L_{2,3}$ edges of two $SrIrO_3$ thin films with different strain states. The Xray dichroism results corroborate the existence of a measureable local moment on the Ir sites, but do show the strain dependence observed in the Hall data.

In the Mn_3GaN/Mn_3Ga superlattic chapter, I present research about how superlatticing two materials can change the properties of one. Artificially-layered superlattices with two distinct spin structures offer new opportunities for manipulation of magnetic properties and interfacial spin configurations. We have grown epitaxial, coherent superlattices of ferrimagnetic Mn_3Ga and non-collinear antiferromagnetic Mn_3GaN. The out-of-plane ferrimagnetism of the Mn_3Ga layer, and

the Berry-phase charge to spin current generation by the non-collinear antiferromagnetic Mn3GaN layer, provide a unique combination for spintronic applications. Reactive magnetron sputtering growth resulted in abrupt transitions between the two layers through controlling the N_2 flow. X-ray diffraction and cross-sectional STEM images demonstrate the clean layering and consistent modulation wavelengths, with interfacial roughness less than one unit cell. This allows investigation of the interfacial magnetic interactions. Through a combination of SQuID magnetometry and polarized neutron reflectometry we show that Mn_3Ga / Mn_3GaN superlattice structures have the out-of-plane magnetic anisotropy decreased compared to Mn_3Ga single-layer films. This softening is primarily a result of reduced anisotropy energy at the interface, and is linked to the Mn_3GaN layer. The superlattice structure provides a platform for devices that use out-of-plane spin torques generated from an antiferromagnetic material to switch the net magnetic moment of a ferrimagnetic material. Our results demonstrate the tunability of magnetic anisotropy to allow for optimal balancing of the switching power and thermal stability in spintronic heterostructures.

In the Mn_3GaN exchange bias chapter, I present research about exchange bias in an epitaxial system with a noncollinear antiferromagnet. Noncollinear antiferromagnets provide new opportunities for spintronics. The antiperovskite antiferromagnet Mn_3GaN shows room temperature noncollinear spin order, and provides largely unexplored symmetries and anisotropies to interfacial magnetic interactions that can provide control of Berry phase generation of spin currents. We find that the exchange bias between epitaxial thin films of the noncollinear antiferromagnet Mn_3GaN and a permalloy (Py) ferromagnetic overlayer controls the antiferromagnetic domain structure, and reflects the Γ^{5g} antiferromagnetic spin order of the Mn_3GaN. We show this with a combined approach of magnetization and field-angle-dependent magneto-transport measurements and their dependence on temperature, Mn_3GaN thickness, and magnetic field magnitude and direction This

provides a route toward control of spin current generation in noncollinear antiferromagnets.

Contents

List of Figures

Chapter 1

Introduction

1.1 Introduction

In this chapter of the thesis, I will build up the relevant theory for understanding the electronic material properties of the systems I studied. Since all materials are made up of atoms, I start with an overview of atom structure, then parlay that into a discussion of electronic structure in crystals. An understanding of electronic structure is critical for understanding how to think about the materials I studied and what roles the different constituent atoms play. The discussion revolves mostly around Perovskite oxides as they are a well-studied and clean enough system for building intuition. This evolves into a discussion about the different techniques I used to probe and study the electronic and magnetic states in these materials. Finally, I discuss individually $SrIrO_3$, $Pr_2Ir_2O_7$, Mn_3GaN, and Mn_3NiN.

1.1.1 Electronic Structure of Atoms

All atoms are comprised of a positively-charged core, the nucleus, surrounded by some number of negatively-charged electrons that seeks to balance the charge of the nucleus. For almost everthing discussed in this thesis the electron portion of the atom is what is relevant. Given the inherent symmetry of the atom, the electronic sturcture can be solved for using the Schrodinger equation, resulting in single-electron levels denoted by n, the principal quantum number; l, the orbital quantum number; m_l, the magnetic quantum number; and m_s, the spin quantum number[5]. These results describe solutions to the time-independent Schrodinger's equation given the spherical Coulombic potential that results from the positively-charged nucleus.

$$-\frac{\hbar^2}{2m_e}\left(\nabla^2 + \frac{n^2e^2}{|r|}\right)\psi = E\psi \tag{1.1}$$

While in reality the situation of one electron only holds for a few light atoms, we can extend this eletronic structure to heavier atoms and treat the relevant differences as perturbations. The most relevant atoms for this work are Nitrogen (N), Oxygen (O), Manganese (Mn), Gallium (Ga), Praseodymium (Pr), Iridium (Ir), and Lead (Pb), so I'll focus on the implications for these. As will come up in the cyrstal section, only the highest-energy electrons, or valence electrons are relevant for predicting the properties of the atoms and thus the material.

Both N and O atoms have p-shell valences ($l = 1$) and large electronegativities. This makes them heavily prone to forming chemical and ionic bonds, and particularly keen for 180° bond angles.

Mn is a $3d$ transition metal, meaning $n = 3$ and $l = 2$. Its valence shell thus consists of a half-filled $3d$ orbital, and due to Hund's rule these electrons are all expected to have the same m_s quantum number[6]. Ignoring orbital effects, this endows a neutral Mn atom with a $5\mu_B$ net magnetic moment. Such a magnetic moment is quite large, and indicates that unless there are significant changes to the electronic structure due to the surrounding atoms in a crystal, we should expect Mn atoms to have local magnetic moments.

Pr is in the Lanthanide series, meaning that its valence orbitals are $4f$, and it ionizes easily to form ionic bonds, but does not generally form covalent bonds. The valence $4f$ orbital contains 3 electrons, again with their spins aligned this yields a net magnetic moment of $3\mu_B$. Furthermore, I'll note that orbitals of Pr have smaller spatial extent compared to other elements such as Ir, and it has a small electronegativity. This combination means that in $Pr_2Ir_2O_7$, Pr atoms are ionically bonded and electronically isolated.

Ir is a $5d$ transition metal, with 7 electrons in its $5d$ orbital when the atom is neutral. A relevant point about Ir is that the nucleus has a large charge, and the orbital quantum number $l = 2$ is large enough that to accurately describe the electronic structure, we must consider the coupling between the electron spin and the orbital angluar momentum, called spin-orbit coupling.

In contrast to Ir, Pb, which is just 5 elements to the right of Ir, has a full $5d$ shell, and its valence electrons ar $6sp$ in nature. While the nuclear charge in Pb is still strong, the lower orbital angular momentum means spin-orbit coupling is absent in Pb and it is more similar to O and N than to Ir in this sense.

1.1.2 Electronic Structure of Crystals

When many atoms are combined to form a material, and the atoms are arranged in such a way that there is perfect translational symmetry, then we call the ensemble of atoms a crystal. This work focuses on the properties of crystalline thin films, which are crystals created by various deposition methods onto substrates, which are crystals themselves. To gain an intuiation for the ways in which crystals can influence electron behavior we start with some simplyfing assumptions. In the simplest case, we ignore the influence of the atoms on the potential experienced by the electrons and consider the impact from the particle and wave nature of the electrons in the crystal. This yields a simple density of states as well as a Fermi energy and also lets us discuss the classical Hall effect. Then we consider the periodic nature of the crystalline potential and discover the presence of discrete electron bands.

Electrons as Classical Particles

In a conducting material, the simplist situation one can imagine is many electrons moving in a volume that has scattering sites. At non zero temperature, these electrons have random kinetic energy that results in microscopic motion, but no net movement of charge[7]. Furthermore, due to the positive ions, impurities, and other electrons, these electrons will scatter at some rate (ν_s). Beyond these scattering interactions, we do not assume any other influence on the electron behavior from the host material.

$$\begin{aligned} E_{kin} &= \frac{1}{2} m_e v_e^2 = \frac{3}{2} k_B T \\ v_e &= \sqrt{\frac{k_B T}{m_e}} \end{aligned} \tag{1.2}$$

At 300 K and using the free-electron rest mass this gives individual electrons average speeds of $1.2 \cdot 10^5$ m/s, which is not, on its face, unreasonable. If we incorporate scattering, with an average time between scattering events, $\tau_s = 1/\nu_s$, then we can compute a mean free path for the electrons.

$$l = v_e \tau_s \tag{1.3}$$

For a 1 nm mean free math path, we find a scattering time of one event every $8.6 \cdot 10^{-15}$ s. This is reasonably close to the known value for copper of, a good conductor, of $2.4 \cdot 10^{-14}$[7].

If we now consider biasing such a situation with an electric field $\vec{E}$, then nothing written in this model so far would preclude the electrons accelerating to infinite speeds. We know this prediction is incorrect as charge in even the best conductors is known to flow at a steady rate. To resolve this, we assume an electron drag force that is proportional to the velocity, and set it equal to the force from the electric field.

$$\begin{aligned} F_{drag} &= m_e \bar{v}_e / \tau_s \\ 0 &= e\vec{E} - m_e \bar{v}_e / \tau_s \\ \bar{v}_e &= e\vec{E}\tau_s / m_e \end{aligned} \tag{1.4}$$

To determine current density, $\vec{j}$, a quantity we can measure in the lab, we sum over all the conducting electrons in the volume, which in this case have been assumed to behave the same. The number density of the electrons is represented as n_e.

$$\begin{aligned}\vec{j} &= en_e\bar{v}_e\hat{E} \\ &= \frac{e^2 n_e \tau_s}{m_e}\vec{E} \\ &= \hat{\sigma}\vec{E}\end{aligned} \tag{1.5}$$

Here we have applied Ohm's law to the situation, and given the material a conductivity tensor $\hat{\sigma}$. From this we can find the familiar on-diagonal elements of the conductivity and resistivity, ρ.

$$\begin{aligned}&= \hat{\sigma}\vec{E} \\ \hat{\sigma}\vec{E} &= \vec{j} \\ \sigma_{xx} &= \frac{1}{\rho_{xx}} = \frac{e^2 n_e \tau_s}{m_e}\end{aligned} \tag{1.6}$$

In equation 1.6 n_e is the number density of the electrons, $\bar{v}_e$ is the average net velocity of the electrons, and e is the electron charge. The steady-state nature of this solution hinges on the random scattering processes in the material that result in a drift velocity $\bar{v}_e = v_d$ for the electrons instead of an acceleration[7].

1.1.3 Electrons as Quantum Mechanical Waves

Since, in fact, electrons do not behave entirely as classical point particles, it is useful to take into consideration their wave nature when describing conduction in materials. Additionally, since the wave nature will result in various allowed states, or energy levels, we must recall that electrons are fermions, and so any two electrons cannot be in the same electronic state in the same crystal.

This leads to a Fermi energy, which describes the energy of the highest-energy electrons. These electrons are the ones relevant for predicting conduction behavior. In reciprocal, or k, space, the natural space for describing wave phenomena, this reveals a Fermi surface which tells us the wavevectors of the electrons at the Fermi energy[7].

Free Election Model

In a crystal, most electrons in the inner shells are so close to one nucleus, and far from any other nuclei that they are effectively in a Coulomb potential and are localized around said nucleus. Due to the shell theorem, since the net charge within the radius of the outermost non-valence electrons is close to zero, the nuclear charges are close to entirely shielded. Furthermore, when adding together so many Coulomb potentials, the spatial variation of the energy for the valence electrons is close to uniform. This is motivation for the free electron model, where we consider the limit in which the only relevant energy change is the close-to-infinte potential at the edges of the crystal[7]. This then maps our problem onto the well-known particle in a box problem.

$$\begin{aligned} -\frac{\hbar^2}{2m_e}\nabla^2\psi_K &= E_K\psi_K \\ \psi_K &= A\mathrm{e}^{ik_x x}\mathrm{e}^{ik_y y}\mathrm{e}^{ik_z z} \\ E_K = \frac{|\vec{K}|^2\hbar^2}{2m_e} &= (k_x^2+k_y^2+k_z^2)\frac{\hbar^2}{2m_e} \end{aligned} \tag{1.7}$$

Enforcing the finite cyrstal constraint requires periodic boundary conditions be applied to the wave function. For a crystal with atomic periodicity a in every direction and finite lengths L_x, L_y, and L_z in the x, y, and z directions we say there are N_x, N_y, and N_z repeating units in each direction. This constrains the K_i values to discrete quantities based on the crystal size.

$$
\begin{aligned}
K_i &= \pm n\frac{2\pi}{N_i a} \text{ for } i = x, y, z \text{ and } n \in \mathbb{N} \\
\lambda_F &= \frac{2\pi}{K_i(n = mN_i)} = \frac{a}{m}
\end{aligned}
\tag{1.8}
$$

In 1.8 the periodic boundary conditions have constrained the K_i to take discrete values in accordance with the crystal size and periodicity. If we consider the case of m electrons contributing to the free electron model from each a^3 volume, then we can find K_i at the Fermi surface. It is more intuitive to calculate the wavelength of such a wave. Doing so reveals that the electron waves at the Fermi surface have a peroidicity that is the crystalline periodicity divided by an integer. Thus, the waves situate such that there is a node at the most energetically unfavorable position in each periodic cell in each direction[7].

From this model we can find the Fermi energy of the electronic system. To do so, we first need the density of states, or number of allowed electron states in a unit of volume in reciprocal space.

$$
\begin{aligned}
g(K)dK &= \frac{N_x N_y N_z}{(2\pi/a)^3} 4\pi K^2 \mathrm{d}K \\
&= \frac{(N_x a)(N_y a)(N_z a)}{2\pi^2} K^2 \mathrm{d}K \\
&= \frac{V}{2\pi^2} K^2 \mathrm{d}K
\end{aligned}
\tag{1.9}
$$

We then fix the number of free electrons in the system to the integral of $g(K)\mathrm{d}K$ from $K = 0$ to $K = K_F$, the Fermi wavevector, allowing for two electrons per wavevector state.

$$
\begin{aligned}
N_e &= 2\int_0^{K_F} \frac{V}{2\pi^2} K^2 \mathrm{d}K \\
&= \frac{V K_F^3}{3\pi^2} \\
K_F &= \left(\frac{3N_e\pi^2}{V}\right)^{1/3} \\
E_F &= \frac{\hbar^2}{2m_e}\left(\frac{3N_e\pi^2}{V}\right)^{2/3} \\
&= \frac{\hbar^2 K_F^2}{2m_e}
\end{aligned}
\tag{1.10}
$$

In equations 1.9 and 1.10 V is the volume of the conducting material, K_F and E_F are the Fermi wavevector and energy, N_e is the total number of electrons, and n_e is the number density of the electrons. We now have an expression for the energy of the highest-energy electron in the conducting system.

Conduction in K-Space

Now that we have a description of the electronic structure, we can describe conduction, or transport of electric charge, via the electron mass and the group velocity ($\frac{\mathrm{d}\omega}{\mathrm{d}K}$) of the wave. To produce a net flow of charge, we assume an electric field $\vec{E}$ is applied to the crystal. Since our model of conductivity will involve electrons moving to unoccupied energy levels, only the electrons close to the Fermi surface will be involved, and so we take the above description from 1.10[7]. And recall that in quantized systems $E = \hbar\omega$.

$$
\vec{p} = m_e\vec{v}_g = m_e\vec{\nabla}_K\omega = \frac{m_e}{\hbar}\vec{\nabla}_K E = \hbar\vec{K} \tag{1.11}
$$

$$\begin{aligned} \vec{F} &= -e\vec{E} \\ &= \frac{\mathrm{d}\vec{p}}{\mathrm{d}t} \\ &= \hbar\frac{\mathrm{d}\vec{K}}{\mathrm{d}t} \\ \frac{\mathrm{d}\vec{K}}{\mathrm{d}t} &= -\frac{e}{\hbar}\vec{E} \end{aligned} \tag{1.12}$$

From 1.12 it is clear that the electron motion in the crystal comes from a shift in the momentum states of electrons at the Fermi surface. When there is no electric field in this case the Fermi surface will be the locus of points equidistant from $\vec{K} = 0$, which averages out to no net momentum; and when $\vec{E}$ turns on it shifts the Fermi surface to momenta with the opposite polarity of the field, creating a net charge flow. As in 1.3 we need to add in a term to cap the electron momentum at finite values to match emperical observations of constant-rate charge currents. In this case, we modify 1.6 with the Fermi velocity to calculate σ_{xx} values[7].

$$\begin{aligned} \sigma_{xx} &= \frac{1}{\rho_{xx}} = \frac{e^2 n_e l_{mfp}}{m_e v_F} \\ &= \frac{1}{\rho_{xx}} = \frac{e^2 n_e l_{mfp}}{\sqrt{2 m_e E_F}} \end{aligned} \tag{1.13}$$

1.1.4 Tight Binding Model

The relevant theory to discuss next is the tight-binding model of electrons in a solid. This describes more localized electrons than the free-electron model as a result of the strong influence of the crystal lattice. Put another way, this provides description for conducting materials on the

covalent-ionic bonding spectrum. To describe the electrons, instead of starting with planar waves as we did for the free-electron model for metallic-bonded materials, here we start with the atomic wavefunctions and build a compound based on combining them.

When combining atomic orbitals, we expect that the electronic charge density should have the same periodicity as the crystal lattice, a condition known as the Bloch condition.

$$\psi_{\vec{k}}(\vec{R}+\vec{r}) = e^{i\vec{k}\cdot\vec{R}}\psi_{\vec{k}}(\vec{r}) \tag{1.14}$$

As in equation 1.14 the electronic wave function is constrained to differ by no more than a phase when translated by $\vec{R}$, the vector of lattice translational symmetry, and ψ is the total electronic wave function. When starting from individual atomic wavefunctions $\phi_n(\vec{r})$, we want a sum of these to represent ψ.

$$\psi_k = \frac{1}{\sqrt{N}}\sum_{\vec{R},n} e^{i\vec{k}\cdot\vec{R}}\phi_n(\vec{r}+\vec{R}) \tag{1.15}$$

In equation 1.15 we have a linear combination of atomic orbitals, another name tight binding. For intuition, we can check two values of $\vec{k}$, $\vec{k}=\vec{0}$ and $\hat{i}\frac{\pi}{a}$ where a is the periodicity of the lattice in the $\hat{i}$ direction. In the first case, the phase is always one, and as a result there is significant electron density between the two lattice site creating what is called a 'bonding' configuration. In contrast, the second value of $\vec{k}$ results in a phase difference of -1 between adjacent lattice sites. As a result, the phase must cross from positive to negative and go through zero, resulting with significantly less electron density between the lattice sites, producing an 'anti-bonding' configuration.

Tight Binding in a Cubic Perovskite

For intuition it is a useful exercise to apply tightbinding to a simple cubic perovskite system. Perovskites discussed in this thesis are predominantly thought of a ionic materials for which we can write down a formal charge on each atom. However, as many of the materials considered here are conducting, a framework for understanding the band structure is useful. Furtheremore, since the BO_3 system what drives the electronic properties many concepts translate well to other oxide systems, and even to some antiperovskites.

Here I follow the derivation of Thomas Wolfram and Sinasi Ellialtioglu in their excellent introduction to Perovskite oxides, *Electronic and Optical Properties of d-band Perovskites*[8]. To orient ourselves, we focus on the BO_3 system, and locate B at the origin, and the three Oxygen atoms each a distance a from B along the three principal directions $\hat{e}_x$, $\hat{e}_y$, and $\hat{e}_z$. The lattice vector for the Perovskite system is then that of the B atom.

$$\vec{R}_B = 2a(n_x\hat{e}_x + n_y\hat{e}_y + n_z\hat{e}_z) \tag{1.16}$$

In this system there are 14 relevant atomic orbitals, $5d$-band orbitals from the B ion and $3p$-band orbitals from each of the 3 Oxygen atoms. In a system of N atoms, this means we have $14N$ oribtals. To help with the complexity, we can rewrite the Bloch condition and total wavefuction ψ with sufficient subscripts.

$$\begin{aligned}\phi^{\vec{k},\nu}_{mj\alpha} &= \frac{1}{\sqrt{N}} e^{i\vec{k}\cdot R_{mj}} \phi_{j\alpha}(\vec{k},\nu) \\ \psi_{\vec{k}\nu}(\vec{r}) &= \frac{1}{\sqrt{N}} \sum_m \sum_{j\alpha} e^{i\vec{k}\cdot\vec{R}_{mj}} \phi_{mj\alpha}(\vec{k},\nu)\end{aligned} \tag{1.17}$$

In equation 1.17 we have switched to now represent the j-th atom in the m-th unit cell with subscripts, while α indexes the symmetry of the orbital, the options for which differ between B and O atoms. Solving for the energy levels then becomes an eigenvalue equation in which the Hamiltonian represents the kinetic energy of the electrons and the crystal energy of Perovskite lattice.

$$\frac{1}{\sqrt{N}} \sum_n \sum_{i\alpha} \left(H_{j\beta,i\alpha}(\vec{R}_n - \vec{R}_m) - E_{\vec{k}\nu}\delta_{\alpha\beta}\delta_{nm}\delta_{ij} \right) e^{i\vec{k}\cdot\vec{R}_{in}} \phi_{i\alpha}(\vec{k},\nu) = 0 \tag{1.18}$$

In equation 1.18 the contributions from lattice sites, n, atoms in the unit cell and their individual oribtals $i\alpha$ are summed over. This provides an expression that links each band's energy E_ν to atomic orbitals $\phi_{i\alpha}$ and the crystal structure through the potential energy in H.

A good computational group can take equation 1.18 or a massaged form and run with it. But to build intuition for experimental endeavors, it is useful to work through the solution to the 14×14 matrix with geometry and understood facts. Since the basis elements are atomic orbitals, all p orbitals on the same oxygen site do not overlap, and neither do d orbitals between the e_g and t_{2g} manifolds.

The on-diagonal elements of the equation 1.18 matrix have form $< \phi_\alpha | H(\vec{r}) | \phi_\alpha >$ which we know has three main contributions. There are an ionization energy E_{ion}, an electrostatic, or Madelung, energy V_M, and a term from electrostatic splitting Δ. These energies can be summa-

rized into four parameters for the four natural categories of orbitals[8].

$$\begin{aligned} E_e &= E_d + V_M(B) + \frac{3}{5}\Delta(d) \\ E_t &= E_d + V_M(B) - \frac{2}{5}\Delta(d) \\ E_\perp &= E_p + V_M(O) + \frac{1}{3}\Delta(p) \\ E_\parallel &= E_p + V_M(O) - \frac{2}{3}\Delta(p) \end{aligned} \tag{1.19}$$

The off-diagonal elements rely more heavily on the geometry of the Perovskite crystal. We consider only nearest and next-nearest-neighbor interactions. These have two types. The nearest-neighbor interaction is between B-site d orbitals and Oxygen p orbitals, and the next-nearest neighbor interactions are between two oxygen atoms on adjacent faces.

$$\begin{aligned} H_{d-o}(\pm a\hat{e}_j) &=< \phi_d(\vec{r})|H|\phi_o(\vec{r} \pm a\hat{e}_j) > (j \in \{x, y, z\}) \\ H_{o-o}(\pm a\hat{e}_i \pm a\hat{e}_j) &=< \phi_o(\vec{r} \pm a\hat{e}_i)|H|\phi_o(\vec{r} \pm a\hat{e}_j) > (i \neq j; i, j \in \{x, y, z\}) \end{aligned} \tag{1.20}$$

We again rely heavily on geometry to compute these off-diagonal elements. First, when discussing Oxygen p orbitals, it is easier to define the 3 orbitals with respect to the B-site. The one p orbital that extends toward the adjacent B sites I will refer to as the $p_\parallel$ orbital and the other two that extend perpendicular to the B-O-B axis I refer to as $p_\perp$. By symmetry these will have the same matrix values. The first equation in 1.20 respresents the mixing of the B-site d obitals with the Oxygen p orbitals. As the t_{2g}-type d obitals do not have spatial extent along the B-O-B axis, these orbitals have matrix element values of zero when mixed with the $p_\parallel$ orbitals, while the t_{2g}-$p_\perp$

element has a nonzero value of $\pm(pd\pi)$[8].

The σ bonds come from the e_g manifold mixing with the $p_{\|}$ orbitals. Because of the different geometry of the d_{z^2} and $d_{x^2-y^2}$ orbitals, they mix differently with the different p orbitals.

$$\begin{aligned}
< d_{z^2}(\vec{r})|H|p_\alpha(\vec{r} \pm a\hat{e}_\alpha) > &= \pm\frac{1}{2}(pd\sigma)(\alpha \in \{x, y\}) \\
< d_{z^2}(\vec{r})|H|p_z(\vec{r} \mp a\hat{e}_z) > &= \pm(pd\sigma) \\
< d_{x^2-y^2}(\vec{r})|H|p_x(\vec{r} \mp a\hat{e}_z) > &= \pm\frac{\sqrt{3}}{2}(pd\sigma) \\
< d_{x^2-y^2}(\vec{r})|H|p_y(\vec{r} \mp a\hat{e}_y) > &= \mp\frac{\sqrt{3}}{2}(pd\sigma)
\end{aligned} \tag{1.21}$$

We not consider the Oxygen-Oxygen contributions. These interactions give rise to many non-vanishing elements, which can be partitioned into 3 catogories based on the simplified form of the integral. The categories differ with regard to which adjacent Oxygen orbitals mix with which orbital on the adjacent Oxygen atom[8].

$$\begin{aligned}
< p_\alpha(\vec{r}) \mp a\hat{e}_\alpha|H|p_\beta(\vec{r} \mp a\hat{e}_\beta) > &= -(\mp)(\mp)\frac{1}{2}[(pp\pi) - (pp\sigma)](\alpha \neq \beta; \alpha, \beta \in \{x, y, z\}) \\
< p_\alpha(\vec{r}) \mp a\hat{e}_\alpha|H|p_\alpha(\vec{r} \mp a\hat{e}_\beta) > &= \frac{1}{2}[(pp\pi) + (pp\sigma)](\alpha \neq \beta; \alpha, \beta \in \{x, y, z\}) \\
< p_\gamma(\vec{r}) \pm a\hat{e}_\alpha|H|p_\gamma(\vec{r} \pm a\hat{e}_\beta) > &= (pp\pi)(\alpha \neq \beta \neq \gamma; \alpha, \beta, \gamma \in \{x, y, z\})
\end{aligned} \tag{1.22}$$

We have now defined all the terms in the secular equation for the Perovskite unit cell with eight parameters: $(pd\sigma)$, $(pd\pi)$, $(pp\sigma)$, $(pp\pi)$, E_e, E_t, $E_{\|}$, and $E_{\perp}$. At this point we can build the matrix and perform eigenvalue and vector analysis. To compute a traditional band structure, E v $\vec{k}$, we must reinsert the phase, $\exp i\vec{k} \cdot (\vec{\tau}_i - \vec{\tau}_j)$ where $\vec{\tau}_i$ is the location in the unit cell of atom

i. I will also note that grouping the following orbitals adjacently in the 14x14 matrix achieves a block diagonal matrix in the absence of Oxygen-Oxygen interactions, the least significant of those considered here. The first group is the e_g manifold and consists of the $d_{z^2}(\vec{r})$, $dx^2 - y^2(\vec{r})$, $p_x(\vec{r} - a\hat{e}_x)$ and $p_y(\vec{r} - a\hat{e}_y)$ orbitals. The next three groups together constitute the t_{2g} manifold. They are grouped as $d_xy(\vec{r})$, $p_x(\vec{r} - a\hat{e}_y)$, and $p_y(\vec{r}a\hat{e}_x)$; $d_xz(\vec{r})$, $p_x(\vec{r} - a\hat{e}_z)$, and $p_z(\vec{r}a\hat{e}_x)$; and $d_yz(\vec{r})$, $p_y(\vec{r} - a\hat{e}_z)$, and $p_z(\vec{r}a\hat{e}_xy)$[8].

The 3x3 sub-blocks have 2 eigenenergies, one that comes from only Oxygen-Oxygen interaction and one whose weight is a mix of all three orbitals. This the Fermi energy for the system, and the analytical expression for for the energy can be used to find the theoretical effective band mass and bandwidth.

$$E_{\vec{k}}^{\alpha\beta} = c1 + \sqrt{c2 + 4(a(pd\pi))^2(\sin^2 k_\alpha + \sin^2 k_\beta)} \tag{1.23}$$

Where in equation 1.23 I have ignored all Oxygen-Oxygen interactions, and $c1$ and $c2$ are constants. In this case the bandwidth is non trivial and easier to see that it depends on $(pd\pi)$. Notably, this also results in a flat band in that $E^{\alpha,\beta}$ only depends on the α and β components of $\vec{k}$. This property makes Perovskites easy to abstract into Ruddlesden-Popper phases and thin-film heterostructures. Furthermore, the result that the main contribution to electronic properties from transition metals coordinated with Oxygen is from the metal cation's d orbitals hybridizing with the adjacent Oxygen p orbitals will prove useful more complicated materials such as $Pr_2Ir_2O_7$[8].

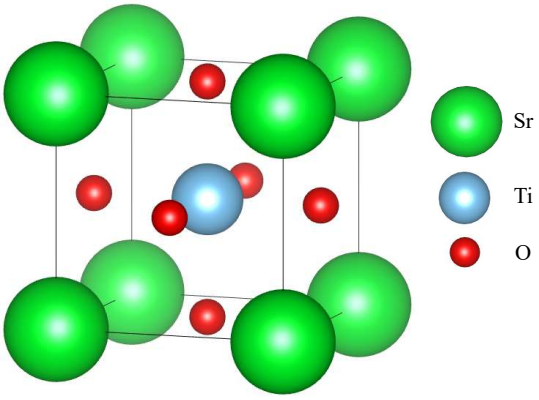

Figure 1.1: The simple cubic unit cell of Perovskite $SrTiO_3$ has the A-site cation, Sr, in the corners, B-site cation, Ti, in the body center, and anions, O,at the face centers.

1.1.5 Crystal Fields, d-orbitals, and Anions

Transition metals are mostly interesting because of their valence electrons are in d orbitals. These orbitals have $l = 2$, $m_l \in \{-2, -1, 0, 1, 2\}$, and consequently can hold up to 10 electrons. The best understood of these materials are the $3d$ monoatomic metals such as Fe and Ni, which are known for their strong ferromagnetism. This comes about as a result of the valence $3d$ orbitals being close to half full combined with Hund's rule stating that all the electron spins, m_s will have the same value before m_l orbitals are doubly occupied[6]. The sum of these m_s is the net magnetic moment, which has saturation values on the order of multiple μ_B/atom.

As shown in figure 1.2, these orbitals have directional lobes, and so in materials with anions present, such as oxides and nitrides, these anions will coordinate according to the geometry of the d orbitals. One common coordination occurs in Perovskite oxides such as $SrTiO_3$. In this case, the material has a cubic, or near-cubic, symmetry, and the anions, Oxygen, are arranged in an octahedral coordination around the B-site cation, Ti in $SrTiO_3$ as show in figure 1.1. The resultant electric field of the Oxygen atoms creates a crystal field effect on the Ti d-orbitals that breaks their

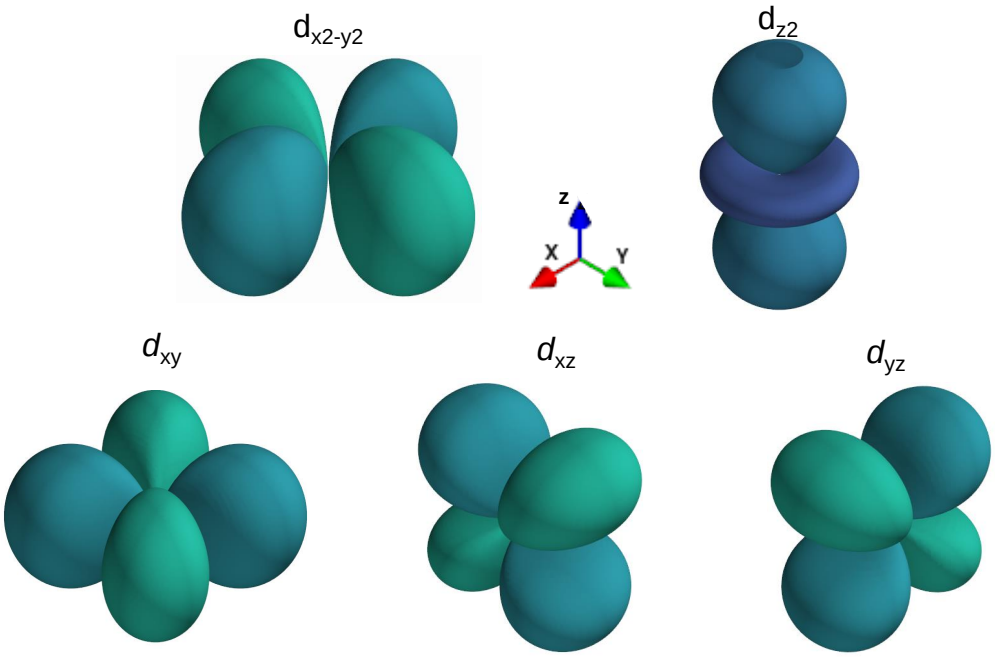

Figure 1.2: The 5 d orbitals are shown here in the basis that makes the most sense for thinking about Perovskites coordination. The $d_{x^2-y^2}$ and d_{x^2} orbitals have electron density along the $\hat{e}_x$, $\hat{e}_y$, and $\hat{e}_z$ directions which corresponds to where Oxygen sit in the Perovskite lattice. The d_{xy}, d_{xz}, and d_{yz} orbitals all have electron density that does not point toward an Oxygen atom. As a result, the $d_{x^2-y^2}$ and d_{x^2} orbitals shown in the top row constitue the e_g manifold, while the d_{xy}, d_{xz}, and d_{yz} orbitals in the bottom row constitute the t_{2g} manifold.

degeneracy creating two subbands referred to as e_g and t_{2g}. This energy shift is best motivated geometrically, by noting that the octahedral symmetry can be mimiced by the $m_l = 0$ orbital and an equal-weight linear combination of the $m_l = \pm 2$ orbitals. It is these two orbitals that have electron density in the direction of the anions and thus have a higher energy, while the remaining three orbitals have a lower energy. In Perovskite oxides, the gap between the e_g and t_{2g} orbitals is significant enough to dominate over Hund's rule, and so electrons fill the t_{2g} manifold before the ${e_g}^6$.

As examples, let's consider two $3d$ transition-metal Perovskites, $SrTiO_3$ and $La_{1-x}Sr_xMnO_3$ (LSMO). The electron configuration of Ti is [Ar]$3d^2 4s^2$, and Sr is [Kr]$5s^2$. Conveniently, if both

of these materials oxidize down to their noble shells, that creates 6 electrons to reduce the 3 oxygen per formula unit, and so that is the purely ionic picture of $SrTiO_3$. In this case the Ti atom now has the largest charge, and so if we add just one additional electron to this crystal, it was situate in the Ti t_2g manifold which is the conduction band. This is, in fact, what occurs in the well-studied LAO/STO 2DEG system[9].

Alternatively, in LSMO, the relevant B-site cation is Mn which has an electron configuration of [Ar]$3d^5 4s^2$, and so oxidizes to have only 2 or 3 electrons in the Mn t_{2g} orbital that have the same m_s quantum numbers, resulting in a strong net magnetic moment of a few μ_B/Mn. Separate from have a strong net magnetic moment is the topic of whether that moment orders. LSMO undergoes a paramagnetic to ferromagnetic Curie transition at 320K, as shown in figure [M-T of LSMO].

A final point to discuss about d-orbitals derives from the $l = 2$ quantum number. Such large angular momentum gives rise to spin-orbit coupling. Section [ref spin-orbit coupling discussion] discusses this phenomena in more detail. Because the spin-orbit coupling energy scales strongly with Z^4 (or Z^2 for large Z), it is a major differentiator between $3d$ and $5d$ ions[10]. A large amount of recent research has been focused recently on better understanding $5d$ transition metals due to their intriguing phenomena such as spin-orbit torques and and skyrmions [Moon et al (2008), Kawasaki et al (2016), Nie et al (2015), Cao and Schlottmann (2018), Nan et al (2019), Mohanta et al (2019)]. Core to understanding these observations is spin-orbit coupling, and the most straightforward and wide-spread observations have occured in $SrIrO_3$.

1.1.6 Xray Spectroscopy, $5d$ orbitals, and spin-orbit coupling

X-ray absorption spectroscopy is a powerful tool for studying the electronic structure of materials, and can be extended to quantify the spin-orbit coupling in $5d$ transition-metal systems such as

Iridates. Clancy et al noted that many Ir-containing materials are insulating, despite the $5d^5$ configuration of the Ir^{4+} state that would suggest metallic behavior[11]. This study was based off that of Laguna-Marco, who used this technique to observe a large spin-orbit interaction in $BaIrO_3$ doped with Sr[12]. The resolution of this puzzle comes from accounting for the spin-orbit coupling present in the electronic system. The theory was originally posed by Thole and van der Laan in a series of 3 articles in 1988[13–15], in which they showed that the spin-orbit coupling could be measured by the ratio of the L_2 and L_3 edge absorptions. In Xray spectroscopy, and L-edge is an electronic transition from a $2p$ orbital to an unfilled valence d orbital. The L_2 edge comes from electrons with a $J_{eff} = 1/2$ d state, while L_3 comes from those with a $J_{eff} = 3/2$[16]. The branching ratio is related to the spin-orbit coupling by

$$\begin{aligned} \frac{I_(L_3)}{I(L_2)} &= \frac{2+r}{1-r} \\ r &= \frac{<\mathbf{L}\cdot\mathbf{S}>}{<n_h>} \end{aligned} \tag{1.24}$$

where in 1.24 $< n_h >$ is the expected number of holes. It is simple then to see that branching ratios in excess of 2 indicate a significant spin-orbit coupling. The spin-angular expectation is over the ground state, and $j_{eff} = \frac{1}{2}$ electrons have $< \mathbf{L}\cdot\mathbf{s} >= \mathbf{1}$[12]. The impacts of spin-orbit coupling and crystal-field splitting are shown in figure 1.3.

1.1.7 Thin Film resistivity: van der Pauw method

When studying the electrical properties of thin films, we often are interested in the quantities of longitudinal and transverse resistivity, where the latter comes from the Hall effect. When thinking about longitudinal resistivity, we typically have a fixed current direction present and set up voltage

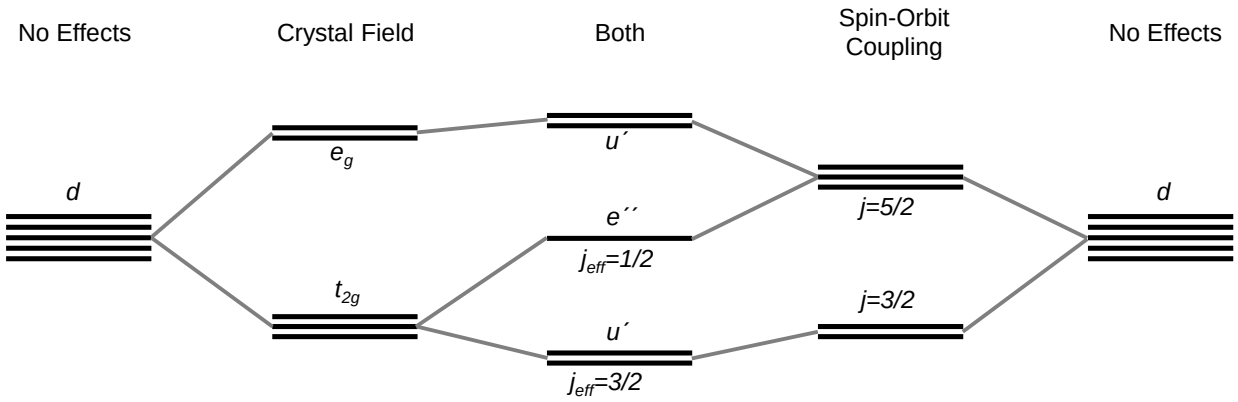

Figure 1.3: Otherwise degenerate d orbitals are commonly referenced by the subspaces that come about due to the effects of both crystal-field splitting and spin-orbit coupling. The common Ir^{4+} cation has 5 d electrons.

measurements along this defined current path. However, this is a one-dimensional view, and does not easily abstract to a two-dimensional film. One approach often taken is to what what is referred to as patterning the film. This involves somehow constraining the current so it can only flow along one well-defined direction. In this case as simple 4-point voltage measurement allows for effective measurement of the resistance.

$$\begin{aligned} R &= \frac{I}{\Delta V} \\ \rho &= R\left(\frac{\tau w}{l}\right) \end{aligned} \tag{1.25}$$

In equation 1.25 the voltage drop ΔV is between voltage leads placed l apart inside of the two current leads, and τ, w represent the thickness of the film and patterned width of the channel respectively. If two perpendicular directions are chosen, then the resistivity tensor can be created.

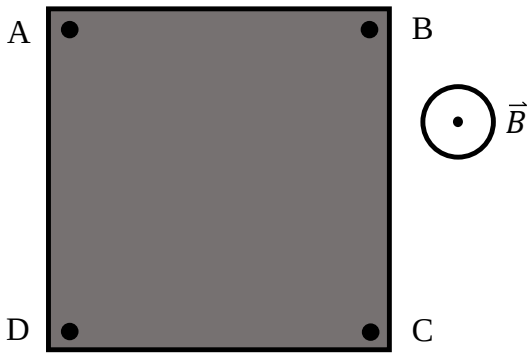

Figure 1.4: A square film sample needs four electrical contacts placed in the corners of the film. For clarity in discussions, they are labelled A, B, C, and D.

$$\hat{\rho} = \begin{pmatrix} \rho_{xx} & \rho_{xy} \\ \rho_{yx} & \rho_{yy} \end{pmatrix} \tag{1.26}$$

In equation 1.26 ρ_{xx} and ρ_{yy} are the two longitudinal resistivities measured with equation 1.25. The off diagonal measurements can be easily performed by measuring the voltage drop across the width of the channel. While in theory this method of characterizing a film's resistivity should work well, in practice in the films discussed in this thesis it does not. The hangup is in the patterning step. First, patterning can take up to a couple days to complete, slowing down the growth-properties feedback loop that allows these systems to be fine tuned. Secondly, patterning the films can cause their physical properties to change. The most common methods of patterning utilized both involve depositing a full film then removing parts of it leaving only the desired conducting channels. This process is fraught with either solvents or ionic bombardment that can impact the film and the substrate, even when the utmost care is taken to avoid such issues. As a result, the van der Pauw method is most often used to measure the film resistivity.

The van der Pauw method was developed by L.J. van der Pauw, and put forth in the report "A method of measuring specific resistivity and Hall effect of discs of arbitrary shape." The summary of this report states that it works for a "flat sample of arbitrary shape if the contact are sufficiently small and located at the circumference of the sample. Furthermore, the sample must be singly connected, ie, it should not have isolated holes[17]." The films I measured were primarily close to square, and so contacts were made by wirebonding to the sample corners as in figure 1.4.

Resistivty measurements then utilize all four corners in 4 distinct configurations, where subscript letters indicate the ordered positive and negative polarities of the measurement (ie V_{AB} is voltage at pin A minus voltage at pin B and I_{AB} is current flowing from pin A to pin B).

$$\begin{aligned} R_{vdP1} &= \frac{V_{AB}}{I_{DC}} \\ R_{vdP2} &= \frac{V_{AD}}{I_{BC}} \\ R_{Hall1} &= \frac{V_{DB}}{I_{AC}} \\ R_{Hall2} &= \frac{V_{CA}}{I_{DB}} \end{aligned} \tag{1.27}$$

The two classifications of resistance types in equation 1.27 are vdP, which capture the longitudinal resistivity, and Hall, which capture the transverse. The astute reader will notice that many more configurations are possible, and perhaps ought to be measured in order to wholly measure the film resistivity. The most obvious additional configuration is to swap the order of each subscript, which amounts to switching the current polarity. This is achieved in the measurements by using a bipolar current source. The other type of configuration is to swap the subscripts between V and I. If we extend the requirements of vdP measurement to include that the sample's conduction

must be homogeneous and isotropic, then for square or rectangular films, such as ours are, these measurements will return the same resistance value. Thus, when taking data, the tradeoff has been made to eschew these variations in favor of measurement speed and data density.

We can compute the sheet resistance, $\rho = \sqrt{\rho_{xx}\rho_{yy}} = \tau R$ from the van der Pauw measurements described in 1.27 using the van der Pauw equation[17,18].

$$1 = \exp \frac{-\pi\rho_{vdP1}}{\rho} + \exp \frac{-\pi\rho_{vdP2}}{\rho} \tag{1.28}$$

Equation 1.28 is not analytically solvable, so a root-finding method must be used to solve for ρ. I will also note that since ρ must be positive, so must R_{vdP1} and R_{vdP2}. The Hall resistance, R_{xy} is more simply computed by averaging the two Hall configurations.

$$R_{xy} = \frac{R_{Hall1} + R_{Hall2}}{2} \tag{1.29}$$

Once the resistances have been computed, their associated conductivity analogs σ can be easily computed as well; however, we must compute them via matrix inversion, not simple scalar inversion.

$$\begin{aligned} \sigma &= \frac{1}{\rho} \\ \sigma_{xx} &= \frac{1}{\rho_{yy}} \\ \sigma_{yy} &= \frac{1}{\rho_{xx}} \\ \sigma_{xy} &= \frac{-\rho_{xy}}{\rho^2 - \rho_{xy}^2} \end{aligned} \tag{1.30}$$

In the thin films I measured it was often a working assumption that $\rho_{xx} = \rho_{yy}$, and some authors in literature ignore the $-$ sign for the off-diagonal conductivities to maintain that a positive Hall resistance yields a positive Hall conductivity. Rarely is it the case that a sample for which we know $\rho_{xx} \neq \rho_{yy}$ cannot be patterned and must be measured, and no such sample is discussed in this work. However, for more information about extracting ρ_{xx} and ρyy I encourage the interested reader to peruse the work of Oliver Bierwagen[18,19].

When implementing van der Pauw measurements in the lab, certain conditions, known as reciprocity conditions, must be met in order to ensure the sample is properly connected and homogeneous enough to merit measurement[17]. These are especially important to consider as the membrane revolution comes of age and questions about their transport are asked since membranes are fraught with cracks and potentially bizarre conducting pathways.

$$\begin{aligned} R_{vdP1}, R_{vdp2} &> 0 \\ |R_{vdP1} - R_{vdp2}| &= |R_{Hall1}| \\ R_{Hall1} &= -R_{Hall2} \end{aligned} \tag{1.31}$$

The Classical Hall effect

When charge is moving and a magnetic field is present, the charge feels a force, called the Lorentz force, in the direction perpendicular to both the magnetic field direction and velocity direction. When current is flowing in a conductor and a magnetic field is applied, measurement of the transverse voltage results in a measurement of the classical Hall effect. Under certain conditions, the Hall effect can tell us useful information about the material; othertimes it is simply a property of

the material that is too complex to model and extract deep insight from.

In the scenario that only one band dominates the conduction of a material, the Hall can tell us the carrier sign, density, and mobility of the material. Here I will show the case for a van der Pauw measurement on a film with a finite thickness τ. Such measurements are performed with an out-of-plane magnetic field, B (Tesla) that is sweep while continuously measuring the Hall resistance, R_{xy}, and sheet resistance R_{sq}. Under certain constraints various aspects of this procedure may be altered, but this is the standard and most-common approach.

$$\begin{aligned} n_{3D} &= \frac{1}{e\tau \frac{\mathrm{d}R_{xy}}{\mathrm{d}B}} \\ \mu &= \frac{1}{eR_{sq}\tau n_{3D}} \\ k_F l &= \frac{(3\pi)^{\frac{2}{3}}\hbar \left(\tau \frac{\mathrm{d}R_{xy}}{\mathrm{d}B}\right)^{\frac{1}{3}}}{R_{sq}\tau e^{\frac{5}{3}}} \end{aligned} \tag{1.32}$$

In equation 1.32 e is the charge of one electron, n_{3D} is the three-dimensional carrier density, and μ is the mobility. The units of μ are cm^2/(Vs) which are the units of velocity (cm/s) per electric field (V/cm), and so we think of the mobility as the increase of the steady-state velocity of net charge with increasing electric field. The parameter $k_F l$ is the product of the Fermi wavevector and the mean-free path. This dimensionless parameter is best thought of as a measure of the influence of defects on a film's conduction. Although as written it does not depend explicitly on mobility, the parameter exists within the single-band assumptions previously stated and should not be applied to metallic multiband systems. Furthermore, to extend equation 1.32 to two-dimensional systems such as LAO/STO simply set $\tau = 1$.

These equations 1.32 are ubiquitous across semiconductor labs and find a decent amount of applicability in oxide research as well. To set expectations, in the most advanced oxide electronic system, LAO/STO, typical room-temperature values for n_{2D} I measured were 10^{13} cm^{-2} and μ was 4 cm^2/(Vs), while at 2 K the mobility often exceed 10^3 cm^2/(Vs).

1.1.8 The Anomalous Hall Effect

The classical Hall effect was discovered by Edwin Hall in 1879, then in 1881 Edwin Hall discovered the anomalous Hall effect by observing that the transverse resistivity was much larger in ferromagnetic iron than in nonmagnetic conductors[20–22]. While the classical Hall effect was well undertsood and, in certain well-formed cases such as semiconductors, provides a convenient way to obtain the carrier density and mobility, the anomalous Hall effect proved much more difficult to understand. At its most basic, the anomalous Hall effect is the manifestation of a material's magnetism in the Hall voltage. As such, the emperical relationship between ρ_{xy} and M_z established has become the starting point for many analyses[20,23].

$$\rho_x y = R_0 H_z + R_s M_z \tag{1.33}$$

The result in equation 1.33 holds in many systems and allows an electrical probe to be used to study the magnetism of a sample.

While there are clear drawbacks to the direct replacement of direct magnetization measurements with the anomalous Hall effect, in some situations there are clear advantages. One such example is in magnetic thin films. Performing magnetization measurements with the common techniques of vibrating sample magnetometry (VSM) or squid requires measurement of the entire

sample, which includes the substrate. While in theory this should not be a problem because most common oxide substrates are diamagnetic, that is absolutely never the case in practice. There is a wonderful overview of all the net magnetic moments present in oxide substrates by M. Khalid called "Ubiquity of ferromagnetic signals in common diamagnetic oxide crystals" that highlights this situation for the most common oxide substrates[24]. While the observant and creative experimentalist can circumvent these issues in some cases and still produce high-quality magnetization measurements, the fact remains that this is an obstacle often faced and the anomalous Hall effect allows a way to avoid substrate contributions to the magnetism. Furthermore use of the anomalous Hall effect opens up study of magnetic layers on explicitly magnetic substrates as well.

Meanwhile, other methods that seeks to measure the magnetization directly such as the magneto-optical Kerr effect (MOKE) and Nitrogen-vacancy diamond (NV-diamond) return spatially very localized measurements of the magnetization and require careful setups of the probing devices which often perform well at room temperature. However, methods for low temperature high magnetic field measurements often involve cryogens and superconducting solenoids that quickly fetter the geometric constraints of these probes.

The anomalous Hall effect alone cannot compute the magnetization of a sample as the R_s is not nearly as simple as R_0. In fact, the scaling of R_s with ρ was a much debated topic through much of the history of the anomalous Hall effect and turns out to vary across materials systems. The different scaling behaviour has been traced to electron scattering mechanisms and scattering prevalences across materials systems. Nagaosa et al summarize the different regimes of the anomalous Hall effect[20].

- σ_{xy}^{AH} σ_{xx}^{0}. In this case the anomalous Hall effect is from the intrinsic Berry curvature.

- σ_{xy}^{AH} σ_{xx}; $\sigma_{xx} > 10^6$ (Ω -cm)$^{-1}$. In this case skew scattering dominates the anomalous Hall effect, which may itself be dominated by the classical Hall effect.

- σ_{xy}^{AH} σ_{xx}^0; $\sigma_{xx} \in \{10^4 - 10^6\}$ (Ω -cm)$^{-1}$.

- σ_{xy}^{AH} σ_{xx}; $\sigma_{xx} < 10^4$ (Ω -cm)$^{-1}$. In this case the sample is a bad metal and σ_{xy}^{AH} decreases faster than linear with σ_{xx}.

1.1.9 Berry Curvature in Electron Systems

Much of the current interest in the anomalous Hall effect is driven by the phenomena that derive from the Berry curvature. It has been linked to the intrinsic anomalous Hall effect, negative magnetoresistance, and nonlinear Hall effect[25,26]. This is relevant enough that it has made its way into the graduate classroom, and so I'll use the lecture notes for course Phys 7635 by Professor Daniel C. Ralph (unpublished) as a coarse guide to introducing the Berry curvature. The Berry curvature is a necessary term in the semiclassical treatment of electron motion, which, in a crystal experiencing an external force $\vec{F}$, can be described by two equations of motion.

$$\begin{aligned} \frac{\mathrm{d} < \vec{k} >}{\mathrm{d}t} &= \frac{1}{\hbar}\vec{F} = \frac{-e}{\hbar}\left(\vec{E} + \frac{1}{c}\frac{\mathrm{d} < \vec{r} >}{\mathrm{d}t}\right) \\ \frac{\mathrm{d} < \vec{r} >}{\mathrm{d}t} &= \frac{1}{\hbar}\nabla_{\vec{k}}\varepsilon(\vec{k} = \vec{k}_0) - \frac{\mathrm{d} < \vec{k} >}{\mathrm{d}t} \times \vec{\Omega}(\vec{k}_0) \end{aligned} \tag{1.34}$$

In equation 1.34 the electron is assumed to be in a band defined by energy ε and to stay in that band. The energy ε and Berry curvature $\vec{\Omega}$ then have values that are functions only of $\vec{k}$ for a fixed band. In the case on only an electric field $\vec{E}$ it can easily be seen that $< \dot{\vec{k}} >$ is proportional to $\vec{E}$ and substituting this result into the second equation produces a term for $< \dot{\vec{r}} >$

that is always perpendicular to $\vec{E}$. In a thin film where the electron is constrained to move in a plane, this will result in the same dynamic motion as if a magnetic field were present. And hence, the term 'fictitious magnetic field' is often used when talking about electron motion in the presence of a Berry curvature. In order to observe a Berry curvature effect, the existence of ε and $\vec{k}$ such that $\vec{\Omega} \neq 0$ is not enough, rather the integral of $\vec{\Omega}$ over the entire Brillouin zone must not be 0. The Berry curavture for electrons in a system can be nonzero when any number of the following are true: 1) inversion symmetry is broken, 2) time-reversal symmtry is broken, 3) there is strong spin-orbit coupling.

1.1.10 Frustrated Magnetism causing a Berry Curvatures

As the Berry curvature requires uncommon symmetries to make it nonzero, it is observed most commonly in uncommon magnetic strutures. These uncommon magnetic structures are frequently observed on frustrated lattices of various sorts such as triangular, Kagome, and pyrochlore.

The most simple frustrated system is an equilatoral triangle with three antiferromagnetically aligned Ising spins located at the vertices. While two of the spins can align antiferromagnetically the third cannot satisfy an antiparallel alignment with both of the other spins, making the system frustrated, as show in figure 1.5. In the case that there are Heisenberg spins instead of Ising spins the antiferromagnetic constraint abstracts to become that the sum of the spins is zero, resulting in 120^o relative alignment between the spins, but with an unconstrained global rotation state described by (θ, ϕ), as also shown in figure 1.5.

In the case of a kagome lattice the individual triangles only share vertices, but not edges as in a triangular lattice. This results in even fewer constraints and a larger ground state degeneracy of the magnetic lattice. Consequently, populating the lattice merely with the antiferromagnetic constraint

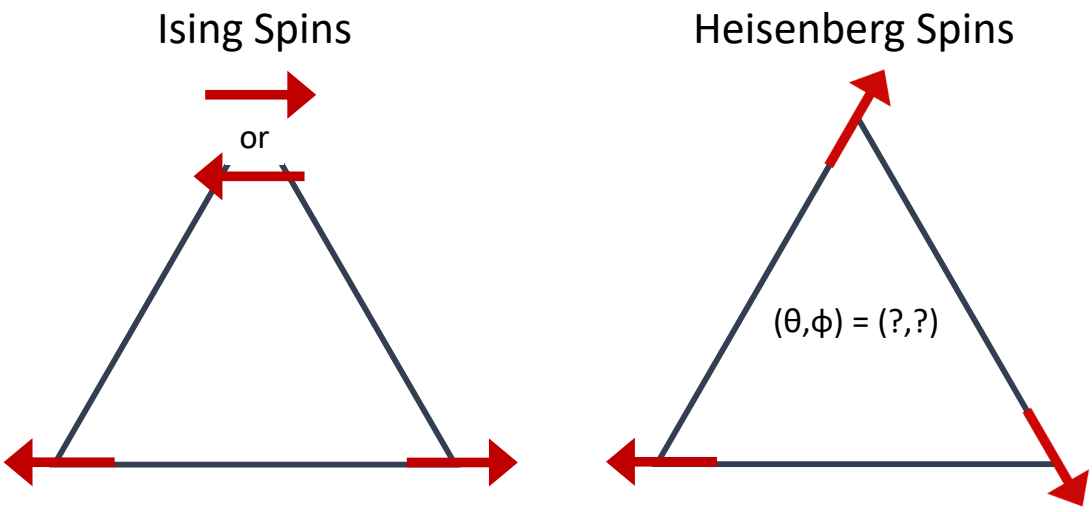

Figure 1.5: The most simple frustrated magnetic system is that of an equilateral triangle endowed with antiferromagnetically-coupled spins at the vertices. On the left the case of Ising spins is shown, while right is the case of Heisenberg spins in which 120^o relative alignment satisfies the zero-net-moment constrain, but leaves the global rotation state (θ, ϕ) unconstrained.

does not constrain the chirality of individual triangles as in the triangular lattice. An instance of the chirality switching is shown in 1.6. The lattice construction from having equilateral triangles that share only their corners creates a maximally-frustrated lattice in two dimensions. An instance of such a latticce is discussed in this work as it is the lattice of the (111) planes of antiperovskite Mn_3GaN and Mn_3NiN.

The specific magnetic structures of Mn_3GaN and Mn_3NiN both have an additional constraint that next-nearest-neighbor Mn atoms are ferromagnetically aligned[27,28]. This results in a magnetic structure that has the same translational symmetry as the atomic lattice, suppressing switched chiralities throughout the lattice. However, while both Γ^{4g} and Γ^{5g} lattices satisfy the same antiferromagnetic and ferromagnetic constraints and produce zero net magnetic moment they both will produce different Hall effects. This is a result of how the lattice symmetries match or do not with the symmetries inherent in the Berry curvature[27]. In the case of the Γ^{5g} lattice, there exist mirror

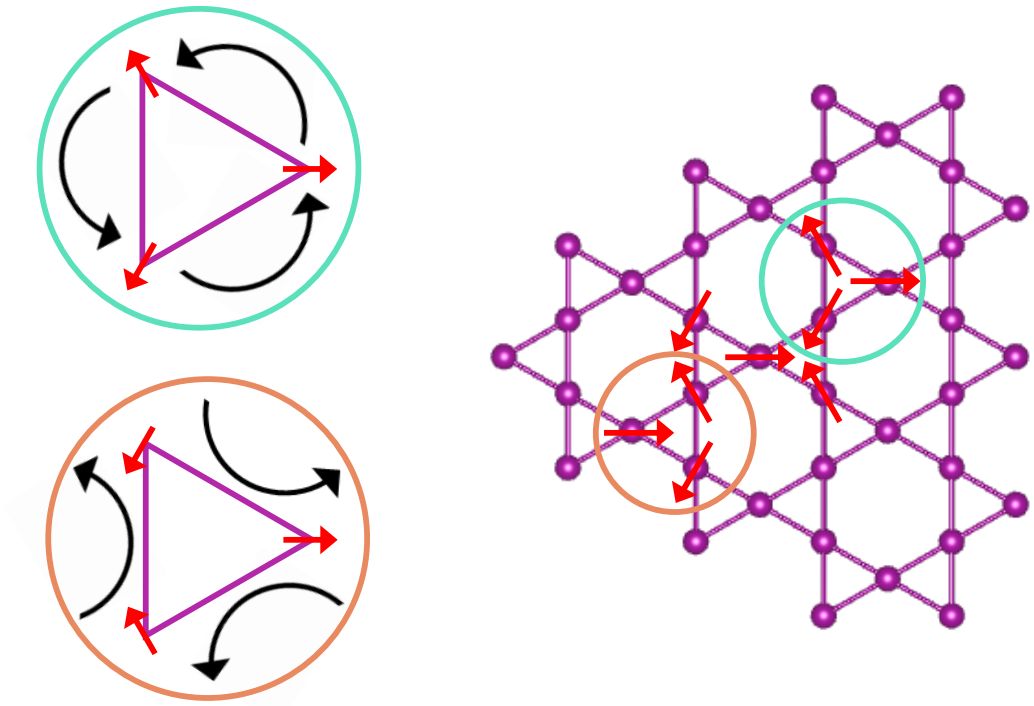

Figure 1.6: The kagome lattice on the right, when endowed with antiferromagnetic spins, is a maximally frustrated system in two dimensions. Spins that satisfy only the antiferromagnetic near-neighbor coupling constraint can create triangle with opposite chiralities. The spin configuration shwown in the green cicle exhibits right-handed chirality, while the one in a brown circle shows left-handed chirality. The kagome lattice shown here was created with Vesta[1].

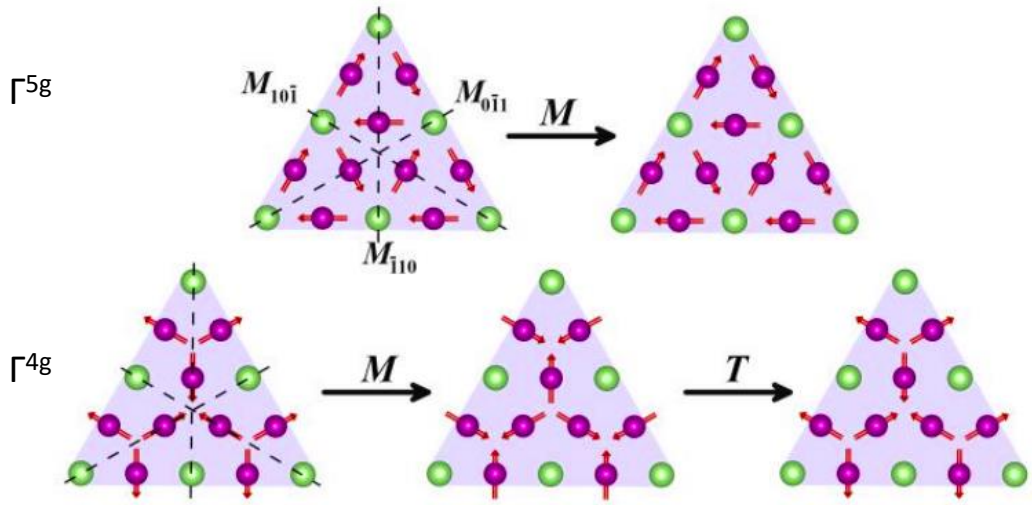

Figure 1.7: The two non collinear antiferromagnetic lattiec, Γ^{5g} and Γ^{4g} are shown along with the symmetry operations that reproduce the lattice. While the Γ^{5g} lattice is symmetric about a mirror plane, the Γ^{4g} lattice is symmetric about a mirror plane and a time reversal symmetry. When these symmetry operations are applied to the Berry curvature, they imply that it must be zero for the Γ^{5g} lattice, but can be non zero for the Γ^{4g} lattice.

planes about which the lattice is symmetric. The Γ^{4g} lattice is not symmetric about these mirror planes without an additional time-reversal operation. These symmetry operations are applied to the lattices in figure 1.7 and to the Berry curvatures in equation 1.35[27].

$$\begin{aligned} M_{\bar{1}10}\vec{\Omega}^{5g}_{xy}(k_y,k_x,k_z) &= -\vec{\Omega}^{5g}_{xy}(k_x,k_y,k_z) \\ TM_{\bar{1}10}\vec{\Omega}^{4g}_{xy}(k_y,k_x,k_z) &= \vec{\Omega}^{4g}_{xy}(-k_x,-k_y,-k_z) \end{aligned} \tag{1.35}$$

In equation 1.35 M is a mirror-plane operation, T is a time-reversal operation, and the superscripts on $\vec{\Omega}$ indicate the symmetry of the system. These imply that $\vec{\Omega}^{5g}_{xy} = 0$, while $\vec{\Omega}^{4g}_{xy} \neq 0$ over the entire Brillouin zone. These results have implications for the Hall effect due to the relationship between the Hall effect and Berry curvature in equation 1.36 that sums over all bands, indexed by n.

$$\sigma_{xy} = \sum_n \frac{e^2}{\hbar} \int_{BZ} \frac{\mathrm{d}^3\vec{k}}{(2\pi)^3} \vec{\Omega}_{xy}(\vec{k}) \tag{1.36}$$

1.1.11 $SrIrO_3$

A lot of research has been aimed at $3d$ transition metal compounds to the extent that most current research on such compounds has progressed to the engineering phase in which the fundamental properties of these films can be exploited to do neat tricks[29]. On the other hand, $5d$ compounds such at Iridates, provide a system in which physical properties are much more emergent, as discussed in the previous section. In particular, I studied Perovskite $SrIrO_3$ in thin-film form.

Perovskite $SrIrO_3$ is itself an example of the value of the thin-film platform from a simple materials-exploration perspective. Bulk samples of $SrIrO_3$ are polycrystalline and at room temperature and pressure exhibit a monoclinic symmetry[2,30]. This can be overcome by growing $SrIrO_3$ on single-crystall oxide substrates such at $SrTiO_3$, LSAT, $NdScO_3$, $GdScO_3$, and $DyScO_3$, resulting in orthorhombic metastable thin films or Perovskite $SrIrO_3$[2,30].

Single-crystal Perovskite $SrIrO_3$ films part of a structural progression known as a Ruddlesden-Popper series[31]. This structural progression was first observed in the 1950s in KNiF, then in oxides by the same researchers in SrTiO3. The general form of the chemical formula for the Ruddlesden-Popper oxides is $A_{n+1}B_nO_{3n+1}$ and most commonly $n \in 1, 2, \infty$. Ruddlesden-Popper phases are known for the 2D nature of the BO_2 planes which are separated by n ABO_3 layers. Increasing n is concomittant with an increased a lattice parameter, making the Perovskite ($n = \infty$) phase the largest at $3.95\mathring{A}$ and the 214 phase ($n = 1$) the smallest at $3.88\mathring{A}$[2,32].

As an aside, why would an orthorhombic material be characterized by a single lattice parameter

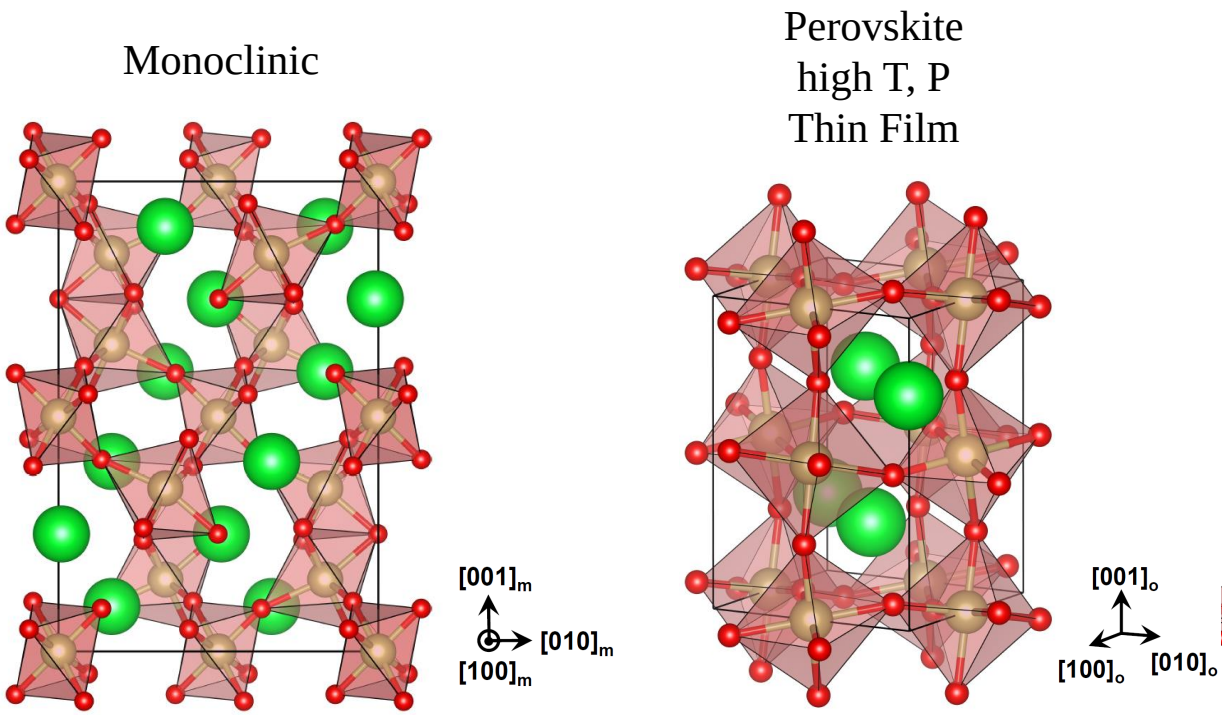

Figure 1.8: $SrIrO_3$ only forms a monoclinic phase without high temperature and pressure, but even this is still polycrystalline. Growing thin films of $SrIrO_3$ allows single crystal Pervskite forms to stabilize and be studied. The Perovskite phase differs notably in that the Oxygen octahedra only touch at ther vertices, never along the sides as in the monoclinic form. The vesta[1] images shown here were created by TJ Anderson for a manuscript[2] and arranged here by me.

a? In this case, what I refer to is the pseudocubic lattice constant, sometimes referred to as a_{pc}. The actual orthorhombic lattice constants for $SrIrO_3$ are $a = 5.60\mathring{A}$, $b = 5.58\mathring{A}$, and $c = 7.89\mathring{A}$. I will note that $5.60 \approx 5.58$ and $5.60/\sqrt{2} = 3.96$ and $7.89/2 = 3.945$. Being guided by this intuition, in fact such a transformation yields a cell of slighty-distorted atoms that look like figure 1.1. Since I studied films grown on cubic $SrTiO_3$, and effects such as the crystal-field effect are best understood using this cell, we call this the pseudocubic unit cell, and describe $SrIrO_3$ with one lattice parameter a. This can be extended to the rest of the Ruddlesden-Popper series, but only for two dimensions, as the third dimension lacks the atomic symmetry.

As a result of $5d$ orbitals and relative stability, $SrIrO_3$ was a strong candidate for showing topologically-interesting electronic transport. In 2012 Carter et al proposed a topological insulator system based on a line node in $SrIrO_3$, but ultimately the constraints of growing epitaxial thin films proved to dismantle the topological protection of the band structure[33–35].

1.1.12 Mn_3GaN and Mn_3NiN

While a lot of my time has focused on oxide materials, I also spent a significnat amount of time on two nitride materials, Mn_3GaN and Mn_3NiN. These two materials are part of a class of materials known as antiperovksite nitrides. The name antiperovskite comes from the similar but inverted cation/anion structure. The anion, Nitrogen in this case is at the body center of the unit cell, and the Mn cation sits at the face centers. The similarity in their structures enables these antiperovskites to be grown in single-crystal epitaxial thin films on standard oxide substrates such as $SrTiO_3$ and LSAT[36]. This even turned out to help grow single-crystal Mn_3Ga, a promising ferrimagnetic material that had languished due to the inability to synthesize films with a uniform magnetization direction. This is further discussed in a later chapter.

As is probably obvious, the structural change between antiperovskites and Perovskites causes a significant difference in the material properties. First, while Perovskite oxides are generally classified as ceramics and one would not be faulted for assuming they are all insulating, antiperovskite nitrides are metals in the textbook sense[5,7]. They are ductible and have many bands crossing the Fermi level. What makes these materials interesting is the magnetic stucture that sits on the Mn sublattice. While in Perovskite oxides the potentially-magnetic B-site cation resides at the body center of the unit cell, in antiperovskites, it sits at the face centers and thus has siginificantly different coordination. For intuition, in Perovskites the nearest-neighbors to the B-sites cations in the B-site sublattice are other B-sites with a distance of a, or one unit cell, and coordinated through an Oxygen anion. In antiperovskites, the Mn nearest neighbors in the Mn sublattice are Mn atoms on adjacent faces, at a distance of $a/\sqrt{2}$ and have no atom directly between them, while the next-nearest neighbors are a away and are coordinated through a N atom. This results in the nearest-neighbor Mn atoms having a negative exchange interaction and tend toward aligning antiferromagnetically, while the next-nearest neighbors have a positive exchange interaction and tend toward ferromagnetic alignment.

The result of this tension is a non-collinear antiferromagnetic Γ structure, where Γ indicates that the magnetic structure has the same translational symmetry as the atomic structure[37]. Focusing on the (111) plane in figure the Mn local moments are constrained to lie in the (111) plane, and the Mn sites form a Kagome lattice[27,28]. Such a magnetic structure can be decomposed into a Γ^{4g} and Γ^{5g} contributions. Relevantly, the Γ^{4g} structure can be shown to break the relevant symmetries to have a nonzero Berry curvature due to the pseudo-vectore nature of the spins, while the Γ^{5g} variant does not[27].

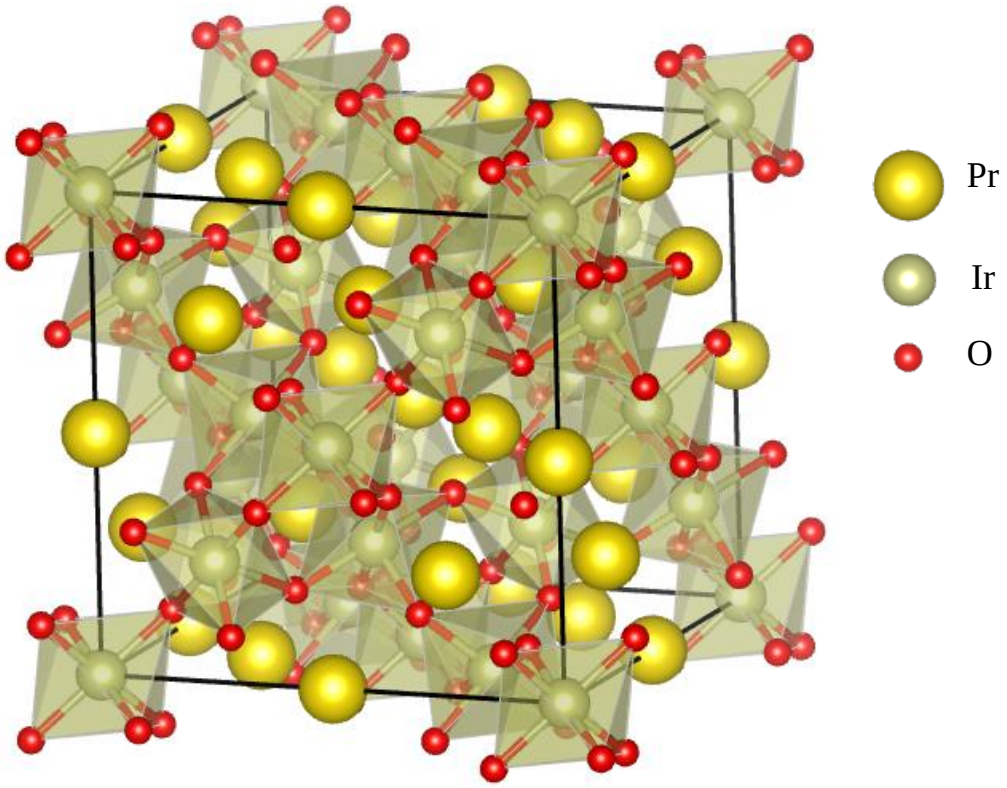

Figure 1.9: $Pr_2Ir_2O_7$ forms in a pyrochlore structure. The unit cell is so large because of the 'missing' Oxygen atom. While this is not a Perovskite material, the chains of Ir-O atoms that run three-dimensionally through the Pr cations are reminiscent of the basic electronic structure of Perovskite oxides. This image was generated with vesta[1].

1.1.13 $Pr_2Ir_2O_7$

If one or both of $SrIrO_3$ or Mn_3NiN sounded interesting, pyrochlore $Pr_2Ir_2O_7$ is definitely interesting as it combines aspects of both previously-discussed materials. The structure of pyrochlore $Pr_2Ir_2O_7$ is inherently three dimensional, and is best thought of as two interlacing sublattices, one of coordinated Pr and the other of coordinated Ir as showin in figure 1.10. The interesting properties come from the combination of the Ir sublattice and the frustrated Pr sublattice. My research focused primarily on our finding that in thin films the Ir sublattice mimicked some properties of the Pr sublattice. So here I will focus on the Pr sublattice.

The Pr sublattice consists of Pr atoms arranged in vertex-sharing tetrahedra as in figure 1.9 and 1.10. Each Pr cation is coordinated with Oxygen atoms that are not shown for clarity. The Pr tetrahedra vertexes are occupied by cations that have local net moments of about $2.7\mu_B$/Pr, and have a negative exchange interaction favoring antiferromagnetic, which is frustrated by the geometry of the lattice[38]. The result is that each Pr atom has a local Ising magnetic spin that points either toward the center of the tetrahedron or away from the center of the tetrahedron. The vertex-share nature of the tetrahedra puts further constrains on the local magnetic configurations, resulting in the three classifications of '2-in-2-out,' '3-in-1-out,' and 'all-in-all-out.' Machida et al link the '2-in-2-out' state to an observed intrinsic anomalous Hall conductivity about the [111] axis by considering a tight-binding model for the Ir $5d$ t_{2g} combined with spin-orbit coupling and importantly an antiferromagnetic Kondo coupling to the Pr $4f$ moments[38]. The '2-in-2-out' state most closely satisfies the condition that next-nearest-neighbor Pr spins be ferromagnetically aligned.

In single crystals of pyrochlore $Pr_2Ir_2O_7$ a non-zero σ_{xy} was observed below 1K while magnetic measurements showed no net magnetic moment above 0.3 K. Thus, in the temperature range from 0.3 - 1.0 K there is a macroscopically broken time reversal symmetry, but no long-range magnetic order. As long-range magnetic order is by far the most common culprit behind a broken time reversal symmetry, this observation demands a different source of symmetry breaking. In this case it is the scalar spin chirality which is the solid angle subtended by three adjacent spins.

$$\kappa_{ijk} = \vec{S}_i \cdot \vec{S}_j \times \vec{S}_k \tag{1.37}$$

The scalar spin chirality offers a nice explanation for spin-liquid states as the contributing spins

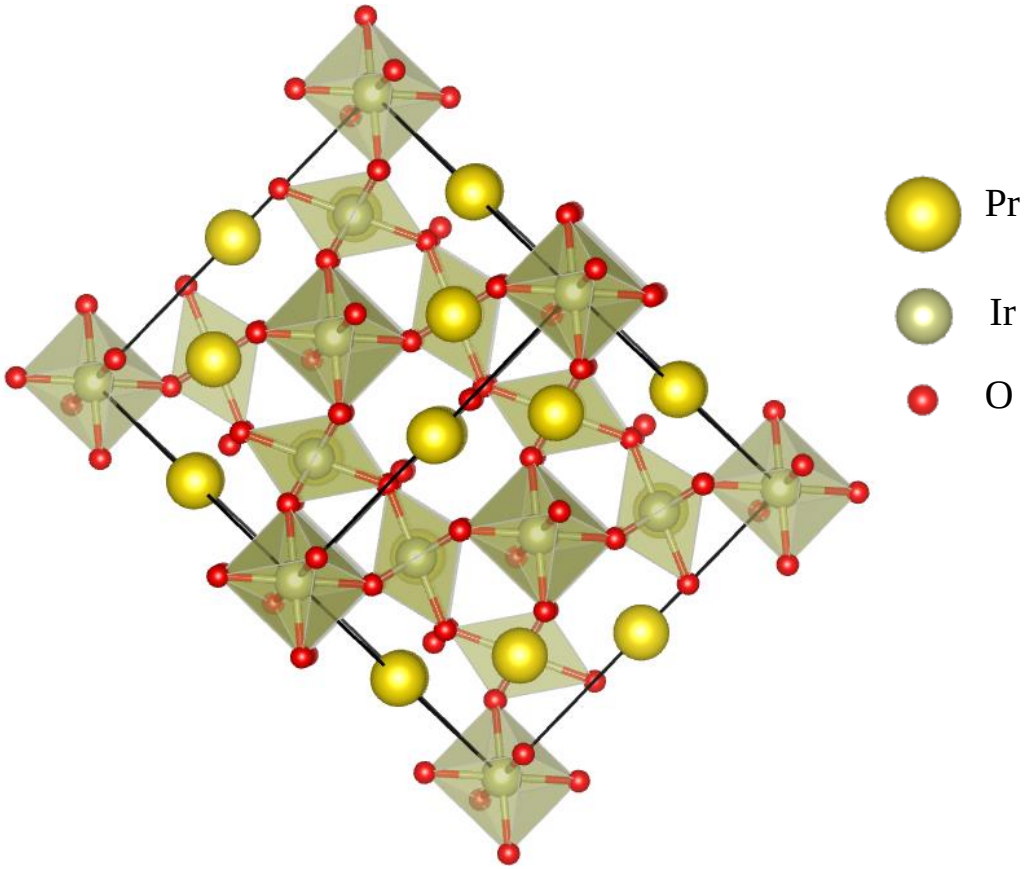

Figure 1.10: When viewed along the [011] zone axis the geometry of the Ir_6 network is apparent in pyrochlore $Pr_2Ir_2O_7$. This image was generated with vesta[1].

need not show a global long-range order in order or net magnetic moment in order to produce an anomalous Hall conductivity.

Chapter 2

Pyrochlore Iridate

2.1 Context and My Contribution

The work in this chapter is the result of many people working together and could not exist without each persons' individual contribution. This project had film growth contributions from Lu Guo in the research group of Chang-Beom Eom, structural characterization and analysis of TEM measurements from Huaixun Huyan and Linze Li of Xiaoqing Pan's research group, and beamline Xray spectroscopy and structural characterization from Yongseong Choi, Jong-Woo Kim, and Phil Ryan at Argonne National Lab. My own contributions included electrical and magnetic measurements of $Pr_2Ir_2O_7$ thin films, identifying the XMCD technique as valuable and advocating for the measurement of $Pr_2Ir_2O_7$ films at Argonne, and consensus building and manuscript writing and modification that resulted in the final publication.

The original conception for attempting to grow pyrochlore $Pr_2Ir_2O_7$ came from some combination of Professor Chang-Beom Eom and his graduate student, Lu Guo. Once Lu had successfully navigated the difficult process of synthesizing pyrochlore $Pr_2Ir_2O_7$, which involved depositing an

amorphous film onto the substrate then annealing the film to achieve crystallinity (a process called solid-state epitaxy), I was brought onto the project to help try to conceive an interesting experiment to do with Lu's films. While the synthesis of these films was a very nontrivial challenge, ultimately, the solid-state epitaxy process does not result in films as high quality as were desired for the originally-planned work. I planned a basic characterization of Lu's highest-quality pyrochlore $Pr_2Ir_2O_7$ film which included electric and magnetic measurements, from which I observed that Lu's $Pr_2Ir_2O_7$ film displayed Hall behavior reminiscent of some results in bulk samples, but with different temperature scales. Bulk samples only showed this Hall effect phenomenon below 1 K, while my data showed it up to 15 K.

While at first this was exciting, since the bulk effect was a spontaneous ordering of Pr moments, the energy scales were such that extending this phenomenon to temperatures $>$ 10x the original observation was not a feasible explanation. At this point I worked with Lu to design additional pyrochlore $Pr_2Ir_2O_7$ films to check reproducibility. The magnitude of the novel low-temperature Hall effect decreased with decreasing film quality, but was reproduced enough to give me confidence to push to investigate the source of this effect via X-ray magnetic circular dichroism experiments to investigate magnetic ordering. Beamtime became available when another the project of group member no longer required the projects original measurements. Lu and I worked together to propose pyrochlore $Pr_2Ir_2O_7$ films as the substitute project. I worked with Lu on determining which samples to measure, and we worked with the beamline team to understand their beamline results, and to integrate them into our understanding of thin-film pyrochlore $Pr_2Ir_2O_7$. The result of this research is presented in the remainder of this chapter largely kept to the published form. The manuscript was written with large contributions by Lu Guo, the beamline team led by Dr. Phil Ryan, and me. Ultimately, most of the manuscript organization and final editing were done by me,

although the ideas were heavily shaped by working with Lu and discussing the research with the beamline team.

2.2 Spontaneous Hall effect from local Ir moments in $Pr_2Ir_2O_7$ thin films

Rare-Earth pyrochlore Iridates have been the subject of much research interest as a result of predictions and observations of phenomena such as bulk and edge massless conduction, frustrated magnetism, and metal-insulator transitions[4,38–41]. The key to the intriguing properties of $RE_2Ir_2O_7$ is the intimate coupling of two disparate sublattices of ionic RE and conducting Ir cations, as well as connecting oxygens. Each sublattice consists of alternating triangular and Kagome planes that are more easily visualized as forming a corner-sharing tetrahedra network (Fig 2.1). The high coordination of the lattice allows significant overlap of Ir orbitals simultaneous with frustrated magnetism of the RE ions.

The RE magnetic exchange interactions are mediated by the conducting Ir bands through the Ruderman–Kittel–Kasuya–Yosida (RKKY) interaction[4]. As a result of the lattice geometry and antiferromagnetic nearest-neighbor coupling, spins on the RE and Ir sublattices are constrained to point toward or away from the center of one of the adjacent tetrahedra, forming frustrated spin-liquid correlations as examples are shown in Fig 2.1(b)-(c). The RE ions have typical local moments of a few Bohr magnetons[4], while the Ir ions have a smaller moment which can be local or delocalized[3,42]. Ir adds to the complexity due to its strong spin-orbit coupling, mixing together the orbital and spin degrees of freedom.

In the $RE_2Ir_2O_7$ family, bulk$Pr_2Ir_2O_7$ is unique in that it is metallic down to the lowest tempera-

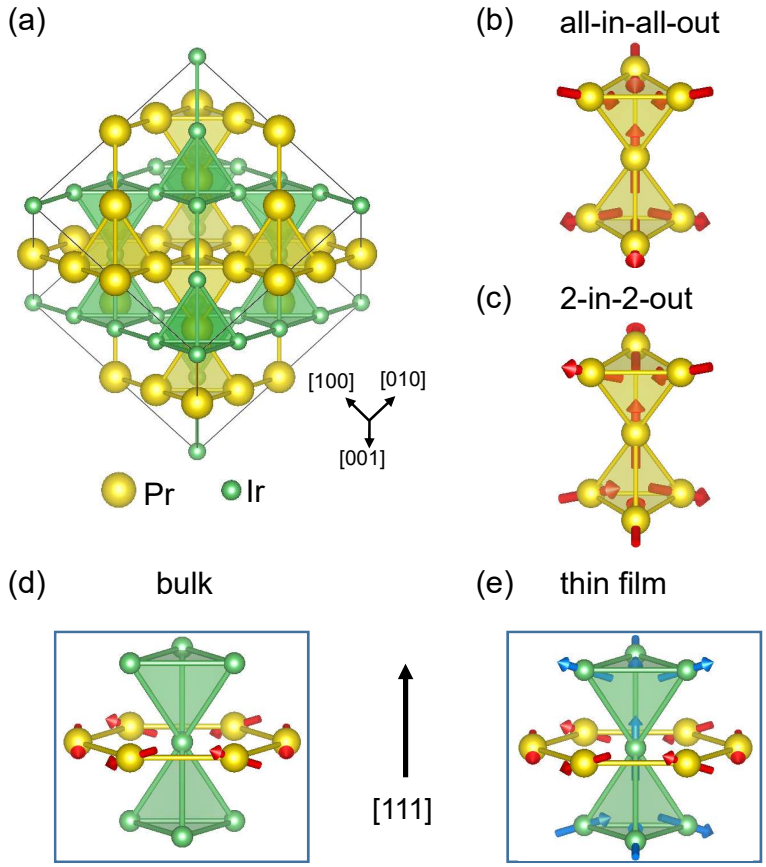

Figure 2.1: (a) Unit cell of $Pr_2Ir_2O_7$ with only cation sublattices shown. Oxygen atoms are not shown for clarity. (b, c) 'All-in-all-out' and '2-in-2-out' spin configurations on the Pr corner sharing tetrahedra. (d, e) Zoom-in of corner-sharing Ir tetrahedral surrounded by Pr hexagonal ring in the (111) plane of the bulk and thin film respectively. The red arrows in the Pr atoms indicate the Pr $4f$ moments. Due to the cubic symmetry-breaking in the thin film, Ir local moments can be established indicated here in (e) by the blue arrows in Ir atoms.

tures and shows topological Hall effect below 1.5 K as a result of various two-in-two-out magnetic configurations at the Pr sites with no net magnetic moment or long-range order. Furthermore, in thin films this topological Hall effect was observed at elevated temperatures up to 50 K[43]. While there has been speculation about the role of Ir in this effect[43], here we combine Hall measurements, synchrotron X-ray diffraction and spectroscopy techniques to provide direct evidence supporting the emergence of Ir local moments, induced by the vanishingly small lattice modification of the Ir sublattice in the epitaxial $Pr_2Ir_2O_7$ thin films. We show a definitive link between the emergence of Ir local moments, which are absent in bulk $Pr_2Ir_2O_7$, and the increased onset temperature of the spontaneous Hall effect in the films.

To study the Hall effect in $Pr_2Ir_2O_7$ thin films, we synthesized stoichiometric epitaxial relaxed films via the solid-phase-epitaxy method, see supplemental information for details[44]. The high resolution Scanning Transmission Electron Microscopy (STEM) image across the interface between the film and substrate, as shown in Fig 2.2(g), together with X-ray diffraction in Fig 2.2(a)-(f), confirms a good epitaxial relationship and a sharp interface. Moreover, the modulated intensity contrast in Fig 2.2(g) arises from an atomic number modulation between columns, indicating an atomic arrangement in the film that matches the ordered pyrochlore lattice. Energy Dispersive x-ray Spectroscopy (EDS) confirms the cation ratio between Pr and Ir is almost $1:1$ (Fig 2.3(g)). While the pyrochlore structure is nominally cubic, the synchrotron X-ray diffraction study shows different d-spacing for the (6010) and $(0\bar{6}10)$ reflections, which are equivalent under cubic symmetry. This points toward a breaking of the cubic symmetry in our epitaxial $Pr_2Ir_2O_7$ thin film; however, the distortion is too small for us to discern the specific symmetry of the lattice from the X-ray diffraction study. There are indications that a trigonal distortion of the Ir sublattice can change the electronic and magnetic properties of $Pr_2Ir_2O_7$[44]. However our result pushes the lower limit

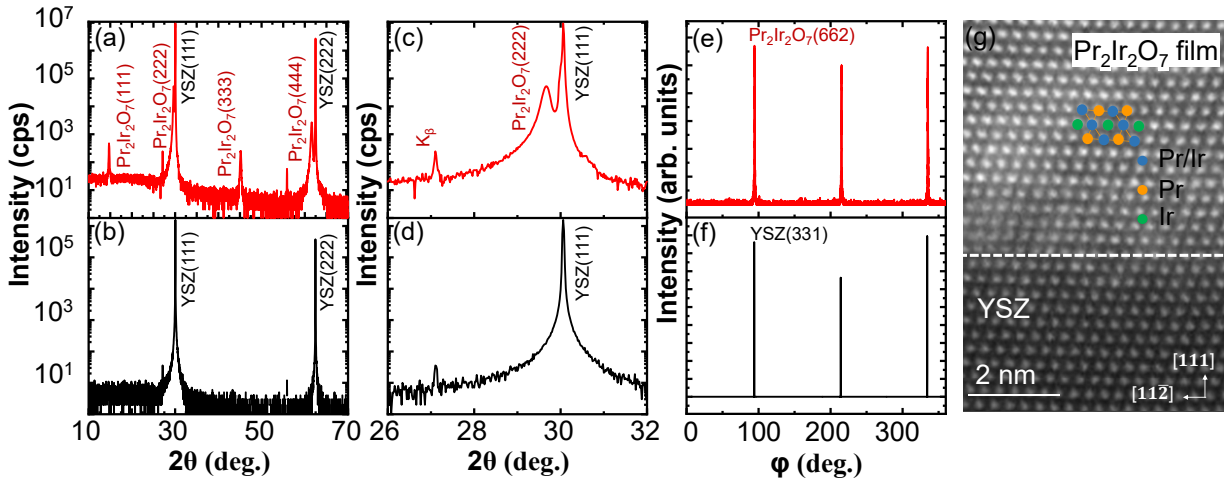

Figure 2.2: Out-of-plane $2\theta - \omega$ scan of (a) the post-annealed and (b) the as-grown film. Zoom-in out-of-plane $2\theta - \omega$ scan near YSZ (111) peak of (c) the post-annealed and (d) the as-grown film. The peak at 270 in both scans are reflections from substrate with Cu Kβ wavelength. Phi-scan patterns of the (e) $\{662\}$ planes from the epitaxial crystalline $Pr_2Ir_2O_7$ thin film and (f) $\{331\}$ planes from the YSZ (111) substrate. (g) Cross-sectional HRSTEM image across the interface between epitaxial$Pr_2Ir_2O_7$ thin film and (111) YSZ substrate. The Pr, and Ir atomic positions labeled in the selected areas are consistent with pyrochlore structure. The blue dots represent the mixed Pr and Ir column due to the alternating arrangement along zone axis. The O atoms are omitted.

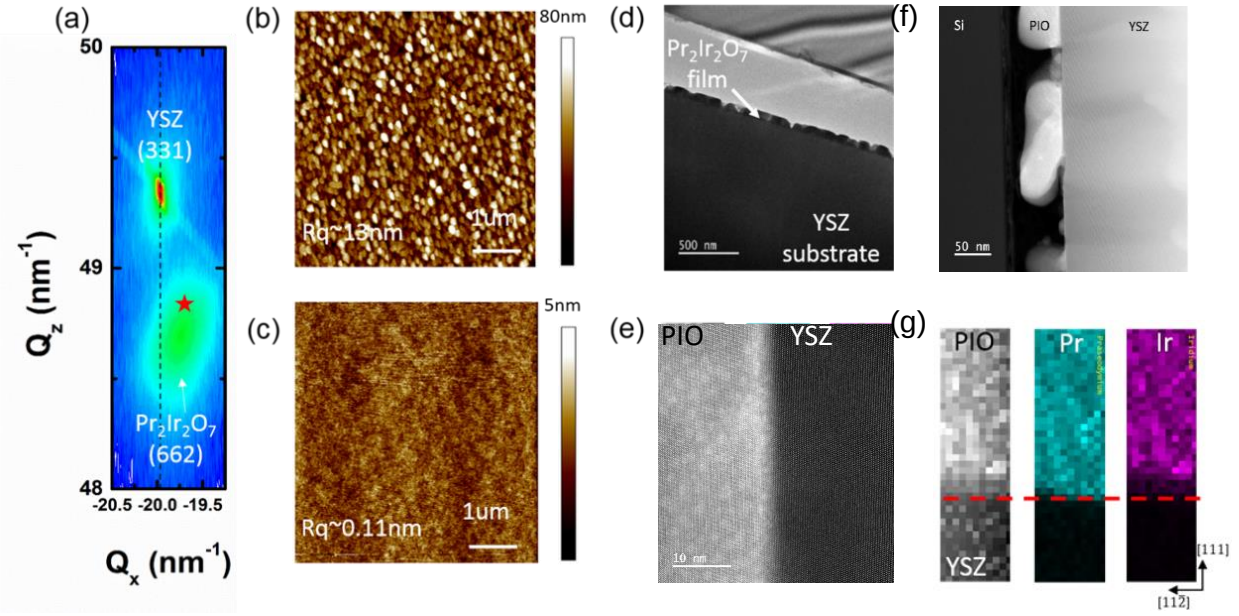

Figure 2.3: (a) Reciprocal space map around YSZ (331) and Pr2Ir2O7 (662) reflection peaks. The red star indicates the (662) reflection peak from bulk Pr2Ir2O7. Atomic Force Microscopy topology results of (b) the post annealed epitaxial crystalline Pr2Ir2O7 thin film and (c) the as-grown amorphous Pr2Ir2O7 thin film. (d) Low magnification STEM cross section images. (e) High magnification STEM cross section images with larger probe area. (f) STEM image on a specific crystallite in the film. (g) EDS mapping across the interface between crystalline Pr2Ir2O7 thin film and YSZ substrate. The red dotted line indicates the location of interface based on EDS.

of the lattice distortion necessary to effectively alter the Ir local electronic environment enough to produce the spontaneous Hall enhancement.

We use Hall measurements to study the electronic and magnetic manifestations of minor lattice distortions in the epitaxial $Pr_2Ir_2O_7$ films. Fig 2.4(b) shows the Hall signal at different temperatures with applied magnetic field along the $[111]$ direction. At temperatures below 20 K, the Hall conductivity is non-linear, becomes hysteretic, and develops a small remnant value at zero field, referred to here as the spontaneous Hall effect. A similar effect is observed in the bulk single crystal, but only at temperatures an order of magnitude lower[38,43]. The origin of such effect most commonly occurs from a spontaneous net magnetic moment via the anomalous Hall effect. We rule out this contribution based on our x-ray measurements, which indicate the net Ir moment is

less than $0.05\ \mu_B$/Ir at 5 T and the film lacks long-range magnetic ordering (Fig 2.5). Consequently, we conclude that the spontaneous Hall effect in the film arises from the topological Hall effect. In this case, the time-reversal symmetry is broken from the frustrated spin-liquid correlations rather than a net magnetic moment.

Since the RE and Ir cations are both magnetically active, we use element-resolved x-ray magnetic scattering and spectroscopy to explore the individual Pr and Ir sublattice contributions to the spontaneous Hall effect. X-ray resonant diffraction measurements at the Ir L_3 edge of our thin films from 65 K down to 5 K, covering the temperature regime above and below the observed onset of the spontaneous Hall effect, show no clear indications of any type of long-range magnetic ordering (Fig 2.6) including Ir-site AIAO ordering, consistent with the intrinsic bulk single-crystal behavior.

To help us understand the $Pr_2Ir_2O_7$, we compare the Pr L_2-XMCD results of our thin film with that of cubic-symmetric $Pr_2Ir_2O_7$ powders. Comparison of film Pr L_2-XMCD peaks (Fig 2.7) and the reference powder peaks (Fig 2.9) suggests that Pr spins behave identically in films and powders. In addition, the field dependence of the Pr L_2-XMCD signal from the film (Fig 2.8(a)) resembles the magnetometry result from the powder sample (Fig 2.5(a)). These results suggest that the structural distortion in the film does not modify the Pr magnetism. This makes sense as the Pr $4f$ orbitals are fairly localized and overlap less with the distorted surrounding atoms. This contrasts sharply with the Ir $5d$ orbitals that are much more dispersive and so more susceptible to structural distortion effects. Previous studies have shown that distortion of the IrO_6 octahedra in Perovskite iridate superlattices induces long-range magnetic ordering and an insulating ground state[45].

To investigate potential changes in the Ir magnetism in the films, we compared the Ir $L_{2,3}$ X-

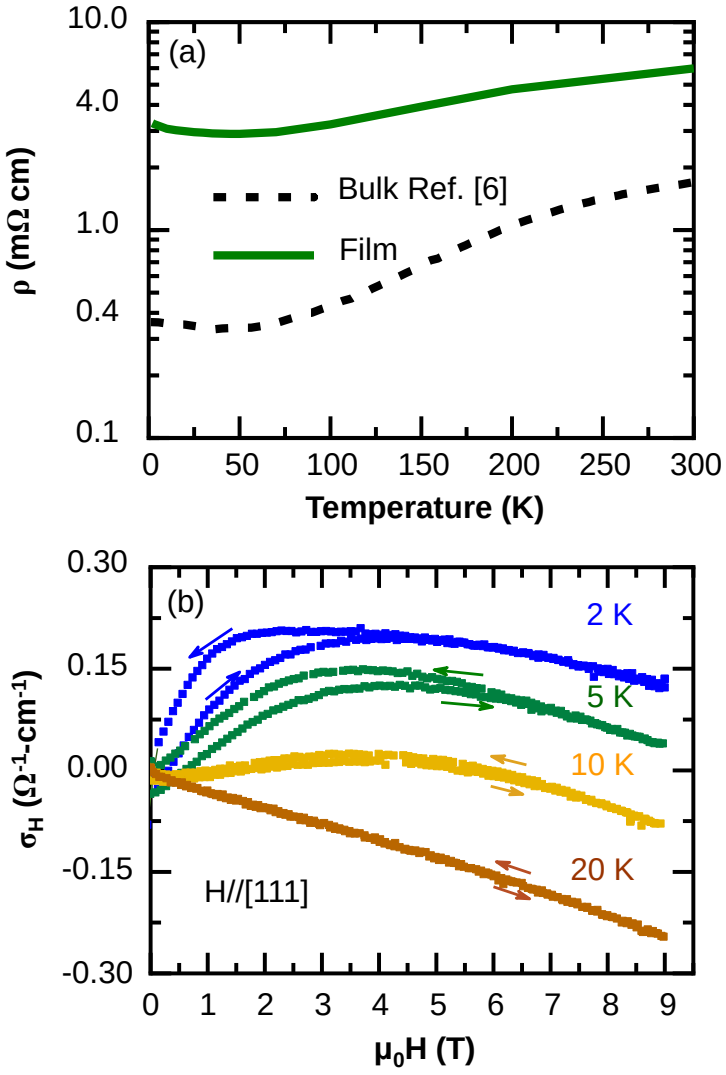

Figure 2.4: (a) Temperature dependence of the longitudinal resistivity of the epitaxial $Pr_2Ir_2O_7$ thin film (solid green line) and the bulk $Pr_2Ir_2O_7$ single crystal (black dashed line) from[3]. (b) Hall conductivity as a function of external out-of-plane magnetic field at different temperatures.

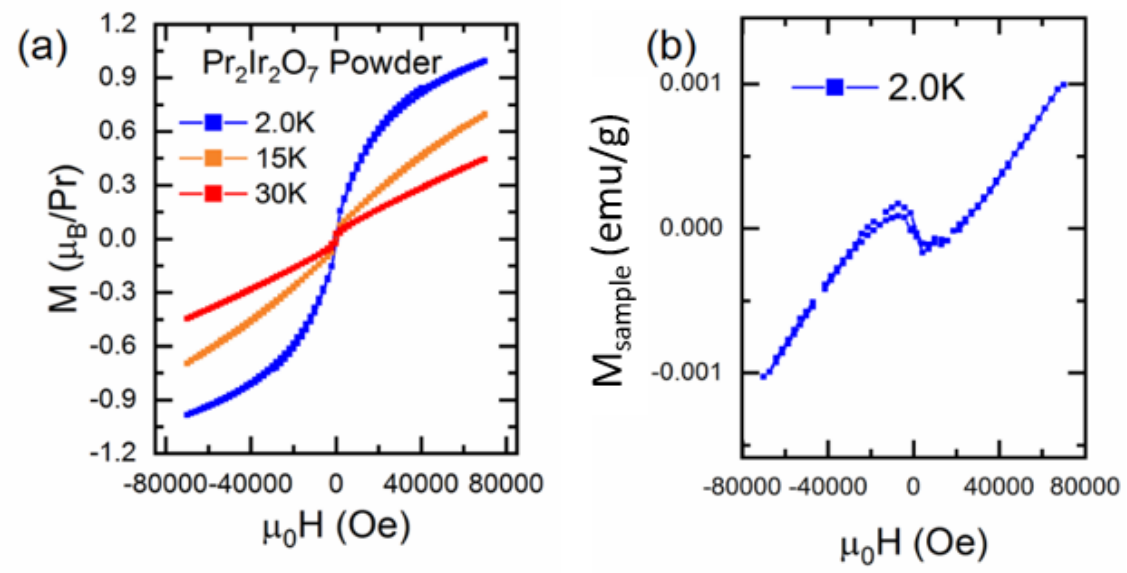

Figure 2.5: (a) M vs B curve measured by SQUID on Pr2Ir2O7 powders at different temperatures. The inset labels describe the measurement temperature. (b) M vs B curve measured by SQUID on Pr2Ir2O7 thin film sample at 2K. The signal mostly comes from the substrate rather than the Pr2Ir2O7 film.

ray absorption spectra (XAS) and XMCD data from the $Pr_2Ir_2O_7$ film with$Pr_2Ir_2O_7$ and Sr_2IrO_4 powders. As shown in Figs 2.10 and 2.11, the absorption edge positions and the L_3/L_2 branching ratios are similar for both powders, as well as the film, and also with previously studied $SrIrO_3/La_0.3Sr_0.7MnO_3$ [42], confirming large spin-orbit coupling and a Ir^{4+} electronic environment in all materials [13]. Despite the similarity of the Ir orbital state, the XMCD signal under 5T on $Pr_2Ir_2O_7$ powders at the Ir L_3 edge is less than 10% of that in Sr_2IrO_4 powders. The observed weak Ir-XMCD value is expected due to the lack of long-range ordering on the Ir $5d$ moments [38]. Furthermore, the Ir-XMCD results here differ significantly from the cases related to spin-orbit coupled Ir local moments with strong orbital magnetic moments [3,42]. Unexpectedly, the Ir-L_3 XMCD sign from the $Pr_2Ir_2O_7$ powder indicates that the Ir induced moments are anti-parallel to the external field, in sharp contrast to the Sr_2IrO_4 case, which shows long-range ordered moments with a net moment of $0.05\mu_B$/Ir [3]. Disparate Ir-L_2 XMCD signals seen in these powder samples pro-

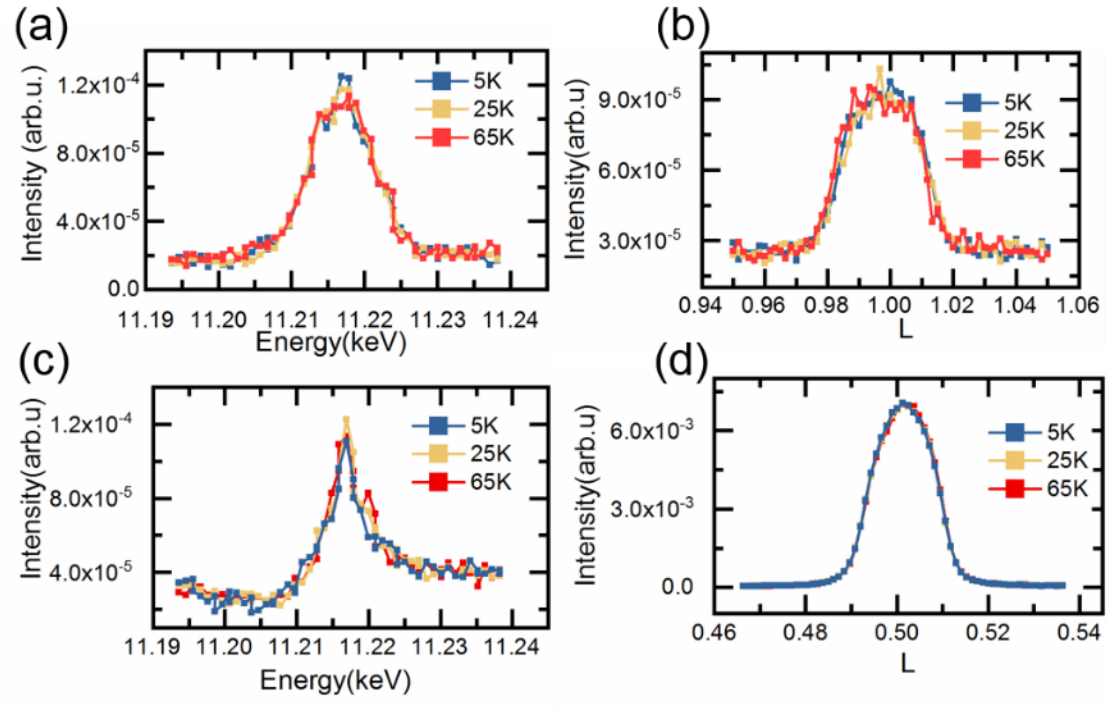

Figure 2.6: Resonant X-ray scattering with incident X-ray tuned near the Ir L edge. (a) and (b) summarizes the energy dependence and l scan of (0 0 2) peak at 5K,25K and 65K, respectively. (c) and (d) summarizes the energy dependence and l scan of (111) peak at 5K,25K and 65K, respectively.

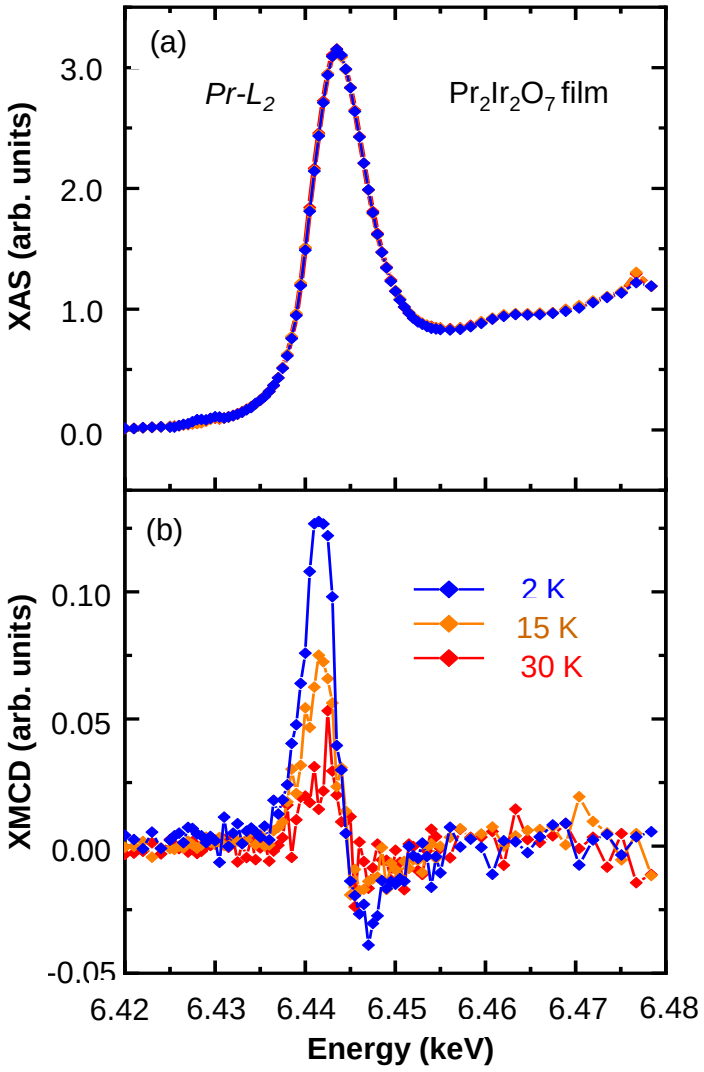

Figure 2.7: (a) XAS and (b) XMCD spectra at the Pr L_2 edge under 5T magnetic field (along [111] direction) on $Pr_2Ir_2O_7$ thin films through the spontaneous Hall effect transition.

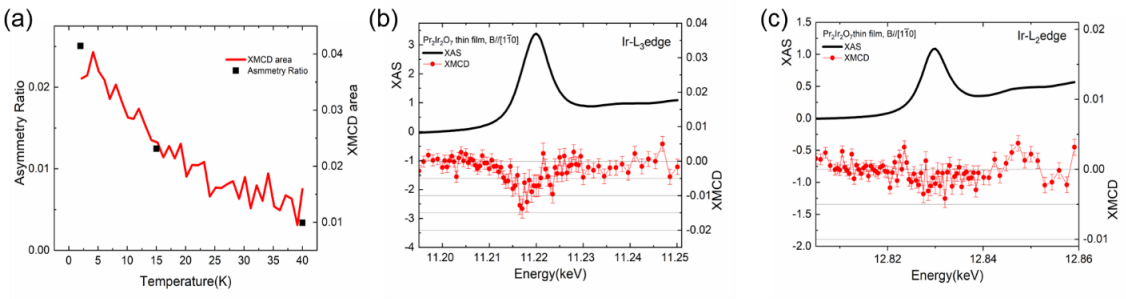

Figure 2.8: XAS and XMCD on the $Pr_2Ir_2O_7$ film. (a) The asymmetric ratio from XMCD signal at the Pr L_2 edge from 2K to 40K under 5T. (b) ,(c) The XAS (the black solid lines) and the XMCD at 2K under 5T (the red solid circles) with magnetic field along $[1-10]$ at the Ir L_3 ,and L_2 edge, respectively.

vide clues to understand the discrepancy in the Ir-L_3 XMCD signals and the overall magnetism in these two materials. Whereas the negligible Ir-L_2 XMCD signal (in comparison with the L_3 signal) from the Sr_2IrO_4 is the characteristic signature of the $J_{eff} = 1/2$ state, the $Pr_2Ir_2O_7$ powders show comparable amplitudes with opposite signs between the Ir L_2 and L_3 edges. This reveals that the observed Ir spin moments in the $Pr_2Ir_2O_7$ powder samples originate from small spin polarization in the conduction band by Pr moments, distinctively different from localized Ir moments in the Sr_2IrO_4 case. This is in accordance with resistivity results which suggest small conduction electron magnetization via the Kondo effect as shown in Fig 2.4(a).

We now discuss the difference between $Pr_2Ir_2O_7$ film and powders, in particular that our XMCD data show a magnetically active Ir sublattice in the film, as opposed to the weak polarization of the Ir spins we observed in powders. The Ir-XMCD signals in the film are an order of magnitude larger than in the $Pr_2Ir_2O_7$ powder, indicating a field-induced alignment of local Ir moments, as shown in Fig 2.10. The sign of Ir-L_3 XMCD in the $Pr_2Ir_2O_7$ thin film, contrary to that of the $Pr_2Ir_2O_7$ powders, indicates that the net Ir moment aligns with the external field, and thus is parallel to the Pr $4f$ net moment. Moreover, the much smaller XMCD signal at the L_2 edge

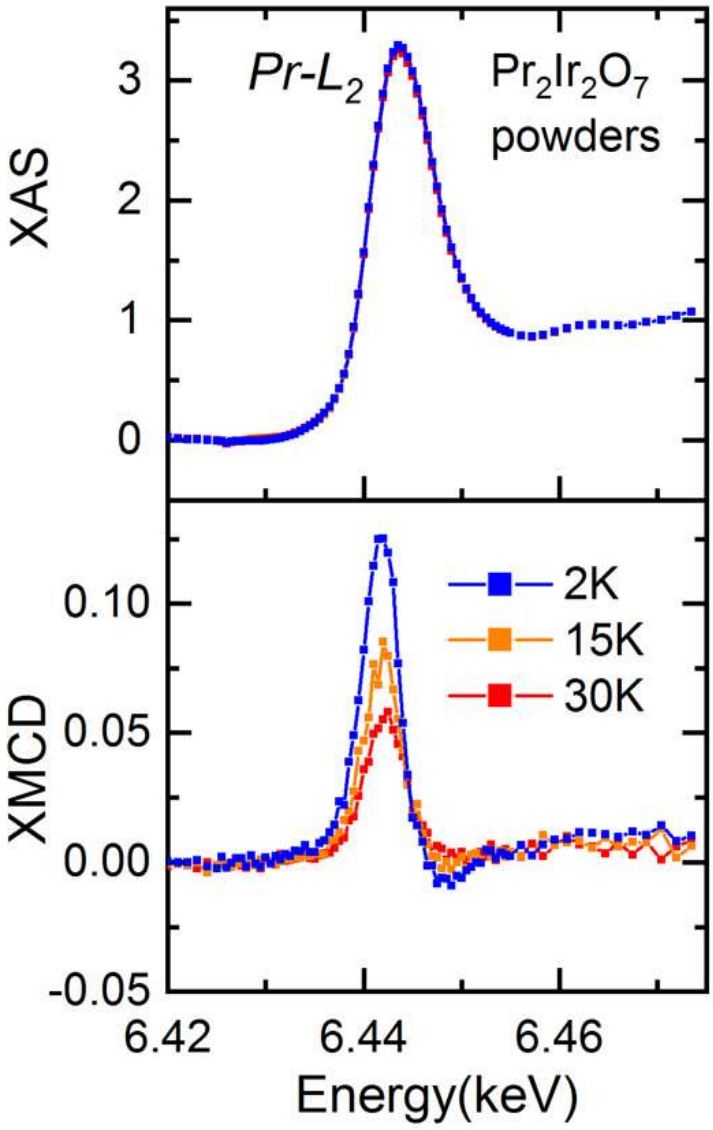

Figure 2.9: The temperature dependent XAS(the solid lines) and XMCD(the solid circles) at the Pr L_2 edge under 5T on the $Pr_2Ir_2O_7$ powders at different temperatures.

relative to L_3 suggests that, unlike the $Pr_2Ir_2O_7$ powder, the Ir $5d$ electronic state in the $Pr_2Ir_2O_7$ thin film is close to the $J_{\text{eff}} = 1/2$ state which is observed in Sr_2IrO_4[3,42]. We thus conclude that the vanishingly-small structural distortion present in our thin films has a profound impact on the electronic properties by localizing the Ir moments and changing the Ir t_{2g} manifold toward the $J_{eff} = 1/2$ observed in other iridates[46].

Our findings are also consistent with the theoretical predictions that a trigonal distortion of the Ir sublattice can enhance the formation of Ir local moments[47]. Previous theoretical work suggested a trigonal distortion of the Ir sublattice can affect the octahedral crystal field and result in non-trivial topological phases in $RE_2Ir_2O_7$ by stabilizing the AIAO spin configuration at Ir sites[44]. Our results highlight the disproportionate effect of a trivial lattice distortion on the Ir sublattice inducing incipient Ir $5d$ local moments as a manifestation of perturbations to the t_{2g} bands[48].

Previous work notes that the Pr-Pr interaction strength is too weak to allow chiral spin liquid correlations on the Pr sublattice at temperatures above 1.5K, despite measurable spontaneous Hall effect signal. The origin of the observed effect was attributed to broken time reversal symmetry at the Ir sublattice[43]. As the most similar point of comparison to $Pr_2Ir_2O_7$ is $Nd_2Ir_2O_7$, which shows AIAO spin ordering at both the Nd and Ir sites in the insulating phase[49], Ohtsuki et al propose AIAO to be the most likely configuration for Ir in $Pr_2Ir_2O_7$[43]. The AIAO ordering and its relationship to the A site elements have been well linked throughout the rare earth pyrochlore iridate series (apart from Pr), with neutron scattering and resonant elastic and inelastic x-ray scattering[43,50–52]. But we did not observe any signal that would indicate long-range AIAO ordering in the Ir sublattice as per the data in Fig 2.6).

As a result of not observing Ir-AIAO ordering, we consider other ways in which Ir moments play a role in the observed TRS breaking. One possible mechanism is that the Ir local moments,

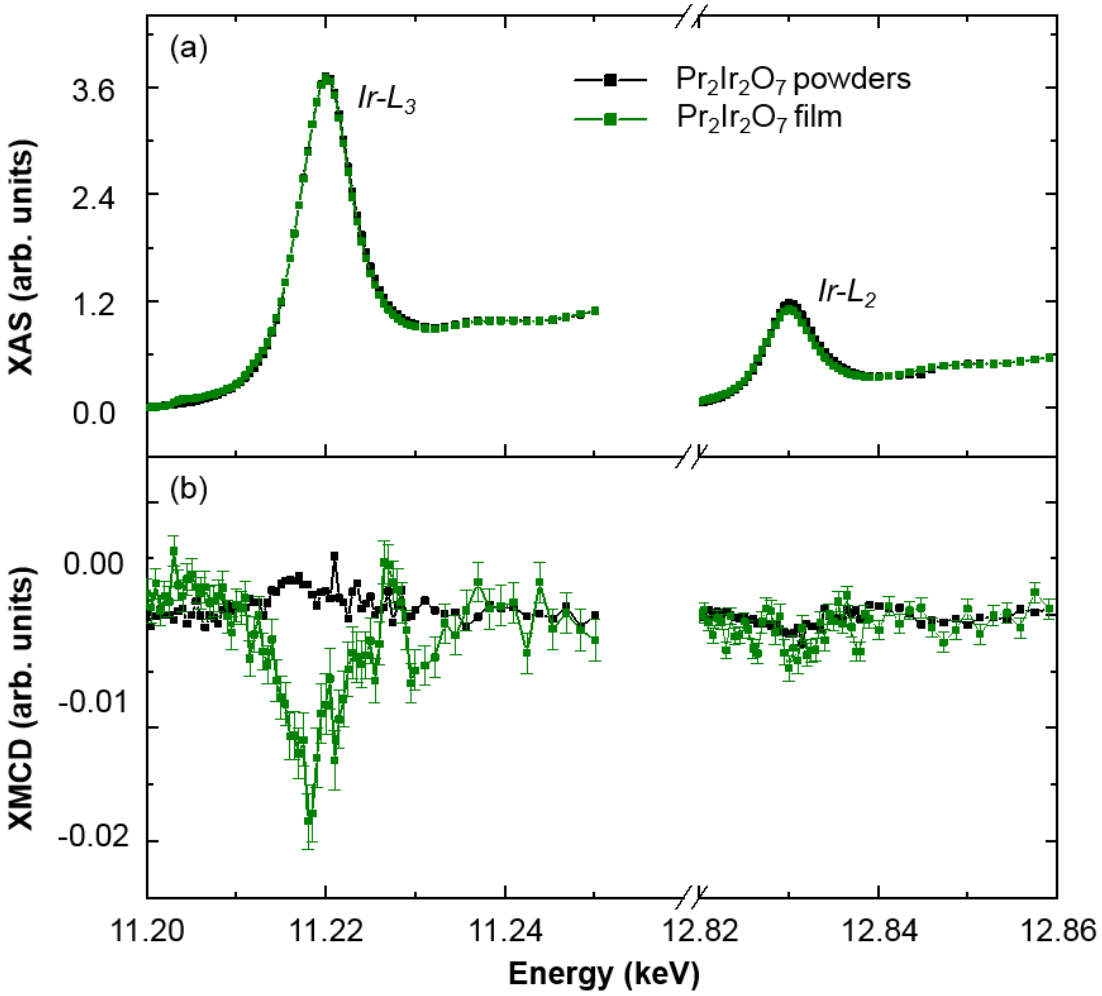

Figure 2.10: The XAS and the XMCD spectra at 2 K under 5 T with magnetic field along the [111] direction at the Ir $L_{2,3}$ edges are compared between the $Pr_2Ir_2O_7$ film (green) and $Pr_2Ir_2O_7$ reference powders (black). The field direction was along the [111] direction of the film sample. For the powder case, the measurement is sensitive to the net Ir moment averaged over the randomly oriented grains.

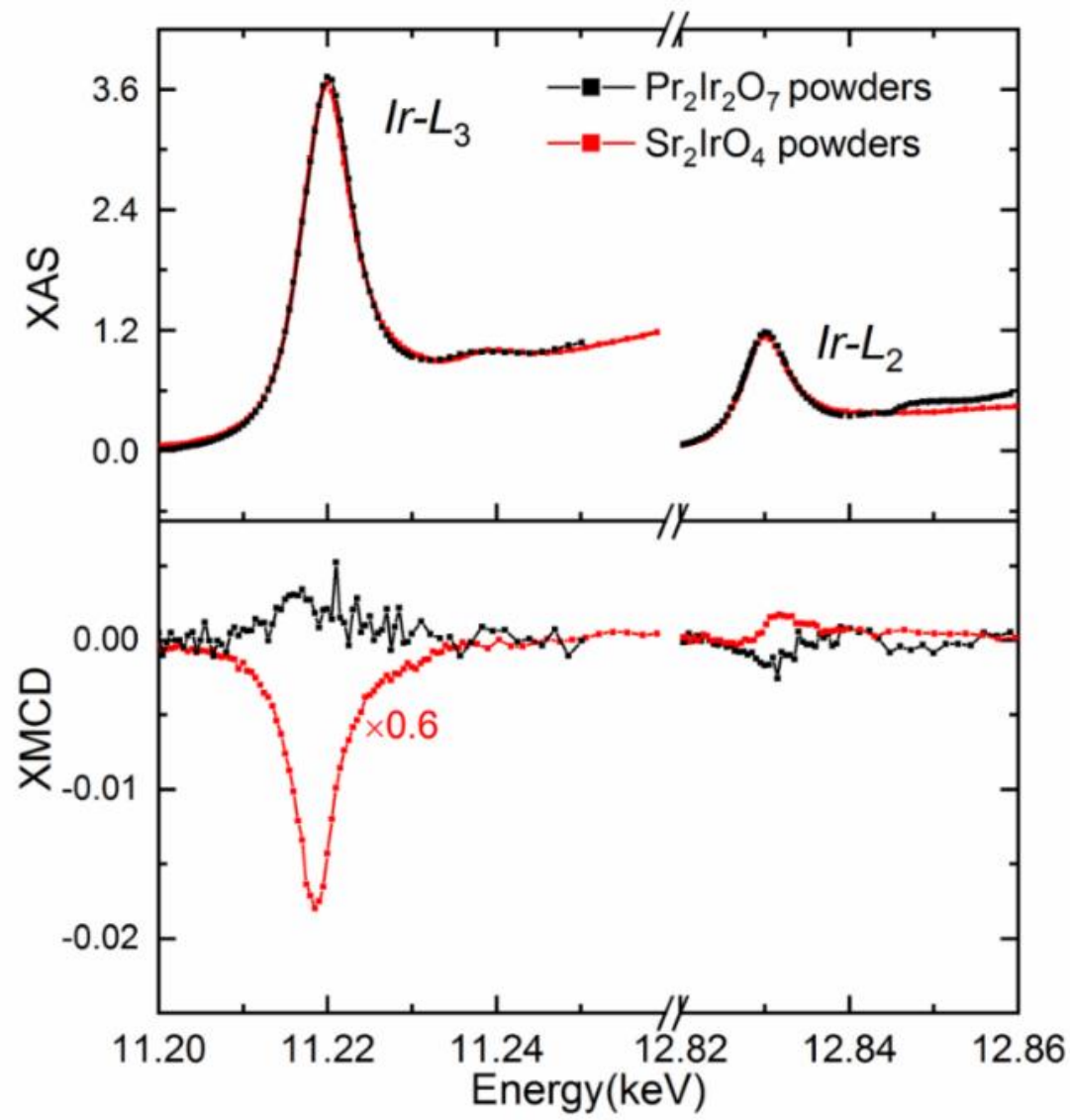

Figure 2.11: The XAS and the XMCD at 2K under 5T at the Ir $L_{2,3}$ edge on $Pr_2Ir_2O_7$ powders. For comparison, XAS and XMCD (the red solid lines which is scaled by multiple 0.6 for direct value comparison) data at the Ir L3 edge on Sr_2IrO_4 powers from Ref[4] are included.

having the same frustrated lattice structure as the Pr, form the same chiral spin liquid correlations, just at higher temperatures. The spontaneous Hall effect in bulk $Pr_2Ir_2O_7$ has been attributed to altering dominant 3-in/out-1-out/in and 2-in-2-out correlations variants at the Pr sites, which leads us to presume these same correlations at the Ir sites can produce the spontaneous Hall effect. This is consistent with the Ir-site spin correlations preceding the Pr-site correlations with cooling, as observed in $RE_2Ir_2O_7$ materials through their metal-insulator transition. In this scenario, the observed small Ir net moment, presumably from canting or defects, couples with the external field, allowing the external field to manipulate the Ir-site spin liquid correlations while not directly producing the anomalous Hall effect[52].

A second possible mechanism is that the Ir local moments renormalize the effective Pr-Pr interaction strength, raising the temperature of the spin-liquid correlation onset of the Pr moments. Since the RKKY interaction describes the Pr-Pr coupling as mediated by the Ir conduction band, consistent with antiferromagnetic coupling and nonzero conductivity, spin polarization at the Ir site should impact this interaction. Subsequently, on the basis of drastically different conduction properties of the Pr and Ir sublattices, one would expect Ir-site spin-liquid correlations to manifest differently in the spontaneous Hall effect than the Pr-site correlations. Yet despite this, the spontaneous Hall effect hysteresis loops appear very similar to the bulk loops attributed to Pr-site correlations[38]. In this scenario, the Ir sublattice would maintain no chiral spin-liquid correlations at all temperatures, and the Ir TRS breaking would only indirectly contribute to the spontaneous Hall effect. The Pr sublattice chiral spin liquid correlations would be the 2-in-2-out and 3-in/out-1-out/in correlations responsible for the spontaneous Hall effect in the bulk[38]. In $Eu_2Ir_2O_7$ films (with no magnetic contribution from Eu^{3+} ions), anomalous Hall effect has been observed, highlighting the contribution of magnetic Ir ions[53]. At this point our experimental evidence does not

rule out either scenario, and future studies on the $RE_2Ir_2O_7$ (without RE local moment) may shed further light on the role of the magnetic Ir sublattice in the Hall effect.

In conclusion, we observed that small lattice distortions in $Pr_2Ir_2O_7$ thin films act as a perturbation, changing the local magnetic properties of the Ir sublattice and inducing a spontaneous Hall effect at elevated temperatures. By analyzing the XMCD signal at the Pr and Ir L edges, we attribute the enhanced spontaneous Hall response in the thin films to localized net moments on the Ir sublattice. Our observations reveal the possible link between structural change in the Ir network, the Ir local magnetic environment, and transport behavior. Understanding these effects provides opportunities to manipulate the $5d$ pyrochlore iridate ground states by modifying the lattices, making this system attractive as a promising candidate in spintronics. Our work opens up possibilities for controlling electronic and magnetic phenomena in conducting frustrated antiferromagnets via thin-film epitaxy.

Chapter 3

Strontium Iridate

3.1 Context and My Contribution

The work on $SrIrO_3$ presented in this chapter is the result of many peoples' contributions and could not have been done successfully without them all. This project had film growth contributions from Trevor Anderson and other useful technical insights and skills from Dr. Tianxiang Nan and Anthony 'Tony' Edgeton in the research group of Chang-Beom Eom, and beamline Xray spectroscopy and sctuctural characterization from Yongseong Choi, Jong-Woo Kim, and Phil Ryan at Argonne National Lab. My own contributions included electrical and magnetic measurements of $SrIrO_3$ thin films, identifying the XMCD technique as valuable and advocating for the measurement of $SrIrO_3$ thin films at Argonne, and consensus building and manuscript writing that resulted in the final publication.

This work was conceived principally by me as an offshoot of my efforts with Trevor Anderson related to his PhD research. Trevor's PhD focused entirely on $SrIrO_3$ thin films, specifically their synthesis and growth, and basic structural properties. My work began with $SrIrO_3$ heterostuctures

first as an attempt to electron dope epitaxial thin-film $SrIrO_3$ with an $LaAlO_3$ overlayer to obtain a heterostucture whose conduction was dominated by a small effective mass electron band, then to investigate ultra-thin (1-2 atomic layers) $SrIrO_3$ overlayers on $SrTiO_3$ as a way to 'add' spin-orbit coupling to the well-studied LAO/STO two-dimensional electron gas. However these samples showed a reduction in electron-type carriers, not and increase as we had expected. This is likely explained by the $LaAlO_3$ layer on the $SrIrO_3$ producing Oxygen vacancies in the $SrIrO_3$ film. This was supported by a conference presentation I saw of unpublished ionic-liquid doping of $SrIrO_3$ results which observed the same reduction in electron-type carriers. Ionic-liquid doping often creates Oxygen vacancies in oxide thin films.

The research presented here arose from my observation of a non-linear Hall effect at 2 K while measuring the control samples for the experiment discussed above. From surveying the literature, I found instances in which this nonlinear Hall effect had been observed, but with smaller magnitude. These publications did not investigate this in detail, at times attributing it to multiple bands effects. $SrIrO_3$ is interesting due to a theoretically-proposed Dirac semimetallic nodal line in the band structure near the Fermi surface. Tensile strain can affect this, and our set of films with various epitaxial strain arising from growth on substrates with different lattice constants seemed to indicate that my obserbved variations in the nonlinear Hall effect could be interpreted as the effect of strain on the Dirac nodal line.

My Hall effect data at 2 K up to 9 T, analyzed in terms of the R_{xy} v $\mu_0 H$ dependence, indicated that the multi-band interpretation was likely incorrect and that, in fact, we had an anomalous Hall effect present. This introduced a host of other potentially-exciting phenomena present in Trevor's films as the related Ruddlesden-Popper phases all showed insulating magnetic behavior (and superconductivity) with $SrIrO_3$ somewhat the anomaly in being nonmagnetic and conducting. At this

point the main question to be answered was the source of the magnetism.

Direct measurement by SQuID magnetometry was inhibited by the dominance of the substrate magnetism at 2 K, even for the sample on $SrTiO_3$ and especially for the Scandate substrates. Furthermore, while the B-site atom, Ir in this case, was the likely culprit, for a new system demonstrating this clearly is always nice. I worked with Dr. Phil Ryan and his team at Argonne National Laboratory to perform low-temperature X-ray magnetic circular dichroism (XMCD) on Trevor's films. This involved me sending films and having video conference meetings and email communication with the team to understand their work. The end result of all of this is put forth in this chapter, presented in a way that emphasizes the ultimate finds more than the process. The subsequent work was drafted entirely by me and has been iterated on many times by both Professor Mark Rzchowski and me.

3.2 Strain Dependent Anomalous Hall Effect in ultra-thin Perovskite $SrIrO_3$ films

Iridates have been extensively researched due to their nontrivial electronic and magnetic properties, such as skyrmions and spin-orbit torques that deviate from predictions based on $3d$ materials due to the large spatial extent and spin-orbit coupling of the Ir $5d$ orbitals[10,54–58]. The large spatial extent of the $5d$ orbitals makes them sensitive to structure, as demonstrated by the strong dimensional dependence of the resistivity in Strontium Iridate Ruddlesden-Popper phases, resulting from the relatively narrow bandwidth and small Coulomb repulsion[54]. Furthermore, in Sr_2IrO_4 the antiferromagnetic insulating state is only induced from the strong spin-orbit interaction in conjunction with electron correlations, making spin-orbit coupling necessary to any understanding of Iridate

magnetism and conduction[59,60].

While the Perovskite phase of $SrIrO_3$ has no magnetic order, other structures and related materials show a diverse set of magnetic properties. Monoclinic $SrIrO_3$ shows evidence of being in close proximity to a ferromagnetic phase, as evidenced by a divergent magnetic susceptibility at low temperatures[61]. Other members of the Ruddlesden-Popper series of Strontium Iridate shows a progression of antiferromagnetic ordering as Ir connections change from planar to three-dimensional[10]. While both $Sr_3Ir_2O_7$ and Sr_2IrO_4 show metal-insulator transitions arising from this antiferromagnetic ordering, bulk polycrystalline perovskite $SrIrO_3$ remains semi-metallic down to the lowest temperatures. Perovskite $BaIrO_3$ has been shown to host a small ferromagnetic moment that diminishes with Sr doping[12].

Another intriguing aspect of perovskite Iridate conduction properties is the proposed Dirac nodal line in the band structure near the Fermi surface[33,62]. As the Perovskite structure of $SrIrO_3$ is only a metastable state, epitaxial thin films are necessary to stabilize the Perovskite structure, but the epitaxy breaks necessary symmetries for the Dirac node, introducing a gap[34]. Angle-resolved photoemission spectroscopy (ARPES) measurements demonstrate the remnants of an electron-like linear dispersion and a broad hole-like band, consistent with a multicarrier interpretation of perovskite $SrIrO_3$ transport[35,55,63]. Additionally, magnetoresistance measurements of polycrystalline samples show indications of the Dirac nodal line accompanied by nonlinear field-induced magnetization at 2 K[64]. Recent experimental and theoretical work indicate that such emergent magnetic properties have a sensitive influence on transport properties such as the Hall effect, and that heterostructuring $SrIrO_3$ with LSMO can change the magnetism, leading to a topological Hall effect[65–67]. Here we report a strain-modulated nonlinear Hall effect, which we attribute to an anomalous Hall effect arising from strain-modulated magnetism. Element-specific X-ray spectroscopy

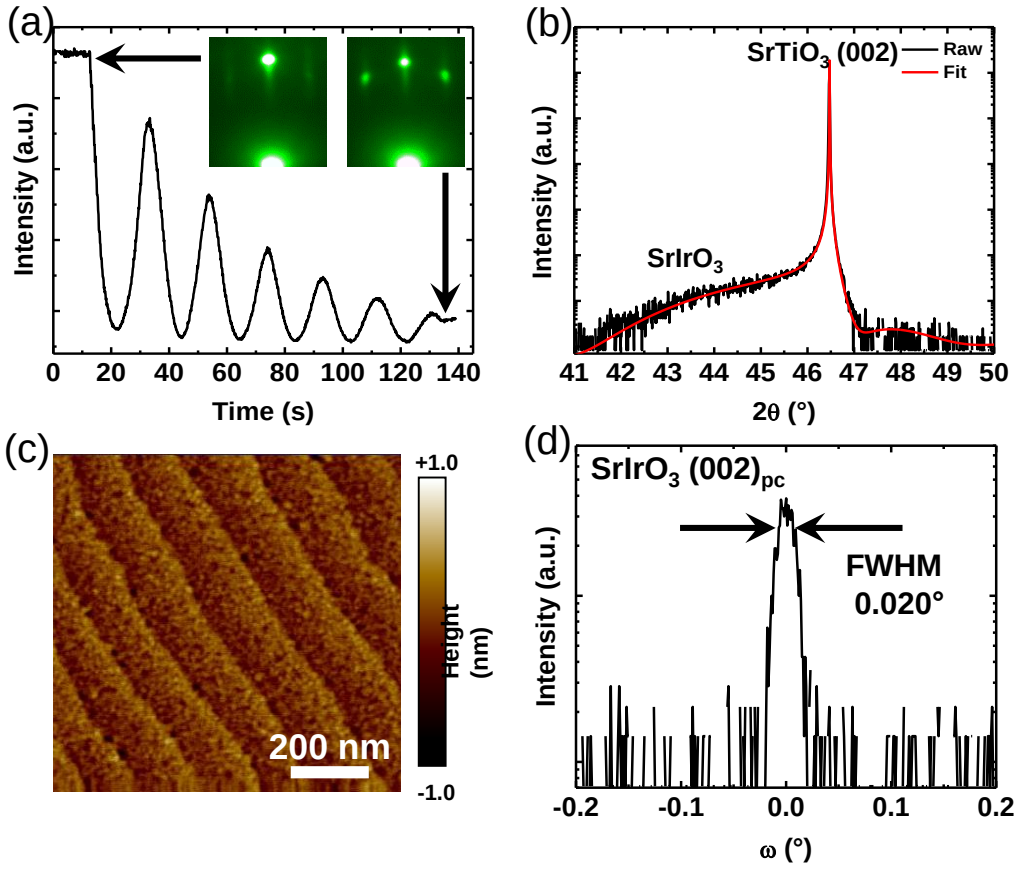

Figure 3.1: Structural characterization of 20 uc $SrIrO_3$ film grown on a $SrTiO_3$ substrate. (a) Film growth was monitored by RHEED to ensure layer-by-layer growth, shown with clear oscillations. (b) Out-of-plane XRD shows a substrate and film peak for the $SrIrO_3$ film on STO. (c) A step-terrace surface is confirmed by atomic-force microscopy. (d) A rocking curve at the (002) peak shows low mosiacity in the $SrIrO_3$ film.

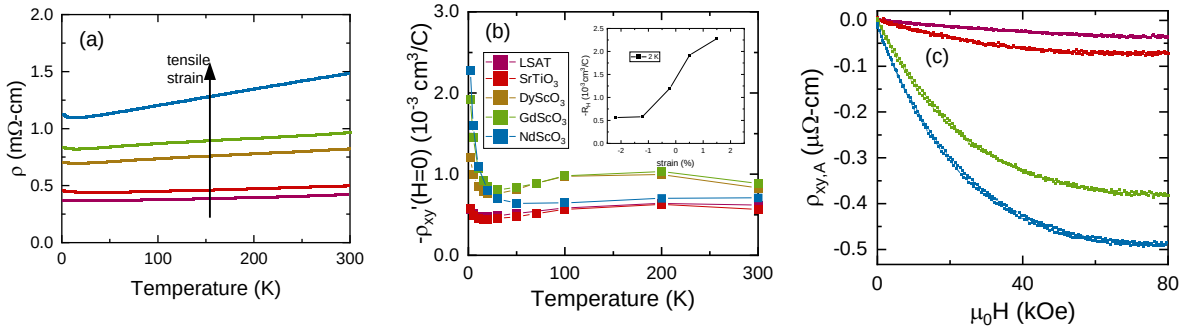

Figure 3.2: Electronic transport overview. (a) Resistivity v temperature data shows metallic behavior for films in all strain states, despite the large increase is resistivity with tensile strain. (b) The Hall coefficient (R_H) fit to data at $|\mu_0 H| < 1.5$ T is constant over most of the temperature range, and increases significantly at the lowest temperatures. (c) High field Hall resistivity v field data at 2 K for four different strain states shows nonlinearity in all films, which increases with tensile strain. (d) Magnetoresistance at 2 K shows a monotonic trend with strain.

directly shows a small field-aligned Ir moment, that supports some but not all of the Hall data interpretation.

We synthesized our pseudomorphic films using pulsed laser deposition with in situ reflection high-energy electron diffraction (RHEED). Films were grown on five different substrates producing between 2% compressive and 1% tensile strain, all with cubic or pseudocubic (001) orientations. Layer by layer growth and 20 uc thickness was confirmed by RHEED oscillations, and coherently strained films were confirmed with reciprocal space maps around the $(\bar{1}03)$ substrate peak, as shown in Fig 3.7. Good step terrace features were maintained through the films, as confirmed by atomic-force microscopy. Van der Pauw electronic transport measurements were carried out in a Quantum Design PPMS at temperatures from 2 K to 300 K, with applied magnetic fields up to 9 T. Spectroscopic X-ray measurements were carried out at Argonne National Lab Advanced Photon Source.

All films showed semimetal-like resistivity between 30 K and 300 K (Fig 3.2a), with 300 K re-

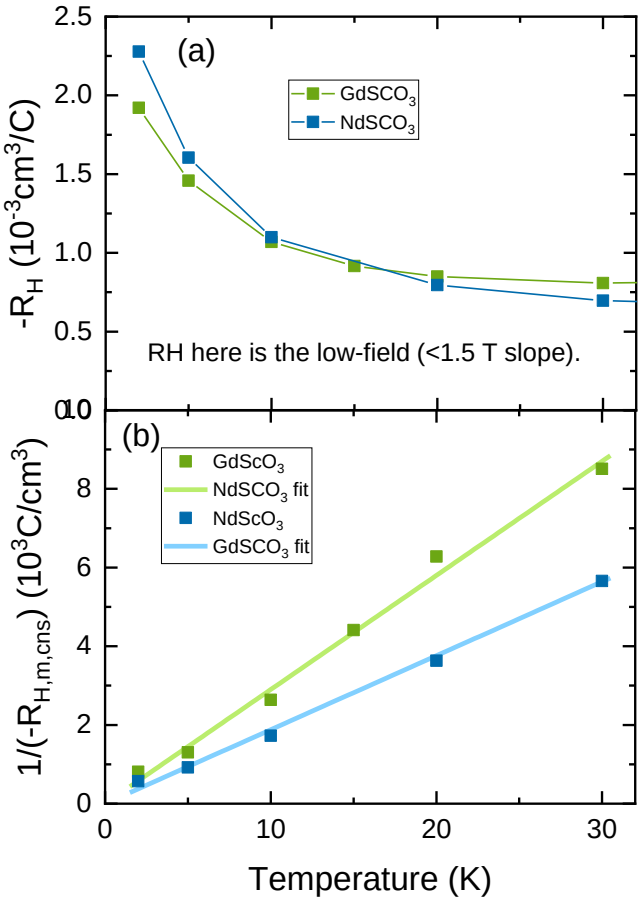

Figure 3.3: Hall resistance modelling from magnetic origin. Hall resistivity v magnetic field for SIO films on GSO (a) and NSO (b). The dashed lines show the results of fitting the MFT model in eqn 1 simultaneously to all the temperatures shown. (c) The low-field Hall slope (R_H) at field below 1.5 T decreases in magnitude as the temperature increases. (d) Subtracting the high-temperature R_H value reveals an inverse relationship with temperature, just as we expect for paramagnetic susceptibility.

sistivity between 0.4 and 1.5 mΩ-cm, consistent with previous reports of epitaxial films on $SrTiO_3$ substrates[56,68]. The 300 K resistivity of films increases significantly with increasing tensile strain across the substrate series. Several observations lead us to conclude that this is an intrinsic behavior rather than arising from increasing misfit defects. First, room-temperature X-ray diffraction results show that the $SrIrO_3$ unit cell volume expands in response to the tensile strain in a way that is consistent with a Poisson's ratio of 0.35, a typical value for ceramics[69]. Second, increasing room temperature resistivity is accompanied by a larger residual resistivity ratio, defined as $\rho(300\text{ K})/\rho(2\text{ K})$, as shown in Fig 3.8. Because scattering from defects is relatively temperature independent, increasing defect density would increase the resistivity without also increasing the residual resistivity ratio[70]. Finally, the most common defect in oxide films is oxygen defects, which modulate the n-type carriers. Hall measurements of our films do not show significant modulation of room-temperature carrier density, again suggesting defects are not the dominant cause of the increased resistivity.

Low-temperature Hall measurements showed n-type conduction to 2 K, indicating that electrons dominate conductivity, consistent with other reports[55,71]. Figure 3.2(c) shows that the low-temperature transverse resistivity ρ_{xy} is linear at high magnetic fields and nonlinear at lower fields, with larger tensile-strain samples showing more nonlinearity, similar to other reports[72]. Accordingly, the nonlinearity is largest in the SIO/NSO film, and smallest in the SIO/LSAT film. Since the nonlinearity adds to the zero-field slope, and thus contributes to the low-field R_H value, the trend in R_H at 2 K shows the strain dependence of the nonlinearity in which increasing tensile strain increases R_H, as inthe inset to Fig 3.2(b). We note that the data shown in Fig 3.2(c) cannot be linked to multicarrier effects since the curvature abates as the field increases without showing a local minimum, as would be expected for a fast-electron, slow-hole model[73]. We model the

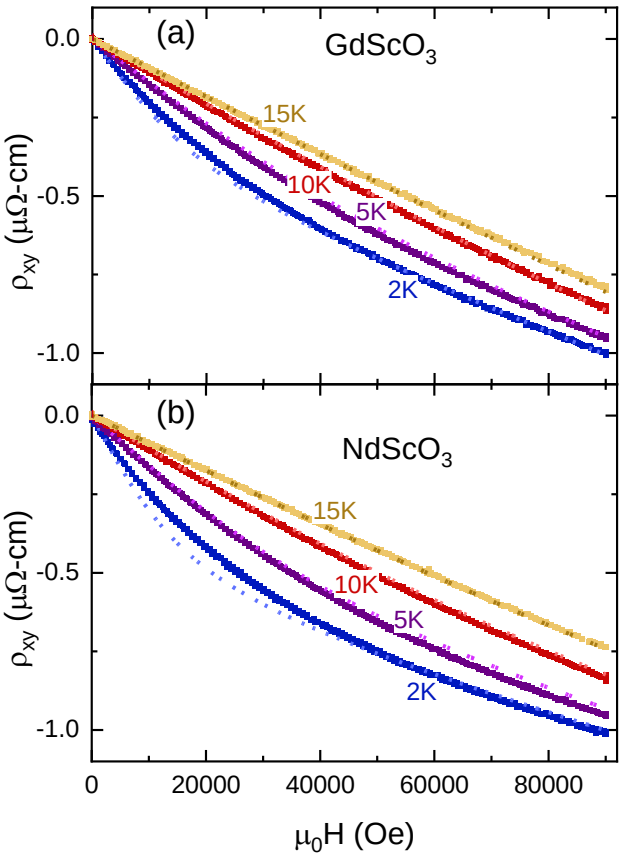

Figure 3.4: Hall resistance modelling from magnetic origin. Hall resistivity v magnetic field for SIO films on GSO (a) and NSO (b). The dashed lines show the results of fitting the magnetization model simultaneously to all the temperatures shown.

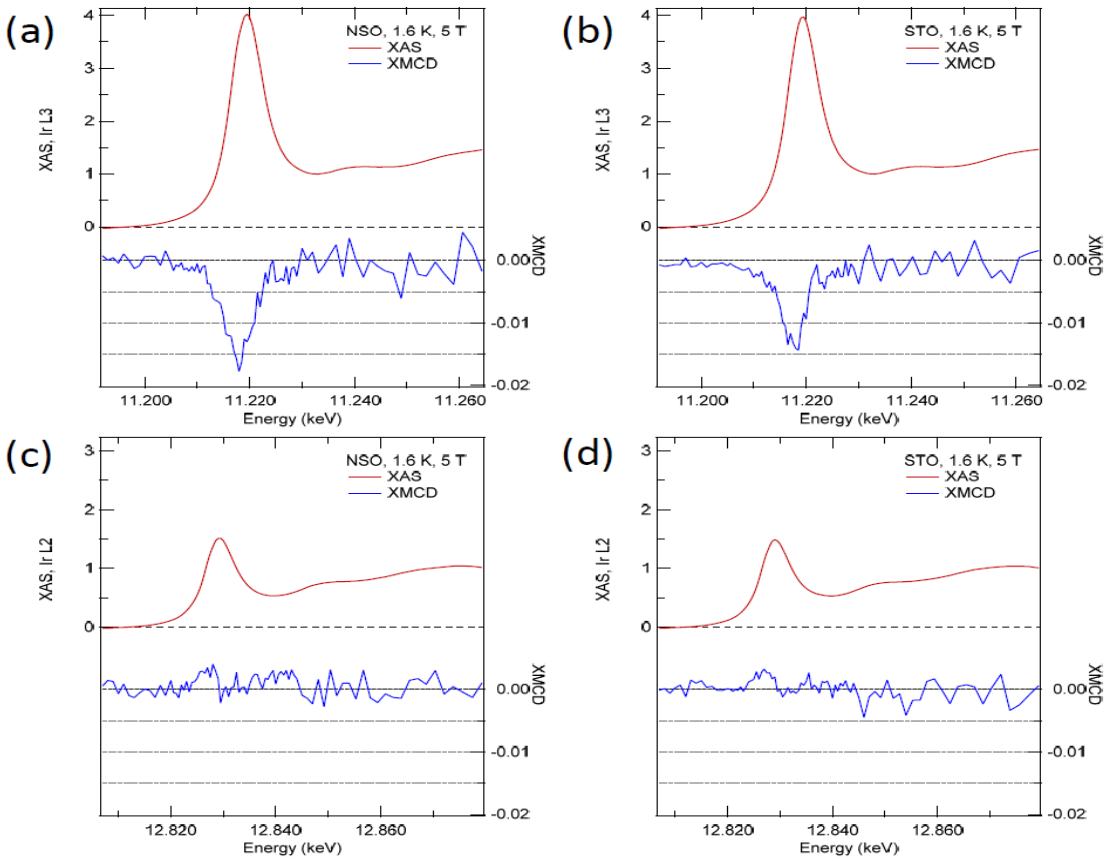

Figure 3.5: XMCD results for $SrIrO_3$ films on NSO and STO. Total absorpbtion (red) and XMCD (blue) signals are shown for the L3 energy in (a) for NSO and (b) for STO, while L2 energy is in (c) for NSO and (d) for STO. There is no discernable L_2 signal for either film, indicating the Ir electronic structure mimics that of Sr_2IrO_4.

transverse resistivity as an anomalous Hall effect due to magnetic-field induced magnetization using the standard expression $\rho_{xy} = R_M M(B) + R_O B$, where R_M and R_O are the anomalous and ordinary Hall coefficients, and M is the film's magnetization[64]. High-field behavior is captured by the $R_O B$ term, and $\rho_{xy} - R_O B$ is the nonlinear contribution, shown in Fig 3.2(c). Our fits of the Hall data yielded 2 K values of R_O of 0.51 and 0.6310^{-3}cm^3/C for $SrIrO_3$ on NSO and GSO respectively, close to the room-temperature values of R_H, indicating that the $SrIrO_3$ band structure does not change when the nonlinearity occurs. As a result, we separate the transverse resistivity into two contributions. The first is the temperature-invariant band contribution $(R_O B)$ linear in magnetic field, and the second the temperature-dependent nonlinearity $(R_M M)$ attributed to a magnetic origin.

We leverage this observation to look for a Curie-law temperature dependence in the low-temperature Hall data in $SrIrO_3$ films on NSO and GSO, which show the largest nonlinearities. We separate the transverse resistivity into two parts: a linear-in-field ordinary Hall effect, and a nonlinear-in-field contribution that we attribute to a field-induced magnetization. In this case we start with the R_H values measured at fields below 1.5 T, and look for the existence of a constant value $R_{\rm cns}$, linear-in-field contribution, to subtract such that a Curie-law temperature dependence is revealed. The constant value represents the ordinary Hall effect contribution from the R_H data and was found to be 0.52 and 0.69 10^{-3}cm^3/C for SIO on NSO and GSO respectively. The resulting values are referred to as $R_{H,\rm cns}$. The negative of the measured Hall coefficient is shown in Fig. 3.3(a) as a function of temperature, and the reciprocal of $R_{H,\rm cns}$ is shown in Figure 3.3(b).

In the magnetic picture, low-field magnetic behavior is characterized by the magnetic susceptibility, χ, defined through $M = \chi B/\mu_0$. In this interpretation, we have extracted the Hall analog to the magnetic susceptibility,

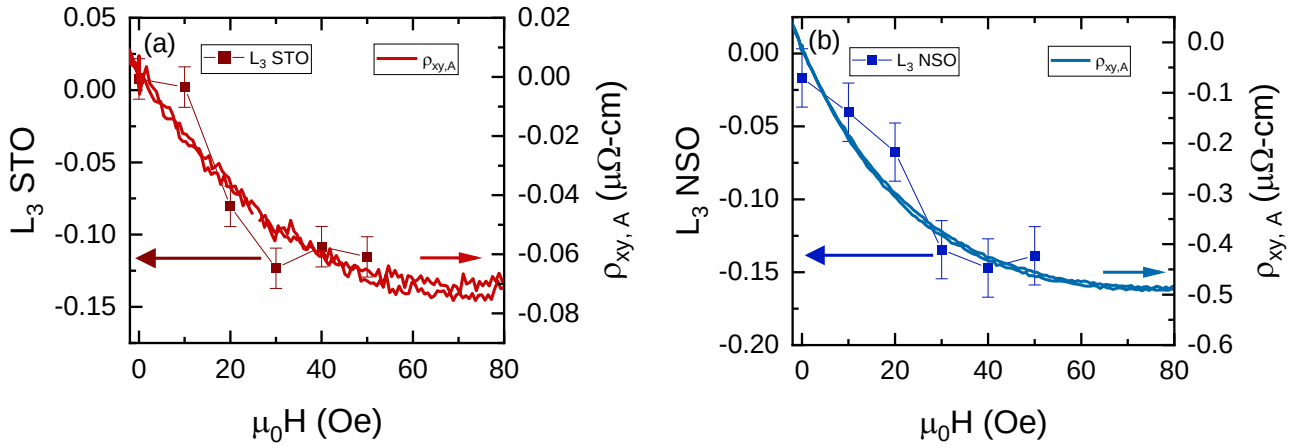

Figure 3.6: XMCD results compared with Hall measurements. Area under the L3 XMCD peak normalized to XAS at 1.6 K overlaid with the anomalous Hall data for SIO on (a) STO and (b) NSO substrates. The SIO film on NSO shows only slightly increased Ir local moment magnitude compared to STO, despite a much larger $\rho_{xy,A}$.

$$R_{H,cns} = (d\rho_{xy})/(d\mu_0 H) - R_{cns} = R_M \chi/\mu_0, \tag{3.1}$$

because the value is the susceptibility multiplied by R_M. In figure 3.3(b), the Curie law is linearized as $\mu_0/(R_M\chi) = T/C$. Results from fits discussed later show that the ratio of the R_M values of the two films does not fully account for the different slopes in Fig. 3.3(b), indicating that the Curie constant, C, must be larger in the film on NSO than in the film on GSO, consistent with larger local Ir moments in the film on NSO.

To investigate the temperature-dependent nonlinearity with magnetic field, we choose a simple paramagnetic model consistent with the temperature scaling to describe the field-induced magnetic response in the $SrIrO_3$ films. Specifically, we choose a Langevin model with no interactions, as this describes a paramagnetic system with neither hysteresis nor any spontaneous long-range ordering. We model the magnetization, M, with a Langevin response,

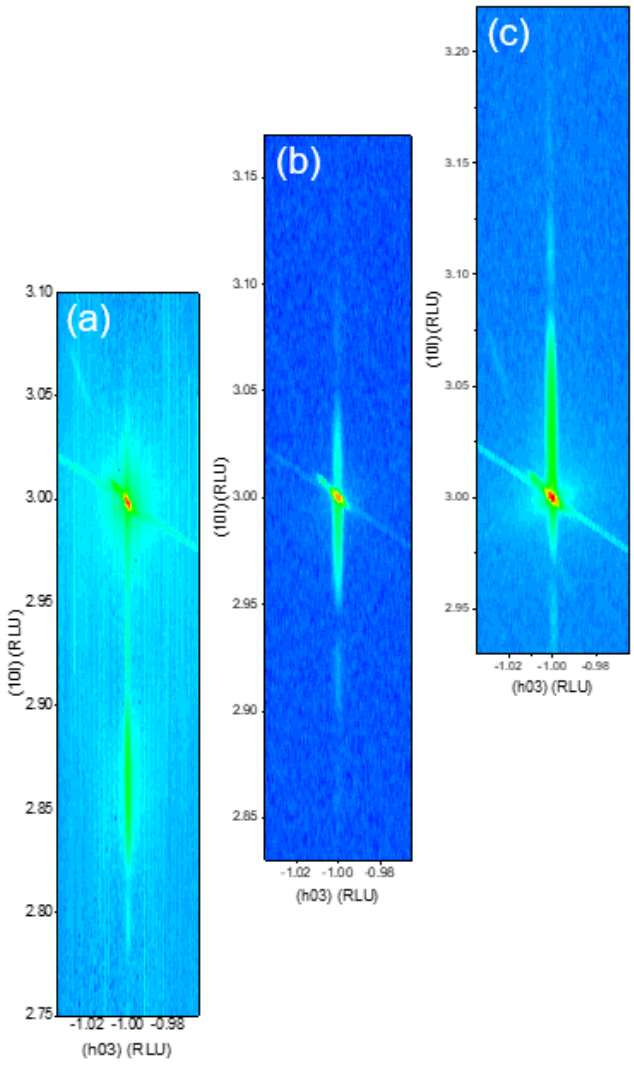

Figure 3.7: Reciprocal space maps of SIO films. SIO films on (a) LSAT, (b) DSO, and (c) NSO substrates all show coherent growth, as indicated by the film and substrate peak alignment at the same h value of -1.0. The reciprocal lattice units (RLU) for each scan are computed from the substrate's pseudocubic lattice constants.

$$M/M_S = L(x) = coth(x) - 1/x, x = (\mu_{eff}B)/(k_BT). \quad (3.2)$$

In eqn 3.2, μ_{eff} is effective local net magnetic moment on the Ir atoms in Bohr magnetons, k_BT is the thermal energy, L is the Langevin function, and M_S the saturation magnetization, related to μ_{eff} through the Ir density. The magnetization versus B thus has an inherent temperature dependence through x. We applied this model to the low-temperature Hall data in two ways. First, we simultaneously fit field sweeps at 2, 5, 10, and 15 K, forcing μ_{eff} to be constant at all temperatures, the results of which are shown in Fig. 3.4. This provided a good description of the data at 10 and 15 K, but failed at 2 and 5 K due to the constraint on μ_{eff}. These results reveal that μ_{eff} increases in value with increasing tensile strain. Furthermore, removing the dependence on R_M from the Curie constants determined from the low-field temperature dependence, we also find a larger net moment in the higher-strained film on NSO than on GSO. Alternatively, we fit temperature independently, allowing for different values of μ_{eff}, and these results are shown for $SrIrO_3$ on NSO in Fig. 3.10. These results show clearly that μ_{eff} is not constant with temperature. We ascribe the decreasing value of the μ_{eff} parameter to the slight decrease in R_O with temperature over this temperature range that our fit is insensitive to due to the limited maximum measurable field.

To discern whether the magnetism we observe in the Hall data comes from the Ir site and to gain more information about the Ir electronic state, we performed Xray magnetic circular dichroism (XMCD) measurements for the L_2 and L_3 edges at 2 K and up to 5 T. XMCD at the Ir $L_{2,3}$ edges enables probing the Ir $5d$ states, and in particular, the half-filled $J_{\text{eff}} = 1/2$ and full $J_{eff} = 3/2$ state can lead to different transition probabilities for the Ir L_3 and L_2 XMCD signals. Figure 3.5

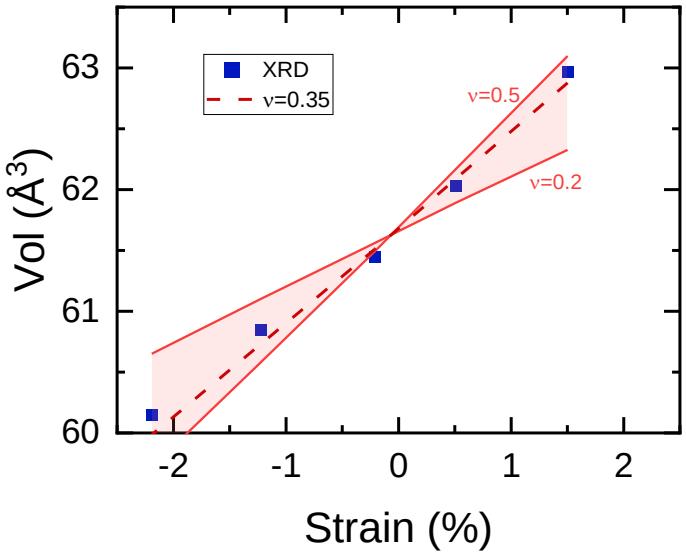

Figure 3.8: The unit cell volume of the SrIrO3 films increases with tensile strain. We rule out structural defects as the cause of this by showing that the volume increase is consistent with a Poisson's ratio of 0.35, a reasonable value for $SrIrO_3$.

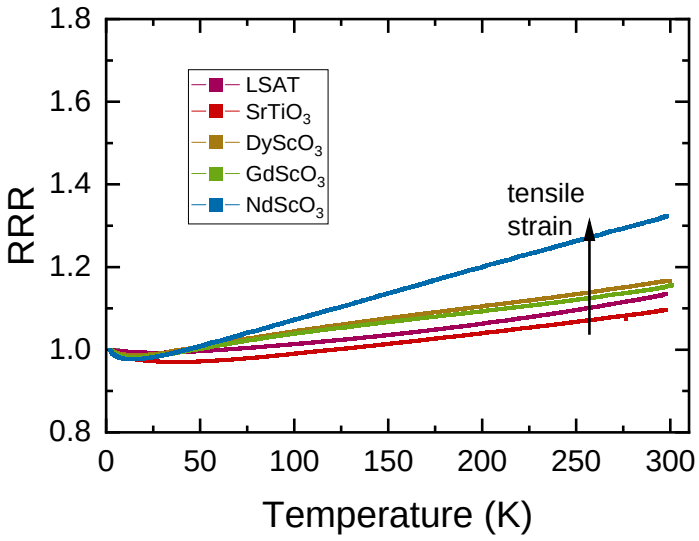

Figure 3.9: Residual resistivity ratios for the films, normalized to their 2 K values. Increasing tensile strain has a larger ratio, again suggesting that defects are not the predominant cause of the increased resistivity in tensile-strained films.

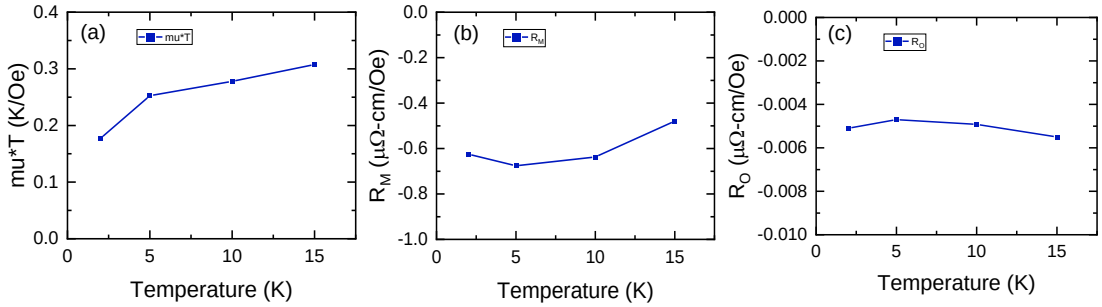

Figure 3.10: Fits of SIO on NSO versus temperature. (a) The magnetic moment strength increases with temperature. We expect it to be constant. (b) R_M is approximately constant across all temperature we observed nonlinear Hall effect. (c) RO is also constant across temperatures. SIO on NSO was chosen as the representative film for this fitting because it shows the strongest nonlinearity, making the higher temperature fits more reliable.

shows no discernable L_2 edge absorption intensity for the $SrIrO_3$ on STO or NSO substrates and an L_3 edge XMCD intensity with a small strain state dependence[74]. To understand this, we compare our $SrIrO_3$ results to measurements on $Sr2IrO_4$ thin films[3]. The near-zero Ir L_2 XMCD observed in Sr_2IrO_4 indicates the same half-filled $J_{\text{eff}} = 1/2$ and full $J_{\text{eff}} = 3/2$ state in our $SrIrO_3$ films as in Sr_2IrO_4[3]. Figure 3.5 shows XMCD spectra from the $SrIrO_3$/$NdScO_3$ (NSO) and $SrIrO_3$/$SrTiO_3$ (STO) samples. The strong Ir L_3 peak (whiteline) intensity in x-ray absorption spectroscopy (XAS) relative to the L_2 counterpart indicates a strong spin orbit coupling[12,74]. The significant L_3 and insignificant L_2 XMCD intensities matches the observations in Sr_2IrO_4, revealing insignificant mixing of the two J_{eff} states, as seen in other ultrathin $SrIrO_3$ films[56]. The mixture of the two states, thus deviations from the half-filled $J_{\text{eff}} = 1/2$ state, can give rise to non-negligible L_2 XMCD intensity, as seen in the Sn-doped $SrIrO_3$ and $SrIrO_3$ sandwiched by $La_{2/3}Sr_{1/3}MnO_3$[42,75].

This indicates a $SrIrO_3$ electronic state more similar to Sr_2IrO_4 films than $SrIrO_3$ heterostructed with magnetic materials, where clear Ir-site local moments were observed[42]. We now compare the Ir moments in different strain states via the L_3 XMCD. The $SrIrO_3$ film on NSO at 1.6 K and 5 T

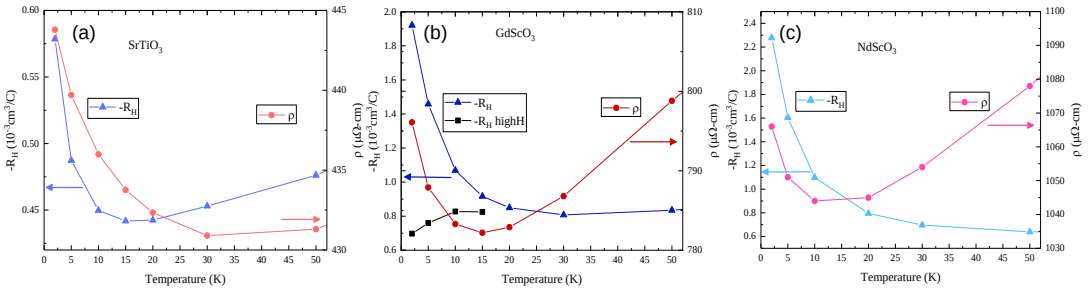

Figure 3.11: The low temperature increase in the Hall coefficient is not concomitant with the upturn in resistivity. (a-c) The temperature values for minimum Hall coefficient and resistivity show opposite temperature dependences with strain, indicating separate origins for the two phenomena.

shows an L_3 XMCD peak about 20% greater than the $SrIrO_3$ film on STO, signifying an increased local moment in the film on NSO, as show in figures 3.5(a,b) and 3.6. In the Sr_2IrO_4 case, the Ir L_3 XMCD effect is about 3% of the whiteline intensity, which corresponds to a local magnetic moment of 0.045 μ_B/Ir[3]. In comparison, the Ir L_3 XMCD signal in our $SrIrO_3$ films is about half that observed in Sr_2IrO_4, and we estimate a local moment of about 0.02 μ_B/Ir in our films. This value is significantly higher than the bulk value of 0.004 μ_B/Ir, but still far smaller than the Hall-derived value of 0.25 μ_B/Ir[56,64]. The film form of the $SrIrO_3$ increases the localization tendency and increases the local moment relative to the bulk case. However, the substrate strain effect is sufficiently strong enough to be the main tuning parameter for the resistivity.

Comparing the XMCD field dependence with the nonlinear Hall data in Fig. 3.6 reveals another notable feature. Both show an apparent saturation above 3 T, while our Hall-derived μ_{eff} values predict a 10 T saturation, and our XMCD values predict 100 T. This discrepancy can be reconciled by a weak interaction of Ir local moments or the existence of an itinerant net magnetic moment. Furthermore, the L_3 XMCD signal shows about a 20% larger signal in the film on NSO than in the film on STO. This is smaller than the 60% increase observed between the two films via the anomalous Hall conductivity, shown in Fig. 3.12. Thus, the Xray study confirmed that the Ir

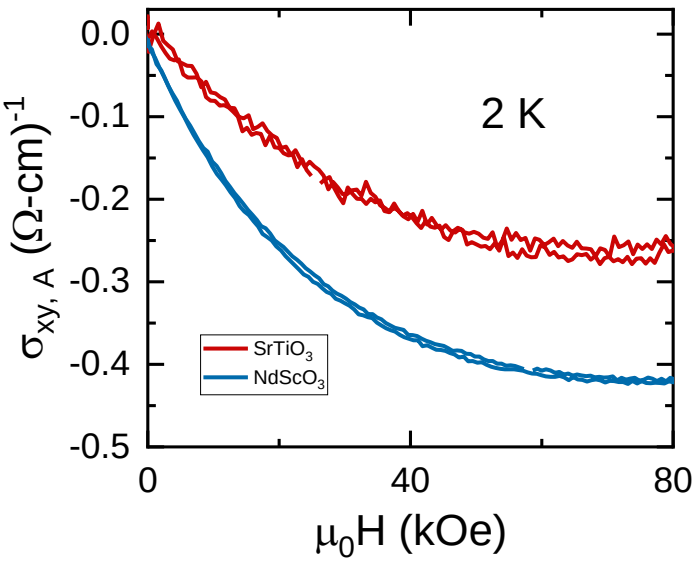

Figure 3.12: The anomalous Hall conductivity at 2 K for $SrIrO_3$ films grown on STO and NSO substrates. Computing the conductivity from the resistivity removes the influence of the resistivity from anomalous Hall effect, yielding a quantity that is proportional to net magnetization.

atomic moment is significantly higher in films than in bulk but did not fully explain the strain dependence of the anomalous Hall data.

To attempt to reconcile the large anomalous Hall effect and strain dependence with the small moments observed by XMCD, we compare the magnitude of our anomalous Hall effect to that of similar Ir-conduction systems. The magnitude of the anomalous Hall effect in our films is quantified by $\Delta\rho_{xy}$, calculated as half the difference of the y-intercepts of linear fits to the positive and negative high-magnetic field Hall data. The conductivity analog to this is$\Delta\sigma_{xy}$. In $SrIrO_3$/LSMO heterostructures the proximity to the LSMO magnetism induces an AFM state in the $SrIrO_3$ with a canted net moment aligned opposite to the LSMO net moment[66]. In our case, we are likely realizing the net moment, but it is field aligned, producing a negative AHE. Using $\Delta\sigma_{xy}$ at 2 K as a measure of the saturation value of the Hall nonlinearity, our values of between 0.2 and 0.6 $(\Omega\text{-cm})^{-1}$, as shown in Fig. 3.13, with XMCD-calculated moments estimated to be about 0.02 μ_B/Ir

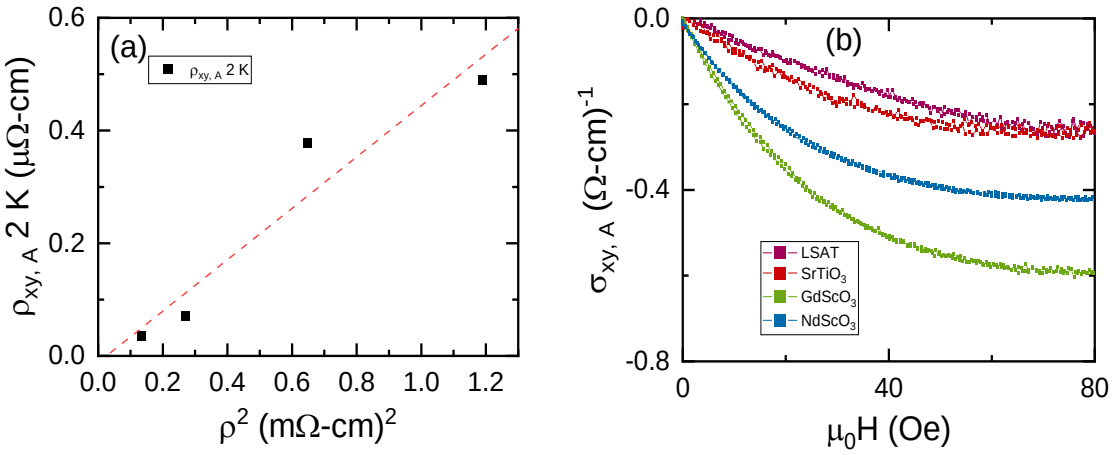

Figure 3.13: Anomalous Hall resistivity. (a) The scaling relationship between the anomalous Hall amplitude and resistivity squared. A linear relationship indicates a constant anomalous conductivity. (b) Anomalous Hall conductivity versus field for SIO on different substrates at 2 K, showing that a constant anomalous Hall conductivity does not occur with strain.

are similar, but slightly smaller than the LSMO heterostructures, that show about 1 $(\Omega\text{-cm})^{-1}$ with a local Ir moment of $0.021\mu_B$/Ir determined from XMCD[66]. The $4d$ material $SrRuO_3$ has shown AHE of about 100 $(\Omega\text{-cm})^{-1}$ per 1 μ_B/Ru at 2 K, which is larger than our 10 $(\Omega\text{-cm})^{-1}$ per 1 μ_B/Ir result[76]. Both of these comparisons show our anomalous Hall values are at the lower end of what is typically observed, so our larger values for $SrIrO_3$ on NSO are not the result of an atypically large effect. Furthermore, the scaling of the Anomalous Hall effect ($\Delta\rho_{xy}$) across the range of strain states is approximately linear with ρ_{xx}^2, as shown in figure 3.9, indicating the AHE is independent of the scattering rate. The exact details of the strain scaling discrepancy between our anomalous Hall and XMCD data are beyond the scope of this work, but we mention these ideas to support that our observed Hall nonlinearity comes from a magnetic origin.

In summary, we have observed clear low-temperature anomalous Hall effect in perovskite $SrIrO_3$ thin films grown on different substrates with different strain states. We have successfully mapped this phenomenon to a magnetic origin that is consistent with element-specific spectroscopy

at the Ir site. While the transport data show a strong strain dependence in the AHE, our XMCD results only partly explain the variation in the Hall data.

Chapter 4

Mn Superlattices

4.1 Context and My Contribution

The work in this chapter is the result of many people working together and could not exist without each persons' individual contribution. This project had film growth contributions from Tianxing Nan and Lu Guo in the research group of Chang-Beom Eom, interpretation and collaboration contributions from visiting Prof. Thomas Tybell, polarized neutron reflectivity measurements from Alex Grutter and others at NIST. My own contributions included electrical and magnetic measurements of bilayer and superlattice samples, a re-interpreration based on these measurements of the magnetization changes between samples, and consensus-building and manuscript modification that resulted in the final publication.

This project arose from the work of Dr. Tianxiang Nan in the Eom research group on spin torque in Mn_3GaN films, in which he found an out-of-plane component to spin torque[77]. This contrasted with most spin-current generating materials, where resulting spin-torques are only in the film plane. Spin-torque studies are often made in heterostructures consisting of a spintorque

generating material, in this case Mn_3GaN, interfaced with a ferromagnet, often permalloy (Py). Permalloy has many advantages for spin-torque measurements, but its in-plane magnetization limits studies of these interesting out-of-plane effects. The ferromagnet Mn_3Ga has such out of plane magnetization that would allow exploration of these new symmetries, but it had not been grown in single crystal thin-film form; however, this hurdle was quickly and conveniently cleared by growing it directly on Mn_3GaN thin films. An additional Mn_3Ga challenge was its large coericivity that complicated its magnetization manipulation, a challenge addressed by manipulating the coercivity via further heterostructuring with Mn_3GaN.

My contribution began with the electrical and magnetic exploration of these Mn_3GaN/Mn_3Ga films. I found clear differences in the magnetic properties of different Mn_3GaN/Mn_3Ga superlattices, with both the coercivity and net magnetization (per Mn_3Ga layer) seeming to change with different superlatticing parameters. This increased net magnetization per Mn_3Ga layer proved exciting enough to spur theories about interfacial magnetism occurring at the Mn_3Ga/Mn_3GaN interfaces, as Mn_3GaN is a known antiferromagnet with no net moment, while Mn_3Ga has a net moment around $2-3\ \mu_B$/Mn.

However Mn_3Ga is actually ferrimagnetic, meaning that its magnetic lattice has spins of opposing directions that do not completely cancel, making the magnitude of its net moment very sensitive to Mn deficiency[78].

My careful analysis of the superlattice data found a net magnetization per Mn_3Ga layer that was monotonic with sample growth number, but not any apparent property of the interfaces or superlatticing. However, the coercivity could be controlled with superlatticing properties. Professor Thomas Tybell, visiting for one year, reached out to contacts at NIST's neutron beamline to perform polarized-neutron reflectometry (pnr) on the superlattices to profile the interfacial net

magnetic moment. At this point graduate student, Lu Guo began growing antiperovskite films for the project. Dr. Alexander Grutter at NIST performed the Polarized Neutron Reflectivity (PNR) measurements and data analysis. These results showed an enhanced in-plane magnetic moment at the interface of Mn_3Ga/Mn_3GaN. Because of the in-plane geometry constraints of the PNR experiment, we were unable to conclude an actual enhancement to the total magnetic moment. In order to quantify the interfacial enhancement, we needed a "control" Mn3Ga bilayer sample.

We found nearly identical saturated net magnetic moments between the bilayer and superlattice films, and my data persuasively showed that stoichiometric drift was the predominant factor changing the net magnetic moment of the films and superlattices and not an interfacial effect. This required a new interpretation of the results. As many of my co-workers had moved on from this project, I led the work to integrate into the manuscript a new interpretation of changing stoichiometry at the interface and the magnetic anisotropy. This involved my communication via email and videoconferencing with co-workers to develop a universally accepted interpretation. The resulting work was recently accepted for publication in October 2023 in the form presented here.

4.2 Tuning the magnetic anisotropy in layered Mn_3GaN/Mn_3Ga superlattices

Spin-torque devices rely on spin current generation in one material injected to another to manipulate the magnetization. As spin current can decay on short length scales, bilayer geometries optimize the functionality of such devices, with spacer layers shown to increase the interface transparency[79], increasing spin accumulation in the magnetic layer. In general, this accumulation can be optimized by increasing the interface area and by increasing the interface transparency. The

first can be accomplished by increasing the interface number via artificially layered superlatticing, while the second can be accomplished with coherent epitaxial heterostructures, for instance between the $D022$ ferrimagnet Mn_3Ga and the cubic antiperovskite Mn_3GaN[80].

Tetragonal $D022$ Mn_3Ga (MG) is a promising spintronics material due to its low saturation magnetization, high spin polarization, and strong perpendicular magnetic anisotropy[78,81–85]. In this X_2YZ form of Heusler materials, Mn occupies both the X and Y sites while they retain their distinct crystallographic symmetries. These different Mn sites (Mn1 and Mn2) are antiferromagnetically aligned with different magnetic moments, resulting in a ferrimagnetic metal with out-of-plane magnetic anisotropy estimated to be in the range 0.1 MJ/m^3 - 1.0 MJ/m^3[78,83]. MG has metallic conductivity, with room temperature resistivity 100 $\mu\Omega$-cm. To incorporate MG in spintronic devices, heterostructuring with other materials is necessary. Attempts at heterostructuring with Cr and Mo did not produce films with appropriate magnetic properties, likely due to strain[86,87]. We demonstrate that thin-film Mn_3GaN is an ideal heterostructing layer for intrinsic MG thin films.

Cubic antiperovskite Mn_3GaN (MGN) is a promising spintronic material due to its noncollinear antiferromagnetism, close phase-proximity to the topological Hall effect, and ability to generate unconventional spin-current polarizations and spin-orbit-torques[27,36,37,77,88–90]. At room temperature, thin-film MGN is antiferromagnetic with the Γ^{5g} magnetic structure[77]. This magnetic structure has been shown to produce spin currents that exert torque on out-of-plane magnetizations, such as those stabilized in MG. Strong covalent bonding and several bands at the Fermi surface lead to metallic conductivity in MGN, with room temperature resistivity 200 $\mu\Omega$-cm[27,91].

As MG and MGN share the same cations and cation ratio, only the body-center nitrogen differentiates the materials. As shown in Figs. 4.1(a) and (b), the basal planes of both unit cells have

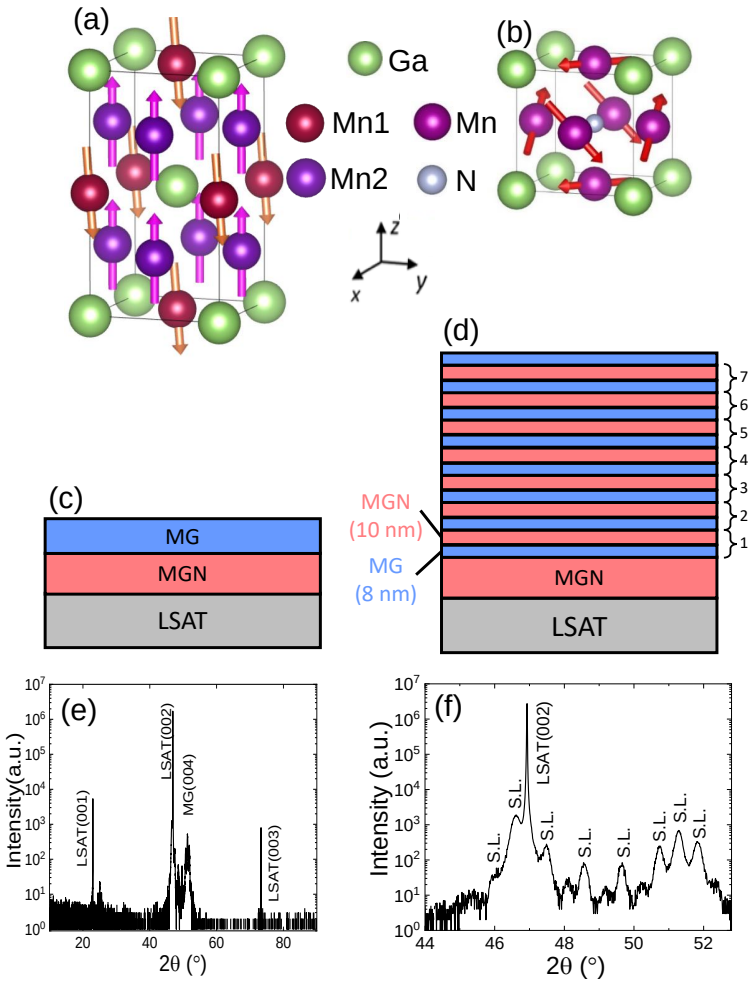

Figure 4.1: The unit cells of (a) Mn_3Ga (MG) and (b) Mn_3GaN (MGN). The arrows in the figure indicate the spin directions held by corresponding Mn atoms. MG has two distinct Mn sites with different symmetries and different magnetic moment directions, Mn1 (ruby) is the minority site, and Mn2 (purple) is the majority site. MG was stabilized in (c) bilayer structures in which a thick MGN layer provided a template for the MGN, and (d) superlattice structure, Sample A, in which MGN was also used as a base layer and MG as a capping layer. The (e) Xray-ray $\theta - 2\theta$ scan shows only substrate and films peaks, while (f) highlighted region around LSAT(002) peak of the Mn_3Ga/Mn_3GaN (MG/MGN) superlattice sample shows annotated superlattice reflections.

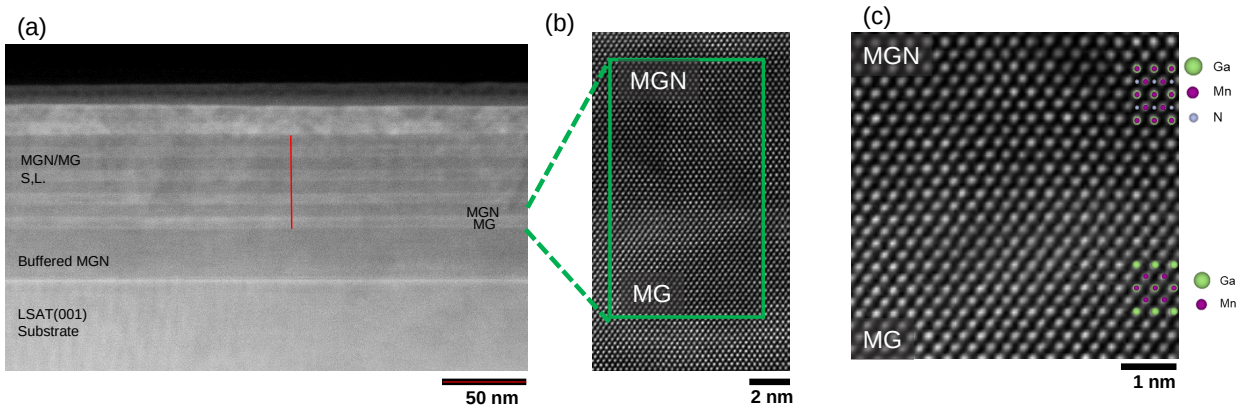

Figure 4.2: (a) Low magnification STEM along the (110) zone axis shows the substrate, MGN buffer layer, and superlattice structure, with the darker layers corresponding to MGN and the lighter to MG. The clear contrast indicates distinct neighboring layers without serious cation interdiffusion. High-resolution STEM images show the high-quality interface between MGN and MG. (b) Adjacent MGN and MG layers are shown with no clear defects from the interface. (c) The interface between MG and MGN is coherent, and stacks of atoms are uninterrupted across the interface. To illustrate the structure, the crystal atomic structures are overlayed on the STEM image.

the same structure in the $[001]$ orientation, and the next atomic layer differs only by the presence or absence of the Nitrogen anion. The bulk in-plane lattice constant of MG is 3.90 $\mathring{A}$, while that of our thin-film MGN is 3.91 $\mathring{A}$, only a 0.2 $\%$ difference[92]. These factors combine to allow high-quality superlattices of MG and MGN to be grown in a way that does not degrade either's structural or magnetic properties.

Here, we demonstrate tuning magnetic properties of thin-film MG via artificially layered superlatticing with MGN. MG has a strong out-of-plane magnetic easy axis when grown in $[001]$-oriented epitaxial thin films[78]. While our epitaxial MG thin films retain their quality and orientation in the superlattice, our magnetometry indicates the magnetization is more easily pulled in plane in the superlattice films compared to single-layer MG films. Our polarized neutron reflectometry (PNR) measurements show that this weakening of the MG anisotropy can be attributed to the MG/MGN interfaces. We discuss the possible origin and consequences of this change in

anisotropy.

4.2.1 Heterostructure growth

High-quality epitaxial growth of thin-film MG has previously proven difficult due to its tendency toward 3D island growth[93]. To overcome this we first grew a thick (53 nm) MGN buffer layer directly on an $(LaAlO3)_{0.3}(Sr_2TaAlO_6)_{0.7}$ (LSAT) (001) substrate, and subsequently grew MG directly on the buffer layer. X-ray diffraction (XRD), high-resolution scanning transmission electron microscopy (HRSTEM), and magnetometry all indicate this growth produces single-crystal MG with the c-axis oriented out of plane. At room temperature, the in-plane lattice constants of MG are 3.904 $\mathring{A}$, while our MGN films on LSAT are 3.91 $\mathring{A}$. Furthermore, MG and MGN have the same MnGa layer arrangement, making MGN an ideal template for oriented MG growth. Such a heterostructure also allows for the bottom MG interface to be the same for all layers and films.

Epitaxial bilayers (Fig. 4.1(c)) and superlattices (Fig. 4.1(d)) of MGN and MG were grown onto (001) LSAT substrates using DC reactive magnetron sputtering of a Mn_3Ga target. The base MGN layer was deposited with the substrate held at 550^o C and under a 10 mTorr (1.33 Pa) mixture of 89% Ar and 11% N_2. All subsequent layers were grown at 350^oC to avoid MG decomposition. MGN superlattice layers were grown using the previously described sputtering gas mixture, while MG layers were deposited with 3 mTorr (0.4 Pa) of pure Ar. Total pressure as well as N_2 partial pressure were changed between superlattice layers, with deposition paused for up to 3 minutes of stabilization time before resuming growth. The superlattice sample consists of seven repeats of a MG/MGN bilayer grown on the MGN base layer, then capped by a final MG layer (Fig. 4.1(d)), the same thickness as in the superlatticed portion, to avoid reaction (or oxidation) of the MGN with air.

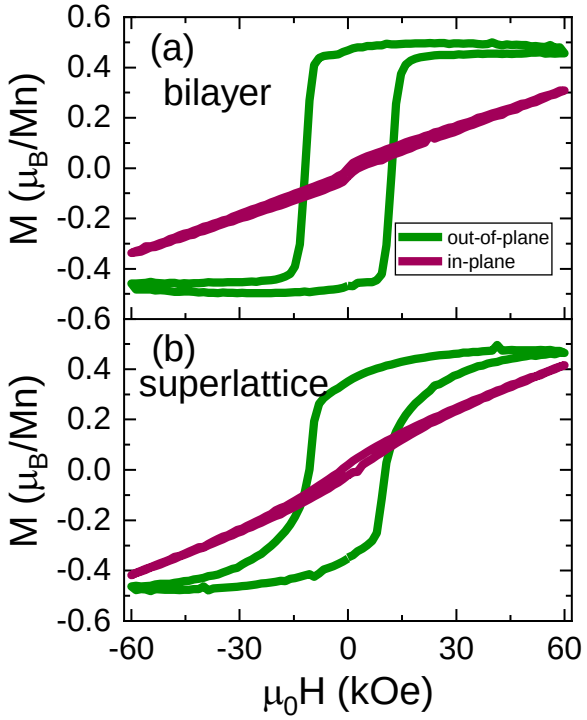

Figure 4.3: Magnetization (M) vs magnetic field ($\mu_0 H$) of (a) 30nm MG/ 53nm MGN bilayer film and (b) our superlattice film, sample A with nominal thickness info of 8 nm MG cap layer/(10 nm MGN/8 nm MGN)$_{x7}$ /53nm MGN . Out-of-plane orientations are shown in green, and in-plane orientations are shown in red. All Mn used for the M units refer only to the nominal Mn in MG, not MGN since the MG provides the dominant net moment.

Out-of-plane XRD of the superlattice sample shows broad MGN and MG c-axis diffraction peaks. MGN has a c-lattice parameter slightly larger than LSAT, placing its peak at 46.6^o just below the substrate peak; while MG has a c-lattice parameter of $7.1\mathring{A}$, giving it a (004) peak at 51.4^o. Both such peaks are over-layered with superlattice reflections, and so not indicated in Fig. 4.1(e). In Fig. 4.1(f) we index the superlattice reflections and determine the superlattice modulation length is 17.7 nm. The nominal thicknesses of MG and MGN in each superlattice repeating unit is 8 nm and 10 nm, respectively, repeated seven times. The nominal repeat unit thickness calibrated from the growth rate, is consistent with the XRD measurements. Since neutrons have very different sensitivity from X-rays, we can separate MGN and MG layer thicknesses from the neutron data, which we discuss in more detail later. The layer thicknesses based on neutron reflectometry are 9.7 nm of MG and 8.5 nm of MGN, as summarized in supplemental Table I []. This contrasts with the nominal thickesses in that the MG layer is larger while the MGN layer is smaller. We speculate the lack of N_2 gas during MG growth lead to the loss of Nitrogen in the adjacent MGN layer, resulting in neutrons perceiving thinner MGN and thicker MG. To check the reproduciblity of our results, we grew and measured two samples. The sample discussed so far, and continue to discuss in the main text, we refer to as sample A, while sample B showed the same phenomena. Bilayer MG films were grown with a similar approach where a base layer of 53 nm of MGN was deposited directly on the substrate, followed by 30 nm of MG as depicted in Fig. 4.1(c).

Cross-sectional STEM confirmed the layer structure and interface sharpness. The low-magnification STEM image along the $[110]$ zone axis, shown in Fig. 4.2(a), clearly shows layered bright and dark regions from the MG and MGN layers, respectively. The contrast arises from the higher density of MG relative to MGN due to narrower out-of-plane spacing of MG, leading to relatively brighter MG layers. MG and MGN cation sublattices differ in that the MnGa layer is shifted half a unit cell

in the $[110]$ direction along the c-axis in MG, doubling the unit cell and enabling tighter packing. When viewed along the $[110]$ zone axis, the MG and MGN cation lattices appear identical (Fig. 4.2(b)); while along the $[100]$ zone axis the offset of the MnGa layer is apparent, as shown in Fig. 4.3. This discrepancy allows interfaces to be identified to only within two MGN unit cells. STEM performed on MG/MGN superlattice samples gave layer thicknesses in good agreement with the X-ray reflectivity measurements. The higher-magnification image in Fig. 4.2(c) shows uninterrupted cation stacking across the interface. Such high-quality oriented growth is vital for the MG to exhibit perpendicular magnetic anisotropy over the entire sample.

4.2.2 Magnetization and neutron diffraction measurements

To measure the perpendicular magnetic anisotropy of the MG in our samples, we used SQuID magnetometry to measure the out-of-plane magnetization versus magnetic field. The bilayer result, shown in Fig. 4.3(a), indicates an easy axis with a saturation magnetization of 0.48 μ_B/Mn, arising from the magnetic response of the MG layer. This value is larger than the 0.33 μ_B/Mn reported for stoichiometric MG films. Such an increase in saturation magnetization has been previously attributed to Mn deficiency, as Mn vacancies prefer minority Mn1 sites[78,83,93]. Notably, this enhancement did not impact the out-of-plane anisotropy of the MG magnetization. We carefully determined that our superlattice sample showed a similar saturation magnetization (Fig. 4.3(b)). Thus, MG in the bilayer and superlattice had similar Mn levels, allowing our measurements to probe intrinsic differences between the bilayer and superlattice samples.

Differences between bilayer and superlattice samples were apparent in the magnetic switching. This was characterized by SQUID magnetometry, measuring both in-plane and out-of-plane net moments of the films, shown in Fig. 4.3. The magnetization was computed per stoichiometric

Mn in the MG layers according to the nominal thickness since the MGN is antiferromagnetic with insignificant magnetization. Both samples showed similar out-of-plane coercive fields of approximately 1.2 T, and similar saturation magnetizations around 0.48 μ_B/Mn. The bilayer film's out-of-plane hysteresis loop was close to square, indicative of a strong out-of-plane easy axis anisotropy. This contrasted with the superlattice sample which showed significantly more curvature through the switching, indicative of a portion of the magnetization rotating in-plane at zero field due to a weaker out-of-plane anisotropy. The in-plane magnetization curves for both films support this interpretation, as the bilayer sample showed near-ideal hard-axis character, while the superlattice shows a non-linear contribution at fields below 3 T. Thus, with in-plane field, at 3 T the superlattice sample has more in-plane magnetization than the bilayer sample. We determined from the in-plane magnetization measurements an out of plane anisotropy energy density of 1.2 MJ/m^3 for the bilayer in good agreement with Rode et al and 0.85 MJ/m^3 for the superlattice[78]. This value is roughly 40 times larger than the thin-film demagnetizing energy density indicating that this change in anisotropy is intrinsic to the MG. The similarity in the out-of-plane coercive fields between the bilayer and superlattice samples suggests that only a portion of the MG layers is subject to the reduced anisotropy.

To check this, we study the in-plane magnetization in the superlattices by performing room-temperature polarized neutron reflectometry measurements (PNR). PNR senses only the net in-plane magnetization, through the spin-dependent neutron reflectivities. We applied a 3 T in-plane field for all measurements to partially rotate the magnetization in-plane. Incident and scattered neutrons were spin-polarized either parallel or antiparallel to this applied in-plane field. We focus on the non-spin flip reflectivities ($R^{\uparrow\uparrow}$ and $R^{\downarrow\downarrow}$), (red and blue data of Fig. 4.4(a)) in which the incident and scattered neutrons possess the same spin direction. These are sensitive to the

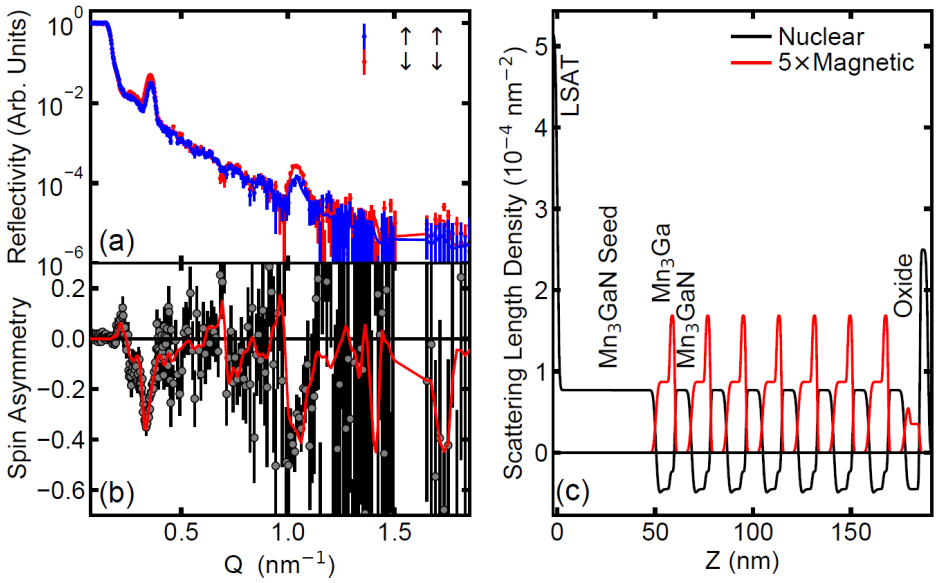

Figure 4.4: Polarized Neutron Reflectometry (PNR) results for sample A. The nuclear reflectivity (a) and spin asymmetry profile (b) vs scattering vector at RT under a 3 T in-plane magnetic field of the superlattice. The solid red line is the fit and grey dots with black error bars show the experimental data. The SLD real-space profiles are shown in (c). The black line shows the nuclear SLD that is indicative of the stoichiometry of layer, while the red line shows magnetic SLD, which is proportional to the net in-plane magnetic moment. Error bars represent ± 1 standard deviation.

magnetization parallel to the applied magnetic field. The spin-flip reflectivities ($R\uparrow\downarrow$ and $R\downarrow\uparrow$) probe the in-plane magnetization perpendicular to the applied field, which is not expected to be present.

PNR measurements were carried out on both superlattice samples, but we focus here on the results from the sample A and discuss similar results from sample B in the supplemental material. Fig. 4.4(a) shows the spin-dependent neutron reflectivities, from which we calculated the associated spin asymmetry $(R^{(}\uparrow\uparrow) - R^{(}\downarrow\downarrow))/(R^{(}\uparrow\uparrow) + R^{(}\downarrow\downarrow))$ (Fig. 4.4(b)). We determined the nuclear and magnetic scattering length density (SLD) depth profiles (Fig. 4.4(c)) within the superlattice by optimizing the calculated fit to the experimental scattering vector (Q) -dependent reflectivity and spin asymmetry. The nuclear SLD indicates the elemental composition and density,

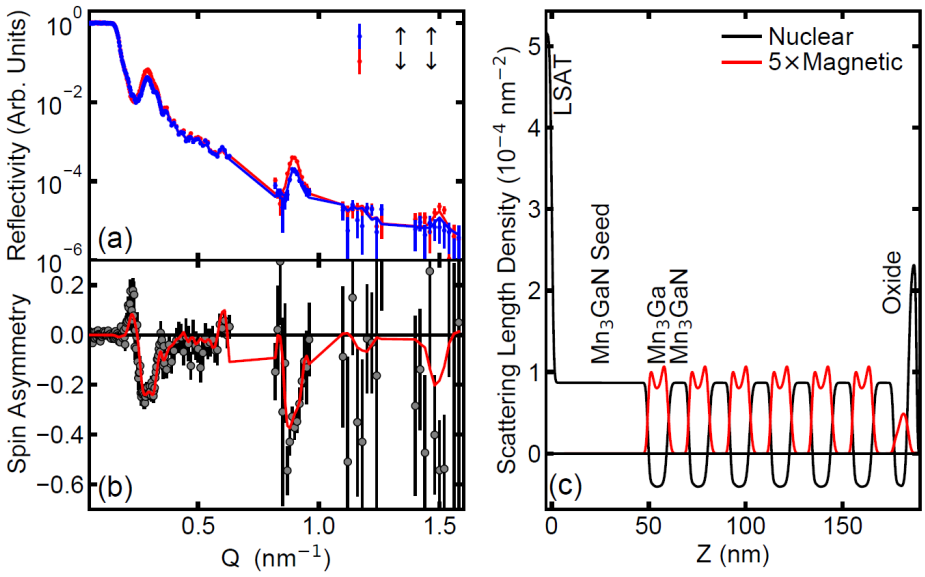

Figure 4.5: Polarized Neutron Reflectometry (PNR) results for sample B. The nuclear reflectivity (a) and spin asymmetry profile (b) vs scattering vector at RT under a 3 T in-plane magnetic field of the superlattice. The solid red line is the fit and grey dots with black error bars show the experimental data. The SLD real-space profiles are shown in (c). The black line shows the nuclear SLD that is indicative of the stoichiometry of layer, while the red line shows magnetic SLD, which is proportional to the net in-plane magnetic moment. Error bars represent ± 1 standard deviation.

while the magnetic SLD is directly proportional to the net in-plane magnetization parallel to the applied field. The horizontal axis Z is the distance from the LSAT substrate surface. More details on the measurement and fitting procedures are in the Supplemental Material.

We show reflectivity data (Fig. 4.4(a) (b)) for Q measured up through the fifth order superlattice Bragg reflections, and the optimal fit to the spin asymmetry signal. The spin asymmetry fits for both nuclear and magnetic SLD, translated into real space, are shown in Fig. 4.4(c) and match well with our nominal superlattice structure. While it is not necessary to include in the depth profiles any net magnetization in the MGN layers, as expected given the antiferromagnetic order, a nonuniform magnetization profile within the MG layer is necessary to fully capture the scattering across the entire measured Q range. In particular, a simple model assuming uniform magnetization within each MG layer fails to capture the spin-splitting at the 2nd, 3rd, and 5th order superlattice

reflections, as shown in 4.5. Allowing for a slight increase of the nuclear SLD and an enhancement of the magnetic SLD at the upper MG/MGN interface of each bilayer results in excellent agreement with the data for sample A. As discussed in the supplemental material, sample B fitting pointed toward magnetic SLD enhancement at both upper and lower MG/MGN interfaces. We conclude therefore that with a 3 T applied magnetic field in plane, the net in-plane magnetization in the MG is enhanced near these interfaces. This indicates a weakened perpendicular magnetic anisotropy at the interface that allows more in-plane magnetization rotation from the applied field, and is consistent with the smaller perpendicular anisotropy in the superlattices compared to the bilayer MG films determined from our magnetization measurements. Measurements on sample B, detailed in supplemental Fig. 4.5, support this interpretation of weakened magnetic anisotropy at the interface with limited differences; in sample B, the fitting pointed toward magnetic SLD enhancement at both MG/MGN interfaces.

4.2.3 Conclusions

Having identified that the observed superlattice weakened anisotropy arises from the MG/MGN interface, we now speculate about its origin. The HRSTEM images showed perfect cation structure across the interface, effectively ruling out a structural effect or a Mn stoichiometry effect at the interface. Furthermore, as the bilayer indicates, the slight strain from growing MG on MGN does not change the anisotropy. In fitting the neutron reflectometry profiles, concomitant with the interfacial bump in magnetic SLD, we find an increase in the nuclear SLD. As the nuclear scattering length of Nitrogen is relatively large, a small amount of Nitrogen diffused across the interface would cause this. We speculate that Nitrogen is accommodated within the partial Mn octahedra in MG (five nearest-neighbor Mn atoms), corresponding to its location in MGN at the Mn octahedra

centers. It is known that Mn-N-Mn exchange interactions control the MGN magnetic structure, and we argue that similar interactions are responsible for the change of the net anisotropy of the MG layer[37]. Transitioning between MGN and MG growth during superlattice synthesis could result in slightly different characteristics of the top and bottom interfaces, and potentially different Nitrogen diffusion at each of them. This could quantitatively change the magnetic anisotropy at the interface. We have successfully fabricated high-quality epitaxial MG/MGN superlattices and bilayer films with atomically smooth interfaces, in which the presence of nitrogen, an anion, in a constant cation stoichiometry controls the magnetic properties of the layers. Cross-sectional HRSTEM and XRD results confirm the correct phase and sharp interfaces. This demonstrates creation of a superlattice by only altering only the gas during growth. Magnetometry measurements show a reduced anisotropy energy in the superlattices that PNR data indicate arises from the MG/MGN interface. Our observations demonstrate that the magnetism of this MG/MGN system shows strong dependence on the bulk and surface chemistry, providing the capability to tune magnetic and spin transport properties. Our findings show a pathway to manipulate magnetism in this system with a small amount of chemical tuning, and a way to modify anisotropy characteristics for spintronic applications.

Chapter 5

Exchange Bias at a NonCollinear Antiferromagnet-Ferromagnet Interface

5.1 Context and My Contribution

The work in this chapter is the result of many people working together and could not exist without each persons' individual contribution. This project had film growth contribtuions from Dr. Tianxiang Nan of Chang-Beom Eom's group. My own contribtuions included electrical and magnetic measurements of the heterostructure samples and manuscript writing that resulted in the final publication.

The origin of this work stems from Dr. Tianxiang Nan's work studying spin torques in Mn_3GaN thin films. Spin-torque studies are often made in heterostructures consisting of a spintorque generating material, (Mn_3GaN) with a ferromagnet, often permalloy (Py), a soft room-temperature ferromagnet. While in previous spin-torque measurements the spin-torque generating material is a heavy metal magnetic exchange bias is not a consideration. But with Mn_3GaN having an antiferro-

magnetic structure, Dr. Nan thought it would be prudent to check for exhange bias, and so got me involved. I successfully characterized the exchange bias in multiple Py/Mn_3GaN samples that Dr. Nan grew, and in doing so made the discovery that exchange bias exists for $[001]$-oriented films, but not in $[111]$-oriented films.

I subsequently worked to understand the extant exchange better. The details of this discovery were both surprising and not surprising since Mn_3GaN is a non-collinear antiferromagnet, simple models of exchange bias did not apply. Furthermore many systems have shown robust exchange bias with very rough (not epitaxial) interfaces, and so while this result did fit into a well-understood paradigm of exchange bias, it also presented an opportunity to study exchange bias in a well-controlled epitaxial system. To do so, I used films grown by Dr. Nan who also did the structural characterization. I conceived and executed the magnetic characterization while discussing principally with Professor Rzchowski. The result is in the section that follows.

5.2 Exchange Bias at a NonCollinear Antiferromagnet - Ferromagnet Interface

Exchange bias at an antiferromagnetic–ferromagnetic bilayer heterointerface modulates the magnetic properties of the ferromagnetic layer through a modified coercivity, and a magnetic field offset, or bias, in its magnetization reversal characteristic. This has proven useful for magnetic and spintronic devices applications, as well as for probing magnetic order and interfacial interactions. It arises as the heterostructure is cooled through the Néel temperature of the antiferromagnetic layer, with the ferromagnetic layer aligned in an applied magnetic cooling field. The exchange coupling at the interface generates the bias, and the field cooling process can create an interfacial

spin arrangement perturbed from that of the original spin configuration[94–96].

Many antiferromagnets have a collinear spin configuration, where antiferromagnetically coupled spins have a common Néel axis along which they align. Extensive investigation of exchange bias at the interface with a collinear antiferromagnet has generated a large knowledge base for basic science and applications[97]. However, exchange coupling can occur with more complex characteristics at interfaces with noncollinear antiferromagnets[98–103]. Here we use magnetization and anisotropic magnetoresistance measurements of heterostructures of epitaxial films of the noncollinear spin material Mn_3GaN (MGN) and permalloy (Py, $Ni_{0.80}Fe_{0.20}$) to show that the interfacial exchange configuration, and its domain structure, can be manipulated with cooling field magnitude and direction. This provides a method to control electronic and magnetic properties of MGN, with potential applications for spintronic heterostructures.

The antiferromagnetic metallic nitride Mn_3GaN has an antiperovskite crystal structure and a noncollinear spin configuration. In the case of Mn_3GaN the interchanged anion and cation positions of the antiperovskite structure relative to perovskite provides three Mn magnetic ions (2.68 μ_B/Mn[104]) per unit cell rather than one per cell in Mn-based perovskites. This leads to a noncollinear antiferromagnetic spin configuration with a bulk Néel temperature near 360 K in thin films and a Γ^{5g} (magnetic space group: $R3\bar{m}$) spin structure coplanar in the (111) planes (Fig. 1a). The 120^o angles between neighboring Mn spins arise from a competition between the Mn crystal field and Ga-mediated exchange interactions between neighboring Mn[37], resulting in $\{111\}$ easy planes and face-diagonal easy axes. These magnetic orderings determine functional properties, such as magnetoresistance[105] , magnetovolume[89,106,107], magneto-caloric[108,109], and barocaloric[110] effects. Recently, it has been shown that the noncollinear spin structure in Mn_3GaN heterostructures can generate charge-spin conversion with unconventional spin polarization through a Berry

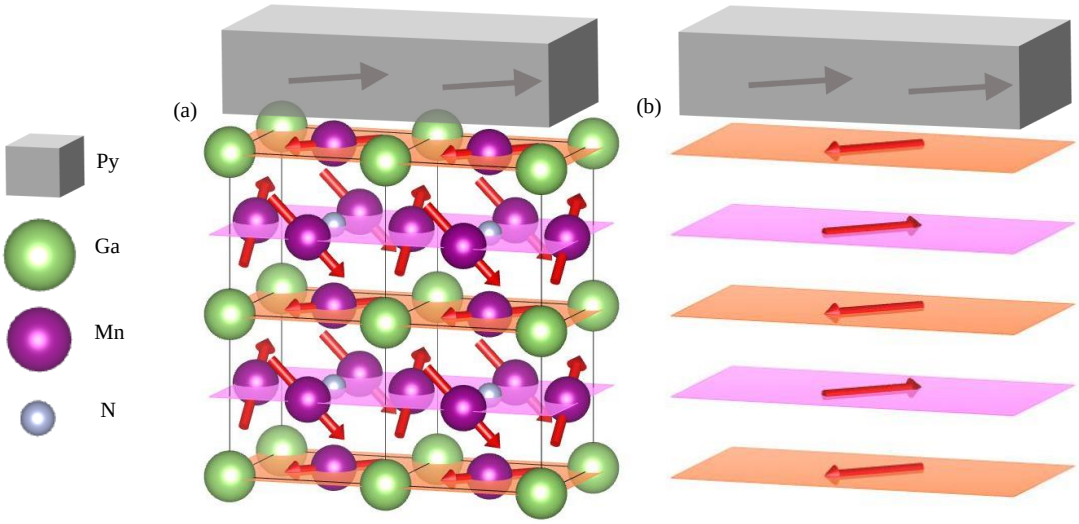

Figure 5.1: (a) Spin structure of Mn_3GaN in the Γ^{5g} configuration for the (001) crystal orientation. The interface plane of a (001) exchange bias heterostructure is a horizontal plane of the cube. The red arrows show the direction of the local Mn moment in the Γ^{5g} magnetic structure, and the orange planes highlight the GaMn planes while the pink planes highlight the Mn_2N planes. The net moment in each orange and pink plane is equal in magnitude (b), and pointing in alternating directions, despite the noncollinear nature of the individual spins. The (001) interface MnGa-termination plane with the Γ^{5g} magnetic configuration has a net planar ferromagnetic moment in the $< 110 >$ direction, while the Mn_2N-termination plane is a ferrimagnetic layer, with no net out-of-plane moment, and an in-plane layer net moment opposite to that of the MnGa layer. The grey blocks indicate the permalloy, which is ferromagnetic.

phase mechanism[77].

We study this noncollinear antiferromagnetic order through exchange bias in thin-film heterostructures of epitaxial antiperovskite Mn_3GaN interfaced with the soft ferromagnet permalloy (Py, $Ni_{0.80}Fe_{0.20}$). Epitaxial Mn_3GaN thin films were grown on (001) $(La_{0.3}Sr_{0.7})(Al_{0.65}Ta_{0.35})O_3$ (LSAT) substrates by reactive magnetron sputtering with in-situ high-pressure RHEED as described previously[36]. The high crystalline quality of Mn_3GaN and the cube-on-cube epitaxial relationship between the film and substrate were confirmed by x-ray diffraction. Single layer films were characterized by SQuID magnetization measurements of unpatterned samples, and magnetotransport of samples patterned into 100μm wide bars for variable field angle transport measurements. Ferromagnetic polycrystalline permalloy Ni80Fe20 (Py) was sputtered in situ without breaking vacuum onto the Mn_3GaN epitaxial films to form Mn_3GaN/Py exchange-bias bilayer heterostructures. The heterostructures were also patterned for anisotropic magnetoresistance (AMR) measurements, or left unpatterned for magnetization measurements. Atomic force microscope images of the 10 nm Py/20 nm Mn_3GaN surface indicate an atomically-smooth surface with a surface roughness of about 0.2 nm.

The Mn_3GaN epitaxial single layer films show a Néel temperature near 360 K, identified by magnetometry, Hall transport, and X-ray and neutron scattering measurements of lattice expansion[110]. The interfacial exchange interaction was initially investigated with magnetometry by cooling from 400 K in different strengths and directions of the cooling magnetic field, then measuring magnetization (M) vs applied magnetic field (M vs. H) hysteresis sweeps along the direction of the cooling field. Figure 5.2 shows the exchange field and coercive field measured after 10 kOe field cooling as a function of temperature along $[110]$ for three different MGN thicknesses (34 and 20 nm), with fixed Py thickness of 8 nm. The M vs. H hysteresis sweeps (insets)

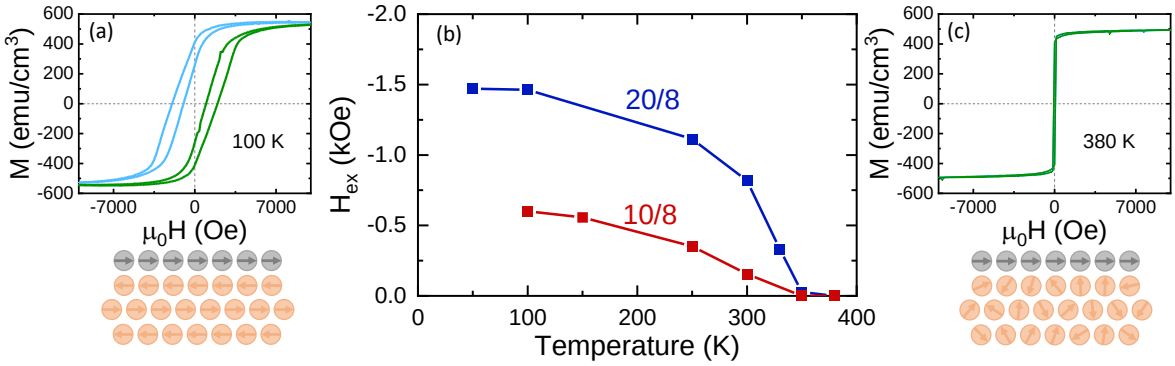

Figure 5.2: Temperature dependence of exchange bias in a Mn_3GaN / Permalloy bilayer for different MGN thicknesses 20 nm (blue), and 10 nm (red) after field cooling in 10 kOe with H —— [100]. The outsets show M vs H at temperatures above (T=380 K, right) and below (T=100 K, left) the Neel temperature, for positive (light blue) and negative (green) cooling field of 10 kOe. Above the Neel temperature the exchange bias field is zero, and the M vs H data sets overlap.

show the effects of interface interaction on loop shape above and below the Néel temperature. The negligible exchange field and small coercive field above the Néel temperature (show temperature in the inset) are consistent with paramagnetic Mn_3GaN. The blocking temperature below which the exchange field and coercive field become nonzero correlates with the Néel temperature. The increasing exchange field with MGN thickness suggests that the length scale on which the MGN spin configuration can be perturbed is greater than 20 nm.

Figure 5.3 shows the dependence of exchange field on the magnitude of the cooling field, and on the Mn_3GaN film thickness, with a fixed Py thickness of 8 nm in the thin-MGN regime. The negative exchange bias indicates antiferromagnetic coupling of the interfacial Mn_3GaN spins with the Py magnetization[94,111,112]. The dependence of the exchange bias on cooling field suggests an additional coupling of the interfacial Mn_3GaN spins with the external field, or a twist of the non-collinear spin configuration through the film thickness. In the former scenario, zero exchange bias occurs when the interfacial coupling and external Zeeman coupling are equal. We can then compute the theoretical cooling field of zero exchange bias. A single layer of interfacial Mn with 2.68

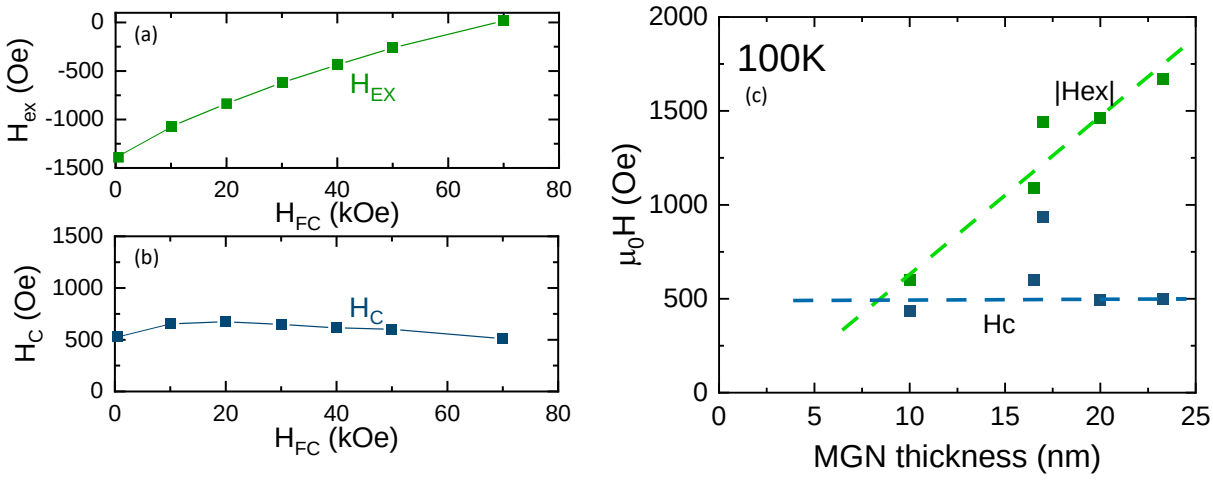

Figure 5.3: Cooling field dependence of the exchange field H_{ex} (a) and coercive field H_C (b) for Mn_3GaN (20 nm) / Permalloy (8 nm) bilayer at $T = 200$ K, measured with $H \parallel [110]$. MGN thickness dependence of He (green) and Hc (purple) at $T = 100$ K (c) after field cooling in 10 kOe.

μ_B/Mn results in zero exchange field when cooled at 15 kOe, much smaller than the 70 kOe field we observe. We also note that our Py /(111)-oriented Mn_3GaN thin film heterostructures grown by the same procedure don't show exchange bias. This is consistent with the compensated interfacial $\{111\}$ planes having zero net moment (see Fig. 5.1), whereas the (001) Mn_2N uncompensated plane contains aligned spins.

We use anisotropic magnetoresistance (AMR) to probe the MGN noncollinear antiferromagnetic order. As discussed previously, magnetic anisotropy in Mn_3GaN prefers a spin direction along the face diagonals of the unit cell, the $[110]$ direction at the MGN / Py interface of our heterostructures. This anisotropy influences the interfacial spin configuration that determines exchange bias. In its simplest form AMR effectively measures the angle between the magnetization and electrical current direction due to a $\cos^2\theta$ dependence of the longitudinal resistance (along the direction of the current) on the angle θ between the magnetization and current direction. Here Py (50 $\mu\Omega$-cm at 300 K) and MGN (150 $\mu\Omega$-cm at 300 K) are both conducting in our Py (10 nm) /

MGN (20 nm) heterostructures. In single-layer MGN we do not observe anisotropic magnetoresistance at room temperature, consistent with the absence of net magnetization, and so attribute the AMR signal to the Py layer.

Multiple magnetic domains in the Py layer along the current path complicate exact modeling of the AMR response, making quantitative extraction of the exchange or coercive field difficult. However, general AMR response characteristics allow straightforward determination of the exchange bias anisotropy axis. For instance, magnetic field applied along a uniaxial exchange bias anisotropy axis reverses magnetization by growing domains parallel or antiparallel to the anisotropy axis without substantial magnetization rotation. In this case the AMR $\cos^2\theta$ dependence would then be mostly independent of applied magnetic field as θ switches abruptly from 0^o to 180^o. Alternatively, magnetic field applied at an angle to a uniaxial anisotropy axis rotates magnetization during reversal, resulting in a strong dependence of AMR on applied magnetic field strength as the magnetization changes angle with respect to the electrical current direction.

Figure 5.4a shows room-temperature AMR measurements after field cooling at 5 kOe with electric current along the MGN $[100]$ direction. The cooling field is along a $[110]$ MGN crystal axis, and the measuring field direction is either parallel (blue), or perpendicular (purple) to the cooling field. The small AMR amplitude for cooling and measurement fields aligned along the $[110]$ direction (blue) indicates minimal magnetization rotation during reversal. This indicates a magnetization originally along $[110]$ and abruptly switched 180^o by the measuring field, consistent with a $[110]$ axis made easy by the exchange bias. The purple curve, with measuring field perpendicular to the cooling field, shows a large AMR amplitude, indicating magnetization rotation during the measuring field sweep. This is also consistent with a $[110]$ exchange bias easy axis, with a magnetization now pulled away from the easy axis and rotating toward the perpendicular mea-

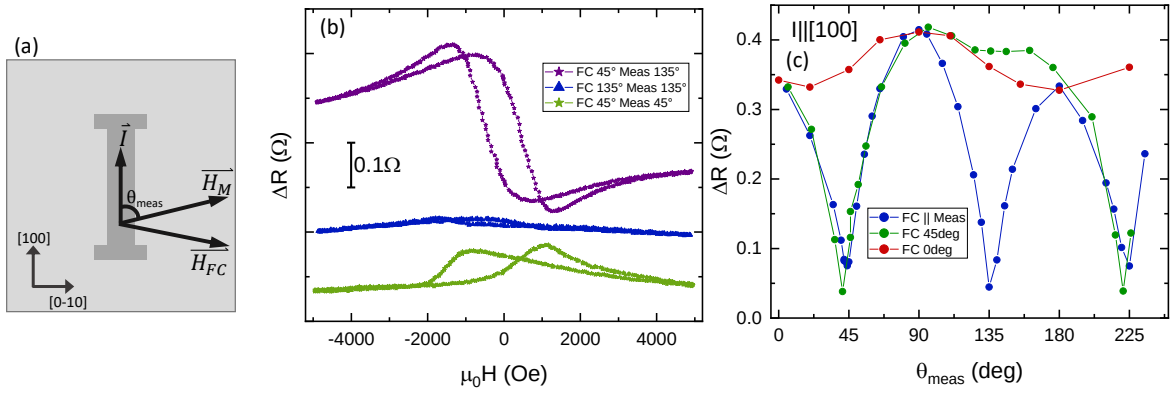

Figure 5.4: Part (a) shows the measurement schematic diagram, with all angles measured in reference to the current direction, which remains fixed. Room temperature longitudinal magnetoresistance vs measurement magnetic field after field cooling through the Neel temperature for different 5 kOe field cooling directions (b), and for different measurement field directions. Current is parallel to the $[100]$ direction. A mostly constant magnetoresistance (small amplitude) with field (blue, green) indicates magnetization remaining parallel or antiparallel to the applied field direction during magnetization reversal. A large amplitude magnetoresistance indicates magnetization rotation during reversal. AMR amplitude vs measurement angle for field cooling direction relative to $< 100 >$ fixed at 0^o (red), fixed at 45^o (green) (c), and varying so that the field cooling direction and measurement direction are the same (blue).

suring field. This indicates that field cooling along a face diagonal produces a uniaxial exchange bias anisotropy axis along those same directions.

Figure 5.4b generalizes these results to other cooling field angles, showing the AMR amplitude (difference between maximum and minimum AMR) vs measurement field direction relative to the $[100]$ crystalline axis. We show that these data indicate all cooling field directions result in an exchange bias anisotropy axis always along a face diagonal. This suggests that Mn spins relax to align with the nearest face diagonal after the cooling field is removed, and then exchange coupling across the interface makes this the anisotropy axis for exchange bias. This is consistent with a Γ^{5g} spin configuration and a strong MGN magnetocrystalline anisotropy preserving the Γ^{5g} configuration after field cooling.

We first discuss the blue curve of Fig. 5.4b, where the measuring field is aligned in the cooling

field direction, but both at various angles with respect to the MGN $[100]$ direction. The minima at 45^o and 135^o indicate a small difference between maximum and minimum AMR during the measuring field sweep, similar to the blue curve of Fig. 4a). This indicates minimal magnetization rotation during the AMR field sweep at these two angles, consistent with the magnetization reversal by domain switching that would occur along an anisotropy axis. We interpret this as field cooling positioning MGN interfacial spins along either the $[110]$ or $[1\bar{1}0]$ face diagonals. However when either the cooling field or the measurement field deviates away from 45^o and 135^o the AMR amplitude increases, indicating increasing magnetization rotation during reversal. This shows that the measuring field is no longer aligned with the exchange bias axis, indicating that the MGN spin has relaxed away from the field cooling direction. The AMR amplitude maxima at 90^o and 180^o are in fact consistent with exchange bias axes near $[110]$ or $[1\bar{1}0]$ for all cooling field directions, which are the nearest face diagonals, as is the reflection symmetry of the data around the minimum angles. Our interpretation is that the MGN crystal anisotropy dominates here, and that the exchange bias axis is the nearer of $< 110 >$ or $< 1\bar{1}0 >$ to the cooling field direction due to MGN spins relaxing to the face diagonal direction after removing the cooling field.

We support this by further measurements (Fig. 5.4b, green data set) with cooling field fixed along $< 110 >$, but with variable measurement field angle. Again, each point is the amplitude of a full AMR field sweep. The minimum at 45^o measuring field (along the $< 110 >$ cooling field direction) is still present, and the maximum AMR amplitude for measurement field along 135^o (perpendicular to the $< 110 >$ cooling field direction indicates field-induced rotation of the magnetization similar to the purple curve of panel a). The red data set of Fig. 5.4b has fixed cooling field direction along $[100]$, and varying measurement field direction. The $[100]$ cooling field is midway between the $[110]$ and $[1\bar{1}0]$ MGN interface plane magnetic anisotropy axes, producing a

mixture of antiferromagnetic domains in the MGN film, with then a mixture of Py domain growth and rotation during reversal. This leads to a smaller variation in AMR amplitude than seen for the cooling directions already discussed. The exact symmetry and shape would depend on the MGN antiferromagnetic domain configuration.

This indicates that the MGN antiferromagnetic domain structure can be controlled by exchange interactions with a neighboring ferromagnetic layer. This control of noncollinear domain structure provides control of spintronic effects such as charge to spin conversion in noncollinear systems[110], leading to spintronic device applications. Another exchange bias control unique to noncollinear spin systems involves transport properties arising from Berry phase mechanisms. Competition between the MGN magnetocrystalline anisotropy[113] and the interfacial exchange interaction with Py spins could produce field-dependent deformations of the MGN noncollinear spin structure as Py spins are manipulated with applied magnetic field. Such deformations of the MGN spin structure would alter the anomalous hall effect in MGN, which is absent in the ground state Γ^{5g} spin configuration, but nonzero in the related Γ^{4g} spin structure[110]. Theoretical understanding of Berry phase transport properties in distorted noncollinear spin structures would open new directions in MGN-based spintronic heterostructures.

Bibliography

[1] Koichi Momma and Fujio Izumi. *VESTA3* for three-dimensional visualization of crystal, volumetric and morphology data. *Journal of Applied Crystallography*, 44(6):1272–1276, Dec 2011.

[2] T. J. Anderson, S. Ryu, H. Zhou, L. Xie, J. P. Podkaminer, Y. Ma, J. Irwin, X. Q. Pan, M. S. Rzchowski, and C. B. Eom. Metastable honeycomb SrTiO3/SrIrO3 heterostructures. *Applied Physics Letters*, 108(15):151604, April 2016.

[3] D. Haskel, G. Fabbris, Mikhail Zhernenkov, P. P. Kong, C. Q. Jin, G. Cao, and M. van Veenendaal. Pressure Tuning of the Spin-Orbit Coupled Ground State in \${\mathrm{Sr}}_{2}{\mathrm{IrO}}_{4}\$. *Physical Review Letters*, 109(2):027204, July 2012.

[4] S. Nakatsuji, Y. Machida, Y. Maeno, T. Tayama, T. Sakakibara, J. van Duijn, L. Balicas, J. N. Millican, R. T. Macaluso, and Julia Y. Chan. Metallic Spin-Liquid Behavior of the Geometrically Frustrated Kondo Lattice Pr 2 Ir 2 O 7. *Physical Review Letters*, 96(8), March 2006.

[5] John S Townsend. *A Modern Approach to Quantum Mechanics*. University Science Books, 200.

[6] F. Hund. Zur Deutung verwickelter Spektren, insbesondere der Elemente Scandium bis Nickel. *Zeitschrift für Physik*, 33(1):345–371, 1925.

[7] David L. Sidebottom. *Fundamentals of Condensed Matter and Crystalline Physics: An Introduction for Students of Physics and Materials Science*. Cambridge University Press, 2012.

[8] Thomas Wolfram and Sinasi Ellialtioglu. *LCAO energy band model for cubic perovskites*, page 1–76. Cambridge University Press, 2006.

[9] A. Ohtomo and H. Y. Hwang. A high-mobility electron gas at the $LaAlO_3$/$SrTiO_3$ heterointerface. *Nature*, 427(6973):423–426, January 2004.

[10] Gang Cao and Pedro Schlottmann. The challenge of spin–orbit-tuned ground states in iridates: a key issues review. *Reports on Progress in Physics*, 81(4):042502, 2018.

[11] J. P. Clancy, N. Chen, C. Y. Kim, W. F. Chen, K. W. Plumb, B. C. Jeon, T. W. Noh, and Young-June Kim. Spin-orbit coupling in iridium-based 5d compounds probed by x-ray absorption spectroscopy. *Physical Review B*, 86(19):195131, November 2012.

[12] M. A. Laguna-Marco, D. Haskel, N. Souza-Neto, J. C. Lang, V. V. Krishnamurthy, S. Chikara, G. Cao, and M. van Veenendaal. Orbital Magnetism and Spin-Orbit Effects in the Electronic Structure of ${\mathrm{BaIrO}}_{3}$. *Physical Review Letters*, 105(21):216407, November 2010.

[13] G. van der Laan and B. T. Thole. Local Probe for Spin-Orbit Interaction. *Physical Review Letters*, 60(19):1977–1980, May 1988.

[14] B. T. Thole and G. van der Laan. Branching ratio in x-ray absorption spectroscopy. *Physical Review B*, 38(5):3158–3171, August 1988.

[15] B. T. Thole and G. van der Laan. Linear relation between x-ray absorption branching ratio and valence-band spin-orbit expectation value. *Physical Review A*, 38(4):1943–1947, August 1988.

[16] F. M. F. De Groot, Z. W. Hu, M. F. Lopez, G. Kaindl, F. Guillot, and M. Tronc. Differences between *L* 3 and *L* 2 x-ray absorption spectra of transition metal compounds. *The Journal of Chemical Physics*, 101(8):6570–6576, October 1994.

[17] L. J. van der PAUW. A method of measuring specific resistivity and hall effect of discs of arbitrary shape. In *Semiconductor Devices: Pioneering Papers*, pages 174–182. WORLD SCIENTIFIC, March 1991.

[18] O. Bierwagen, R. Pomraenke, S. Eilers, and W. T. Masselink. Mobility and carrier density in materials with anisotropic conductivity revealed by van der Pauw measurements. *Physical Review B*, 70(16):165307, October 2004.

[19] Oliver Bierwagen, Tommy Ive, Chris G. Van de Walle, and James S. Speck. Causes of incorrect carrier-type identification in van der Pauw–Hall measurements. *Applied Physics Letters*, 93(24):242108, December 2008.

[20] Naoto Nagaosa, Jairo Sinova, Shigeki Onoda, A. H. MacDonald, and N. P. Ong. Anomalous Hall effect. *Reviews of Modern Physics*, 82(2):1539–1592, May 2010.

[21] E. H. Hall. On a New Action of the Magnet on Electric Currents. *American Journal of Mathematics*, 2(3):287–292, 1879. Publisher: Johns Hopkins University Press.

[22] E.H. Hall. XVIII. On the "Rotational Coefficient" in nickel and cobalt. *The London, Edinburgh, and Dublin Philosophical Magazine and Journal of Science*, 12(74):157–172, September 1881. Publisher: Taylor & Francis _eprint: https://doi.org/10.1080/14786448108627086.

[23] E. M. Pugh and T. W. Lippert. Hall e.m.f. and intensity of magnetization. *Phys. Rev.*, 42:709–713, Dec 1932.

[24] M. Khalid, A. Setzer, M. Ziese, P. Esquinazi, D. Spemann, A. Pöppl, and E. Goering. Ubiquity of ferromagnetic signals in common diamagnetic oxide crystals. *Phys. Rev. B*, 81:214414, Jun 2010.

[25] Jun Ge, Da Ma, Yanzhao Liu, Huichao Wang, Yanan Li, Jiawei Luo, Tianchuang Luo, Ying Xing, Jiaqiang Yan, David Mandrus, Haiwen Liu, X C Xie, and Jian Wang. Unconventional Hall effect induced by Berry curvature. *National Science Review*, 7(12):1879–1885, December 2020.

[26] Tirthankar Chakraborty, Kartik Samanta, Satya N. Guin, Jonathan Noky, Iñigo Robredo, Suchitra Prasad, Juergen Kuebler, Chandra Shekhar, Maia G. Vergniory, and Claudia Felser. Berry curvature induced anomalous Hall conductivity in the magnetic topological oxide double perovskite ${\mathrm{Sr}}_{2}{\mathrm{FeMoO}}_{6}$. *Physical Review B*, 106(15):155141, October 2022. Publisher: American Physical Society.

[27] Gautam Gurung, Ding-Fu Shao, Tula R. Paudel, and Evgeny Y. Tsymbal. Anomalous Hall Conductivity of a Non-Collinear Magnetic Antiperovskite. *arXiv:1901.05040 [cond-mat]*, January 2019. arXiv: 1901.05040.

[28] J. Zemen, E. Mendive-Tapia, Z. Gercsi, R. Banerjee, J. B. Staunton, and K. G. Sandeman. Frustrated magnetism and caloric effects in Mn-based antiperovskite nitrides: Ab initio theory. *Physical Review B*, 95(18):184438, May 2017.

[29] Ping-Chun Wu, Chia-Chun Wei, Qilan Zhong, Sheng-Zhu Ho, Yi-De Liou, Yu-Chen Liu, Chun-Chien Chiu, Wen-Yen Tzeng, Kuo-En Chang, Yao-Wen Chang, Junding Zheng, Chun-Fu Chang, Chien-Ming Tu, Tse-Ming Chen, Chih-Wei Luo, Rong Huang, Chun-Gang Duan, Yi-Chun Chen, Chang-Yang Kuo, and Jan-Chi Yang. Twisted oxide lateral homostructures with conjunction tunability. *Nature Communications*, 13(1):2565, May 2022. Number: 1 Publisher: Nature Publishing Group.

[30] Abhijit Biswas and Yoon H. Jeong. Growth and engineering of perovskite SrIrO 3 thin films. *Current Applied Physics*, 17(5):605–614, May 2017.

[31] S. J. Moon, H. Jin, K. W. Kim, W. S. Choi, Y. S. Lee, J. Yu, G. Cao, A. Sumi, H. Funakubo, C. Bernhard, and T. W. Noh. Dimensionality-Controlled Insulator-Metal Transition and Correlated Metallic State in 5 d Transition Metal Oxides Sr n + 1 Ir n O 3 n + 1 (n = 1 , 2, and oo). *Physical Review Letters*, 101(22), November 2008.

[32] J. Nichols, J. Terzic, E. G. Bittle, O. B. Korneta, L. E. De Long, J. W. Brill, G. Cao, and S. S. A. Seo. Tuning electronic structure via epitaxial strain in Sr_2IrO_4 thin films. *Applied Physics Letters*, 102(14):141908, April 2013.

[33] Jean-Michel Carter, V. Vijay Shankar, M. Ahsan Zeb, and Hae-Young Kee. Semimetal and Topological Insulator in Perovskite Iridates. *Physical Review B*, 85(11), March 2012.

[34] Jian Liu, D. Kriegner, L. Horak, D. Puggioni, C. Rayan Serrao, R. Chen, D. Yi, C. Frontera, V. Holy, A. Vishwanath, J. M. Rondinelli, X. Marti, and R. Ramesh. Strain-induced nonsymmorphic symmetry breaking and removal of Dirac semimetallic nodal line in an orthoperovskite iridate. *Physical Review B*, 93(8), February 2016.

[35] Z. T. Liu, M. Y. Li, Q. F. Li, J. S. Liu, W. Li, H. F. Yang, Q. Yao, C. C. Fan, X. G. Wan, Z. Wang, and D. W. Shen. Direct observation of the Dirac nodes lifting in semimetallic perovskite SrIrO3 thin films. *Scientific Reports*, 6(1), September 2016.

[36] Camilo X. Quintela, Kyung Song, Ding-Fu Shao, Lin Xie, Tianxiang Nan, Tula R. Paudel, Neil Campbell, Xiaoqing Pan, Thomas Tybell, Mark S. Rzchowski, Evgeny Y. Tsymbal, Si-Young Choi, and Chang-Beom Eom. Epitaxial antiperovskite/perovskite heterostructures for materials design. *Science Advances*, 6(30):eaba4017, July 2020. Publisher: American Association for the Advancement of Science.

[37] Masahito Mochizuki, Masaya Kobayashi, Reoya Okabe, and Daisuke Yamamoto. Spin model for nontrivial types of magnetic order in inverse-perovskite antiferromagnets. *Physical Review B*, 97(6):060401, February 2018.

[38] Yo Machida, Satoru Nakatsuji, Shigeki Onoda, Takashi Tayama, and Toshiro Sakakibara. Time-reversal symmetry breaking and spontaneous Hall effect without magnetic dipole order. *Nature*, 463(7278):210–213, January 2010.

[39] Takeshi Kondo, M. Nakayama, R. Chen, J. J. Ishikawa, E.-G. Moon, T. Yamamoto, Y. Ota, W. Malaeb, H. Kanai, Y. Nakashima, Y. Ishida, R. Yoshida, H. Yamamoto, M. Matsunami, S. Kimura, N. Inami, K. Ono, H. Kumigashira, S. Nakatsuji, L. Balents, and S. Shin. Quadratic Fermi node in a 3D strongly correlated semimetal. *Nature Communications*, 6:ncomms10042, December 2015.

[40] Bing Cheng, T. Ohtsuki, Dipanjan Chaudhuri, S. Nakatsuji, Mikk Lippmaa, and N. P. Armitage. Dielectric anomalies and interactions in the three-dimensional quadratic band touching Luttinger semimetal Pr 2 Ir 2 O 7. *Nature Communications*, 8(1):2097, December 2017.

[41] Kazuyuki Matsuhira, Makoto Wakeshima, Yukio Hinatsu, and Seishi Takagi. Metal–Insulator Transitions in Pyrochlore Oxides Ln2Ir2O7. *Journal of the Physical Society of Japan*, 80(9):094701, September 2011. Publisher: The Physical Society of Japan.

[42] J.-W. Kim, Y. Choi, S. H. Chun, D. Haskel, D. Yi, R. Ramesh, J. Liu, and P. J. Ryan. Controlling entangled spin-orbit coupling of $5d$ states with interfacial heterostructure engineering. *Physical Review B*, 97(9):094426, March 2018.

[43] Takumi Ohtsuki, Zhaoming Tian, Akira Endo, Mario Halim, Shingo Katsumoto, Yoshimitsu Kohama, Koichi Kindo, Mikk Lippmaa, and Satoru Nakatsuji. Strain-induced spontaneous Hall effect in an epitaxial thin film of a Luttinger semimetal. *Proceedings of the National Academy of Sciences*, page 201819489, April 2019.

[44] Bohm-Jung Yang and Yong Baek Kim. Topological insulators and metal-insulator transition in the pyrochlore iridates. *Physical Review B*, 82(8):085111, August 2010.

[45] J. Matsuno, K. Ihara, S. Yamamura, H. Wadati, K. Ishii, V. V. Shankar, Hae-Young Kee, and H. Takagi. Engineering a Spin-Orbital Magnetic Insulator by Tailoring Superlattices. *Physical Review Letters*, 114(24), June 2015.

[46] J. W. Kim, Y. Choi, Jungho Kim, J. F. Mitchell, G. Jackeli, M. Daghofer, J. van den Brink, G. Khaliullin, and B. J. Kim. Dimensionality Driven Spin-Flop Transition in Layered Iridates. *Physical Review Letters*, 109(3):037204, July 2012.

[47] Yilin Wang, Hongming Weng, Liang Fu, and Xi Dai. Noncollinear Magnetic Structure and Multipolar Order in ${\mathrm{Eu}}_{2}{\mathrm{Ir}}_{2}{\mathrm{O}}_{7}$. *Physical Review Letters*, 119(18):187203, November 2017. Publisher: American Physical Society.

[48] Daisuke Uematsu, Hajime Sagayama, Taka-hisa Arima, Jun J. Ishikawa, Satoru Nakatsuji, Hidenori Takagi, Masahiro Yoshida, Jun'ichiro Mizuki, and Kenji Ishii. Large trigonal-field effect on spin-orbit coupled states in a pyrochlore iridate. *Physical Review B*, 92(9):094405, September 2015.

[49] Keisuke Tomiyasu, Kazuyuki Matsuhira, Kazuaki Iwasa, Masanori Watahiki, Seishi Takagi, Makoto Wakeshima, Yukio Hinatsu, Makoto Yokoyama, Kenji Ohoyama, and Kazuyoshi Yamada. Emergence of Magnetic Long-range Order in Frustrated Pyrochlore Nd2Ir2O7 with Metal–Insulator Transition. *Journal of the Physical Society of Japan*, 81(3):034709, February 2012.

[50] H. Sagayama, D. Uematsu, T. Arima, K. Sugimoto, J. J. Ishikawa, E. O'Farrell, and S. Nakatsuji. Determination of long-range all-in-all-out ordering of Ir^{4+} moments in a pyrochlore iridate Eu${}_{2}$Ir${}_{2}$O${}_{7}$ by resonant x-ray diffraction. *Physical Review B*, 87(10):100403, March 2013.

[51] C. Donnerer, M. C. Rahn, M. Moretti Sala, J. G. Vale, D. Pincini, J. Strempfer, M. Krisch, D. Prabhakaran, A. T. Boothroyd, and D. F. McMorrow. All-in–all-Out Magnetic Order and Propagating Spin Waves in ${\mathrm{Sm}}_{2}{\mathrm{Ir}}_{2}{\mathrm{O}}_{7}$. *Physical Review Letters*, 117(3):037201, July 2016.

[52] Zach Porter, Eli Zoghlin, Samuel Britner, Samra Husremovic, Jacob P. C. Ruff, Yongseong Choi, Daniel Haskel, Geneva Laurita, and Stephen D. Wilson. Evolution of structure and magnetism across the metal-insulator transition in the pyrochlore iridate ${({\mathrm{Nd}}_{1\ensuremath{-}x}{\mathrm{Ca}}_{x})}_{2}{\mathrm{Ir}}_{2}{\mathrm{O}}_{7}$. *Physical Review B*, 100(5):054409, August 2019. Publisher: American Physical Society.

[53] T. C. Fujita, Y. Kozuka, M. Uchida, A. Tsukazaki, T. Arima, and M. Kawasaki. Odd-parity magnetoresistance in pyrochlore iridate thin films with broken time-reversal symmetry. *Scientific Reports*, 5:srep09711, May 2015.

[54] S. J. Moon, H. Jin, K. W. Kim, W. S. Choi, Y. S. Lee, J. Yu, G. Cao, A. Sumi, H. Funakubo, C. Bernhard, and T. W. Noh. Dimensionality-Controlled Insulator-Metal Transition and Correlated Metallic State in 5 d Transition Metal Oxides Sr n + 1 Ir n O 3 n + 1 (n = 1 , 2, and oo). *Physical Review Letters*, 101(22), November 2008.

[55] Jason K. Kawasaki, Masaki Uchida, Hanjong Paik, Darrell G. Schlom, and Kyle M. Shen. Evolution of electronic correlations across the rutile, perovskite, and Ruddelsden-Popper iridates with octahedral connectivity. *Physical Review B*, 94(12), September 2016.

[56] Y. F. Nie, P. D. C. King, C. H. Kim, M. Uchida, H. I. Wei, B. D. Faeth, J. P. Ruf, J. P. C. Ruff, L. Xie, X. Pan, C. J. Fennie, D. G. Schlom, and K. M. Shen. Interplay of Spin-Orbit Interactions, Dimensionality, and Octahedral Rotations in Semimetallic SrIrO 3. *Physical Review Letters*, 114(1), January 2015.

[57] T. Nan, T. J. Anderson, J. Gibbons, K. Hwang, N. Campbell, H. Zhou, Y. Q. Dong, G. Y. Kim, D. F. Shao, T. R. Paudel, N. Reynolds, X. J. Wang, N. X. Sun, E. Y. Tsymbal, S. Y. Choi, M. S. Rzchowski, Yong Baek Kim, D. C. Ralph, and C. B. Eom. Anisotropic spin-orbit torque generation in epitaxial SrIrO3 by symmetry design. *Proceedings of the National Academy of Sciences*, 116(33):16186–16191, August 2019.

[58] Narayan Mohanta, Elbio Dagotto, and Satoshi Okamoto. Topological Hall effect and emergent skyrmion crystal at manganite-iridate oxide interfaces. *Physical Review B*, 100(6):064429, August 2019. Publisher: American Physical Society.

[59] B. J. Kim, Hosub Jin, S. J. Moon, J.-Y. Kim, B.-G. Park, C. S. Leem, Jaejun Yu, T. W. Noh, C. Kim, S.-J. Oh, J.-H. Park, V. Durairaj, G. Cao, and E. Rotenberg. Novel ${J}_{\mathrm{eff}}=1/2$ Mott State Induced by Relativistic Spin-Orbit Coupling in ${\mathrm{Sr}}_{2}{\mathrm{IrO}}_{4}$. *Physical Review Letters*, 101(7):076402, August 2008.

[60] G. Jackeli and G. Khaliullin. Mott Insulators in the Strong Spin-Orbit Coupling Limit: From Heisenberg to a Quantum Compass and Kitaev Models. *Physical Review Letters*, 102(1):017205, January 2009.

[61] G. Cao, V. Durairaj, S. Chikara, L. E. DeLong, S. Parkin, and P. Schlottmann. Non-Fermi-liquid behavior in nearly ferromagnetic ${\mathrm{SrIrO}}_{3}$ single crystals. *Physical Review B*, 76(10):100402, September 2007.

[62] M. Ahsan Zeb and Hae-Young Kee. Interplay between spin-orbit coupling and Hubbard interaction in SrIrO 3 and related Pbnm perovskite oxides. *Physical Review B*, 86(8), August 2012.

[63] Jian Liu, J.-H. Chu, C. Rayan Serrao, D. Yi, J. Koralek, C. Nelson, C. Frontera, D. Kriegner, L. Horak, E. Arenholz, J. Orenstein, A. Vishwanath, X. Marti, and R. Ramesh. Tuning the electronic properties of J_eff=1/2 correlated semimetal in epitaxial perovskite SrIrO3. *arXiv:1305.1732 [cond-mat]*, May 2013. arXiv: 1305.1732.

[64] J. Fujioka, T. Okawa, A. Yamamoto, and Y. Tokura. Correlated Dirac semimetallic state with unusual positive magnetoresistance in strain-free perovskite SrIrO 3. *Physical Review B*, 95(12), March 2017.

[65] J. Matsuno, N. Ogawa, K. Yasuda, F. Kagawa, W. Koshibae, N. Nagaosa, Y. Tokura, and M. Kawasaki. Interface-driven topological Hall effect in SrRuO3-SrIrO3 bilayer. *Science Advances*, 2(7):e1600304–e1600304, July 2016.

[66] Myoung-Woo Yoo, J. Tornos, A. Sander, Ling-Fang Lin, Narayan Mohanta, A. Peralta, D. Sanchez-Manzano, F. Gallego, D. Haskel, J. W. Freeland, D. J. Keavney, Y. Choi, J. Strempfer, X. Wang, M. Cabero, Hari Babu Vasili, Manuel Valvidares, G. Sanchez-Santolino, J. M. Gonzalez-Calbet, A. Rivera, C. Leon, S. Rosenkranz, M. Bibes, A. Barthelemy, A. Anane, Elbio Dagotto, S. Okamoto, S. G. E. te Velthuis, J. Santamaria, and Javier E. Villegas. Large intrinsic anomalous Hall effect in SrIrO3 induced by magnetic proximity effect. *Nature Communications*, 12(1):3283, June 2021. Number: 1 Publisher: Nature Publishing Group.

[67] John Nichols, Xiang Gao, Shinbuhm Lee, Tricia L. Meyer, John W. Freeland, Valeria Lauter, Di Yi, Jian Liu, Daniel Haskel, Jonathan R. Petrie, Er-Jia Guo, Andreas Herklotz, Dongkyu Lee, Thomas Z. Ward, Gyula Eres, Michael R. Fitzsimmons, and Ho Nyung Lee. Emerging magnetism and anomalous Hall effect in iridate–manganite heterostructures. *Nature Communications*, 7:12721, September 2016.

[68] D. J. Groenendijk, N. Manca, G. Mattoni, L. Kootstra, S. Gariglio, Y. Huang, E. van Heumen, and A. D. Caviglia. Epitaxial growth and thermodynamic stability of SrIrO $_3$ /SrTiO $_3$ heterostructures. *Applied Physics Letters*, 109(4):041906, July 2016.

[69] Araceli Gutiérrez-Llorente, Lucía Iglesias, Benito Rodríguez-González, and Francisco Rivadulla. Epitaxial stabilization of pulsed laser deposited Srn+1IrnO3n+1 thin films: Entangled effect of growth dynamics and strain. *APL Materials*, 6(9):091101, September 2018.

[70] Hari P. Nair, Yang Liu, Jacob P. Ruf, Nathaniel J. Schreiber, Shun-Li Shang, David J. Baek, Berit H. Goodge, Lena F. Kourkoutis, Zi-Kui Liu, Kyle M. Shen, and Darrell G. Schlom. Synthesis science of SrRuO3 and CaRuO3 epitaxial films with high residual resistivity ratios. *APL Materials*, 6(4):046101, April 2018.

[71] Nicola Manca, Dirk J. Groenendijk, Ilaria Pallecchi, Carmine Autieri, Lucas M. K. Tang, Francesca Telesio, Giordano Mattoni, Alix McCollam, Silvia Picozzi, and Andrea D. Caviglia. Balanced electron-hole transport in spin-orbit semimetal ${\mathbf{SrIrO}}_{\mathbf{3}}$ heterostructures. *Physical Review B*, 97(8):081105, February 2018.

[72] Lunyong Zhang, Qifeng Liang, Ye Xiong, Binbin Zhang, Lei Gao, Handong Li, Y. B. Chen, Jian Zhou, Shan-Tao Zhang, Zheng-Bin Gu, Shu-hua Yao, Zhiming Wang, Yuan Lin, and Yan-Feng Chen. Tunable semimetallic state in compressive-strained SrIr O 3 films revealed by transport behavior. *Physical Review B*, 91(3), January 2015.

[73] Cai-Zhen Li, Jin-Guang Li, Li-Xian Wang, Liang Zhang, Jing-Min Zhang, Dapeng Yu, and Zhi-Min Liao. Two-Carrier Transport Induced Hall Anomaly and Large Tunable Magnetoresistance in Dirac Semimetal Cd3As2 Nanoplates. *ACS Nano*, 10(6):6020–6028, June 2016. Publisher: American Chemical Society.

[74] B. J. Kim, H. Ohsumi, T. Komesu, S. Sakai, T. Morita, H. Takagi, and T. Arima. Phase-Sensitive Observation of a Spin-Orbital Mott State in Sr2IrO4. *Science*, 323(5919):1329–1332, March 2009.

[75] Q. Cui, J.-G. Cheng, W. Fan, A. E. Taylor, S. Calder, M. A. McGuire, J.-Q. Yan, D. Meyers, X. Li, Y. Q. Cai, Y. Y. Jiao, Y. Choi, D. Haskel, H. Gotou, Y. Uwatoko, J. Chakhalian, A. D. Christianson, S. Yunoki, J. B. Goodenough, and J.-S. Zhou. Slater Insulator in Iridate Perovskites with Strong Spin-Orbit Coupling. *Physical Review Letters*, 117(17), October 2016.

[76] Graham Kimbell, Paul M. Sass, Bart Woltjes, Eun Kyo Ko, Tae Won Noh, Weida Wu, and Jason W. A. Robinson. Two-channel anomalous Hall effect in ${\mathrm{SrRuO}}_{3}$. *Physical Review Materials*, 4(5):054414, May 2020. Publisher: American Physical Society.

[77] T. Nan, C. X. Quintela, J. Irwin, G. Gurung, D. F. Shao, J. Gibbons, N. Campbell, K. Song, S. Y. Choi, L. Guo, R. D. Johnson, P. Manuel, R. V. Chopdekar, I. Hallsteinsen, T. Tybell, P. J. Ryan, J. W. Kim, Y. S. Choi, P. G. Radaelli, D. C. Ralph, E. Y. Tsymba, M. S. Rzchowski, and C. B. Eom. Controlling spin current polarization through non-collinear antiferromagnetism. *arXiv:1912.12586 [cond-mat]*, December 2019. arXiv: 1912.12586.

[78] Karsten Rode, Nadjib Baadji, Davide Betto, Yong-Chang Lau, Hüseyin Kurt, M. Venkatesan, Plamen Stamenov, Stefano Sanvito, J. M. D. Coey, Emiliano Fonda, Edwige Otero, Fadi Choueikani, Philippe Ohresser, Florence Porcher, and Gilles André. Site-specific order and magnetism in tetragonal Mn${}_{3}$Ga thin films. *Physical Review B*, 87(18):184429, May 2013.

[79] C. H. Chen, P. Tseng, Y. Y. Yang, and W. J. Hsueh. Enhancement of thermal spin transfer torque by double-barrier magnetic tunnel junctions with a nonmagnetic metal spacer. *Journal of Physics: Condensed Matter*, 29(2):025806, November 2016. Publisher: IOP Publishing.

[80] Seung-heon C. Baek, Vivek P. Amin, Young-Wan Oh, Gyungchoon Go, Seung-Jae Lee, Geun-Hee Lee, Kab-Jin Kim, M. D. Stiles, Byong-Guk Park, and Kyung-Jin Lee. Spin currents and spin–orbit torques in ferromagnetic trilayers. *Nature Materials*, 17(6):509–513, June 2018. Number: 6 Publisher: Nature Publishing Group.

[81] Huixin Guo, Zexin Feng, Han Yan, Jiuzhao Liu, Jia Zhang, Xiaorong Zhou, Peixin Qin, Jialin Cai, Zhongming Zeng, Xin Zhang, Xiaoning Wang, Hongyu Chen, Haojiang Wu, Chengbao Jiang, and Zhiqi Liu. Giant Piezospintronic Effect in a Noncollinear Antiferromagnetic Metal. *Advanced Materials*, 32(26):2002300, 2020. _eprint: https://onlinelibrary.wiley.com/doi/pdf/10.1002/adma.202002300.

[82] Hyun-Woo Bang, Woosuk Yoo, Chungman Kim, Sunghun Lee, Jiyeong Gu, Yunchang Park, Kyujoon Lee, and Myung-Hwa Jung. Structural, magnetic, and electrical properties of collinear antiferromagnetic heteroepitaxy cubic Mn3Ga thin films. *Applied Physics Letters*, 115(1):012402, July 2019. Publisher: American Institute of Physics.

[83] Jürgen Winterlik, Benjamin Balke, Gerhard H. Fecher, Claudia Felser, Maria C. M. Alves, Fabiano Bernardi, and Jonder Morais. Structural, electronic, and magnetic properties of tetragonal ${\mathrm{Mn}}_{3\ensuremath{-}x}\mathrm{Ga}$: Experiments and first-principles calculations. *Physical Review B*, 77(5):054406, February 2008. Publisher: American Physical Society.

[84] J. C. Slonczewski. Current-driven excitation of magnetic multilayers. *Journal of Magnetism and Magnetic Materials*, 159(1):L1–L7, June 1996.

[85] J. C Slonczewski. Currents and torques in metallic magnetic multilayers. *Journal of Magnetism and Magnetic Materials*, 247(3):324–338, June 2002.

[86] Rocío M. Gutiérrez-Pérez, Ricardo López Antón, Karol Zaleski, José T. Holguín-Momaca, Francisco Espinosa-Magaña, and Sion F. Olive-Méndez. Tailoring magnetization and anisotropy of tetragonal Mn3Ga thin films by strain-induced growth and spin orbit coupling. *Intermetallics*, 92:20–24, January 2018.

[87] R. M. Gutiérrez-Pérez, J. T. Holguín-Momaca, J. T. Elizalde-Galindo, F. Espinosa-Magaña, and S. F. Olive-Méndez. Giant magnetization on Mn3Ga ultra-thin films grown by magnetron sputtering on SiO2/Si(001). *Journal of Applied Physics*, 117(12):123902, March 2015.

[88] Olena Gomonay. Berry-phase effects and electronic dynamics in a noncollinear antiferromagnetic texture. *Physical Review B*, 91(14):144421, April 2015.

[89] D. Fruchart and E. F. Bertaut. Magnetic Studies of the Metallic Perovskite-Type Compounds of Manganese. *Journal of the Physical Society of Japan*, 44(3):781–791, March 1978. Publisher: The Physical Society of Japan.

[90] D. Fruchart, Ph. L'Héritier, and R. Fruchart. Transformations de phases dans les nitrures et carbures du manganese de structure-type perovskite. *Materials Research Bulletin*, 15(4):415–420, April 1980.

[91] H. Tashiro, R. Suzuki, T. Miyawaki, K. Ueda, and H. Asano. Preparation and properties of inverse perovskite Mn3GaN thin films and heterostructures. *Journal of the Korean Physical Society*, 63(3):299–301, August 2013.

[92] Benjamin Balke, Gerhard H. Fecher, Jürgen Winterlik, and Claudia Felser. Mn3Ga, a compensated ferrimagnet with high Curie temperature and low magnetic moment for spin torque transfer applications. *Applied Physics Letters*, 90(15):152504, April 2007.

[93] H. Kurt, K. Rode, M. Venkatesan, P. Stamenov, and J. M. D. Coey. High spin polarization in epitaxial films of ferrimagnetic Mn${}_{3}$Ga. *Physical Review B*, 83(2):020405, January 2011. Publisher: American Physical Society.

[94] J Nogués and Ivan K Schuller. Exchange bias. *Journal of Magnetism and Magnetic Materials*, 192(2):203–232, February 1999.

[95] A. E. Berkowitz and Kentaro Takano. Exchange anisotropy — a review. *Journal of Magnetism and Magnetic Materials*, 200(1):552–570, October 1999.

[96] Florin Radu and Hartmut Zabel. Exchange Bias Effect of Ferro-/Antiferromagnetic Heterostructures. In Hartmut Zabel and Samuel D. Bader, editors, *Magnetic Heterostructures: Advances and Perspectives in Spinstructures and Spintransport*, Springer Tracts in Modern Physics, pages 97–184. Springer, Berlin, Heidelberg, 2008.

[97] Wei Zhang and Kannan M. Krishnan. Epitaxial exchange-bias systems: From fundamentals to future spin-orbitronics. *Materials Science and Engineering: R: Reports*, 105:1–20, July 2016.

[98] A. Kohn, A. Kovács, R. Fan, G. J. McIntyre, R. C. C. Ward, and J. P. Goff. The antiferromagnetic structures of IrMn3 and their influence on exchange-bias. *Scientific Reports*, 3(1):2412, August 2013. Number: 1 Publisher: Nature Publishing Group.

[99] Y. F. Tian, J. F. Ding, W. N. Lin, Z. H. Chen, A. David, M. He, W. J. Hu, L. Chen, and T. Wu. Anomalous exchange bias at collinear/noncollinear spin interface. *Scientific Reports*, 3(1):1094, January 2013. Number: 1 Publisher: Nature Publishing Group.

[100] James M. Taylor, Edouard Lesne, Anastasios Markou, Fasil Kidane Dejene, Benedikt Ernst, Adel Kalache, Kumari Gaurav Rana, Neeraj Kumar, Peter Werner, Claudia Felser, and Stuart S. P. Parkin. Epitaxial growth, structural characterization, and exchange bias of noncollinear antiferromagnetic $\mathrm{M}{\mathrm{n}}_{3}\mathrm{Ir}$ thin films. *Physical Review Materials*, 3(7):074409, July 2019. Publisher: American Physical Society.

[101] C. Mitsumata, A. Sakuma, and K. Fukamichi. Exchange bias model in ferromagnetic/antiferromagnetic bilayer with L1/sub 2/-type ordered antiferromagnet. *IEEE Transactions on Magnetics*, 41(10):2700–2702, October 2005. Conference Name: IEEE Transactions on Magnetics.

[102] Masakiyo Tsunoda, Ken-ichi Imakita, Mamiko Naka, and Migaku Takahashi. L12 phase formation and giant exchange anisotropy in Mn3Ir/Co–Fe bilayers. *Journal of Magnetism and Magnetic Materials*, 304(1):55–59, September 2006.

[103] T. Hajiri, H. Goto, and H. Asano. Scaling the electrical current switching of exchange bias in fully epitaxial antiferromagnet/ferromagnet bilayers. *Physical Review B*, 102(1):014404, July 2020. Publisher: American Physical Society.

[104] Kewen Shi, Ying Sun, Jun Yan, Sihao Deng, Lei Wang, Hui Wu, Pengwei Hu, Huiqing Lu, Muhammad Imran Malik, Qingzhen Huang, and Cong Wang. Baromagnetic Effect in Antiperovskite Mn3Ga0.95N0.94 by Neutron Powder Diffraction Analysis. *Advanced Materials*, 28(19):3761–3767, 2016. _eprint: https://onlinelibrary.wiley.com/doi/pdf/10.1002/adma.201600310.

[105] K. Kamishima, T. Goto, H. Nakagawa, N. Miura, M. Ohashi, N. Mori, T. Sasaki, and T. Kanomata. Giant magnetoresistance in the intermetallic compound $\mathrm{Mn}{}_{3}\mathrm{GaC}$. *Physical Review B*, 63(2):024426, December 2000. Publisher: American Physical Society.

[106] Takejiro Kaneko, Takeshi Kanomata, and Kiwamu Shirakawa. Pressure Effect on the Magnetic Transition Temperatures in the Intermetallic Compounds Mn $_3$ MC (M=Ga, Zn and Sn). *Journal of the Physical Society of Japan*, 56(11):4047–4055, November 1987.

[107] Koshi Takenaka, Masayoshi Ichigo, Taisuke Hamada, Atsushi Ozawa, Takashi Shibayama, Tetsuya Inagaki, and Kazuko Asano. Magnetovolume effects in manganese nitrides with

antiperovskite structure. *Science and Technology of Advanced Materials*, 15(1):015009, February 2014. Publisher: Taylor & Francis _eprint: https://doi.org/10.1088/1468-6996/15/1/015009.

[108] T. Tohei, H. Wada, and T. Kanomata. Negative magnetocaloric effect at the antiferromagnetic to ferromagnetic transition of Mn3GaC. *Journal of Applied Physics*, 94(3):1800–1802, July 2003.

[109] B. S. Wang, P. Tong, Y. P. Sun, X. Luo, X. B. Zhu, G. Li, X. D. Zhu, S. B. Zhang, Z. R. Yang, W. H. Song, and J. M. Dai. Large magnetic entropy change near room temperature in antiperovskite SnCMn3. *Europhysics Letters*, 85(4):47004, March 2009.

[110] Daichi Matsunami, Asaya Fujita, Koshi Takenaka, and Mika Kano. Giant barocaloric effect enhanced by the frustration of the antiferromagnetic phase in Mn3GaN. *Nature Materials*, 14(1):73–78, January 2015. Number: 1 Publisher: Nature Publishing Group.

[111] Ranjana R. Das, Priyadarshini Parida, A. K. Bera, Tapan Chatterji, B. R. K. Nanda, and P. N. Santhosh. Giant exchange bias in the single-layered Ruddlesden-Popper perovskite $\mathrm{SrLaC}{\mathrm{o}}_{0.5}\mathrm{M}{\mathrm{n}}_{0.5}{\mathrm{O}}_{4}$. *Physical Review B*, 98(18):184417, November 2018. Publisher: American Physical Society.

[112] M. Ali, C. H. Marrows, M. Al-Jawad, B. J. Hickey, A. Misra, U. Nowak, and K. D. Usadel. Antiferromagnetic layer thickness dependence of the IrMn/Co exchange-bias system. *Physical Review B*, 68(21):214420, December 2003. Publisher: American Physical Society.

[113] Xiaodong Zhou, Jan-Philipp Hanke, Wanxiang Feng, Fei Li, Guang-Yu Guo, Yugui Yao, Stefan Blügel, and Yuriy Mokrousov. Spin-order dependent anomalous Hall effect and magneto-optical effect in the noncollinear antiferromagnets ${\mathrm{Mn}}_{3}X\mathrm{N}$ with $X=\mathrm{Ga}$, Zn, Ag, or Ni. *Physical Review B*, 99(10):104428, March 2019. Publisher: American Physical Society.